Enhanced Array Design for Tidal Power Generation

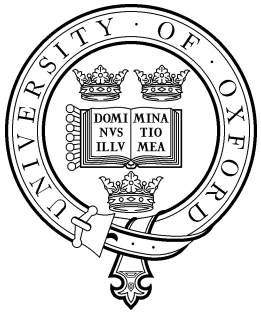

Susannah Cooke
Brasenose College
University of Oxford

A thesis submitted for the degree of
Doctor of Philosophy

Trinity 2016

Acknowledgements

I would like to thank my supervisors for their help and encouragement throughout this DPhil. In particular, I would like to thank Richard Willden for his enthusiasm for the subject, and the many trees' worth of paper we sacrificed to the progress of algebra over the course of our meetings. I would like to thank Byron Byrne for his experimental expertise, his ability to provide an objective viewpoint, and his determination to curtail the length of my sentences when required, except this one. I am grateful to the academics, students and technical staff at the University of Manchester, who provided local support and friendship while I was carrying out experimental work there. I must also thank my fellow students in Jenkin room 11 for a combination of entertaining lunchtime conversations and actual useful discussions of fluid dynamics. Particular thanks are owed to Chris Vogel and Aidan Wimshurst for their unceasing willingness to listen to me talking about my problems.

I would like to acknowledge the support of the EPSRC SuperGen UK Centre for Marine Energy Research, who provided funding for the first three years of my research. I would also like to thank Harris Manchester College for the opportunity to work as a Junior Dean in my final year and widen my experience of university life.

My friends, both in Oxford and elsewhere, have been crucial to my enjoyment of this degree and my time in Oxford. I would like to thank the members of OURPGSoc for hugely enriching my life outside of work, and for just generally being a lot of fun to spend time with. I am grateful to my mother, Frances, who accepted that I wished to become a poverty stricken student for a second time, and tried to forgive me for involving mathematics again. Special thanks go to chromatic chris, for distant encouragement and sympathy emanating from California, as well as for having made it through a DPhil before me and proved it to be possible. Finally, my thanks to James, whose love, and reciprocal support of academic meltdowns for the last two years, have been invaluable.

Abstract

Enhanced Array Design for Tidal Power Generation

A thesis submitted for the degree of Doctor of Philosophy

Susannah Cooke

Brasenose College, Oxford

Trinity Term 2016

Tidal stream energy is a predictable source of renewable energy. Tidal stream turbines have been proposed as a way to extract useful energy from the tide. Many arrays of such devices will need to be installed to extract significant amounts of energy. The presence of an array of turbines within a tidal flow will impact the flowfield, as complex fluid interactions occur across multiple scales. This thesis is concerned with the behaviour of tidal turbines arrayed across channels. Experimental and analytical work is carried out to investigate array behaviour and to create new modelling tools to replicate this behaviour.

Linear Momentum Actuator Disc Theory (LMADT) is employed to develop a new analytical model for a long row array of tidal turbines split into multiple smaller, co-linear row arrays. An argument of separation of scales is used to facilitate this model. It is found that increases in power extraction beyond that of a single continuous row array are possible.

Experimental work is carried out on a row array of eight porous discs, simulating a short row array of tidal turbines. Disc porosity and spacing are varied to investigate thrust on the array, flow behaviour behind the array and an 'inferred' power removed from the flow. The results are compared to previously developed theoretical models. Good agreement is found with the trends of the analytical model, for example that there is a peak power coefficient which can be reached through appropriate selection of spacing and disc resistance. Differences from theory are found in the total thrust and power measurements, as well as in some aspects of the flow behaviour in the array wake. Reductions in thrust and power towards the ends of the array are also identified as 'end effects' which are not included in the analytical model.

Based on these results a new semi-empirical model is proposed, using LMADT with experimental data closure. This model allows variation of the disc resistance across a row array. Values from the experimental work are used as inputs to the model, and the results compared to experimental measurements of flowspeed, thrust and power. Although agreement with experimental results is found in some areas, there are still some discrepancies between the analytical model and the experimental results. This indicates that there are additional factors that contribute to end effects on a short row array.

Nomenclature

Variables

α	Device induction factor
β	Bypass induction factor
γ	Wake induction factor
η	Basin efficiency
Θ	Open area ratio
κ	Pressure coefficient of device resistance
ν	Kinematic viscosity
ρ	Fluid density
τ	Reynolds stress
A	Cross-sectional area
a	Alternate device induction factor, $a = (1 - \alpha)$
B	Blockage ratio
C_P	Power coefficient
C_T	Thrust coefficient
d	Device diameter
f	Frequency
Fr	Froude number
g	Gravitational acceleration
h	Channel height
L	Characteristic length
m	Number of sub-arrays in array
n	Number of devices in sub-array or array
p	Static pressure
P	Power
Q	Volumetric flow
q	Dynamic pressure
Re	Reynolds number

s	Edge to edge spacing
St	Strouhal number
T	Thrust
t	Time
U	Steady-state flow speed in the x direction.
u	Instantaneous flow speed in the x direction.
$\mathbf{u}$	Velocity vector
w	Channel width

Subscripts

$_{0.3d}$	Value at 0.3 disc diameters downstream of array
$_1$	LMADT channel position: at upstream device streamline boundary
$_2$	LMADT channel position: immediately upstream of device
$_3$	LMADT channel position: immediately downstream of device
$_4$	LMADT channel position: at downstream static pressure equalisation
$_5$	LMADT channel position: immediately downstream of core/bypass mixing
$_\infty$	Freestream flow
$_A$	Array scale
$_B$	Bypass flow
$_C$	Channel flow
$_D$	Device flow
$_{\text{disc}}$	Disc plane
$_F$	Farm scale
$_G$	Global scale
$_i$	Pertaining to the ith streamtube
$_L$	Local scale
$_S$	Single streamtube (Chapter 7 only)
$_W$	Wake

Superscripts

$^+$	Immediately upstream of an LMADT station
$^-$	Immediately downstream of an LMADT station

Abbreviations

ADV	Acoustic Doppler Velocimetry
BEM(T)	Blade Element Momentum (Theory)
CFD	Computational Fluid Dynamics
DAQ	Data Acquisition
LES	Large Eddy Simulation
LMADT	Linear Momentum Actuator Disc Theory
PTO	Power Take Off
RANS	Reynolds-Averaged Navier-Stokes
SWE	Shallow Water Equations
TKE	Turbulence Kinetic Energy

Contents

Chapter 1

Introduction

The power present within tidal currents around the world represents a source of predictable renewable energy. Given that tidal currents can be easily forecast, they offer the opportunity to provide a much more predictable supply of energy than other renewable sources such as wind or solar power. Over the last two decades, interest in exploiting this potential has grown, resource assessments have been undertaken in countries where the tidal currents are strongest, and developers have designed devices capable of extracting this energy. The UK has significant potential for tidal energy generation due to the high tidal currents or tidal range present at multiple locations around its coastline [14]. As such, there is considerable public and private interest in developing such capacity. This chapter will give a short review of the current state of commercial development, resource estimation and national targets. A more detailed review of the current state of tidal turbine modelling is undertaken in Chapter 2 to place the work undertaken in this thesis into context.

Two types of technology currently exist at viable commercial scale to exploit tidal power; tidal barrages and tidal stream turbines. Tidal barrages are an established technology, whereby the potential head of water at sites with high tidal range is held behind a dam and expelled through turbines within the dam which generate

(a) Axial-flow

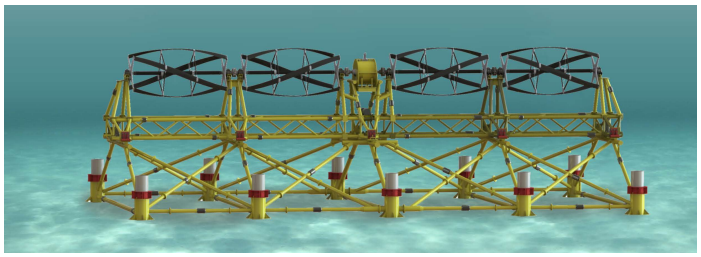

(b) Cross-flow

Figure 1.1: Artists' impressions of a) an array of axial-flow tidal turbines and b) an array of cross-flow tidal turbines. (Images reproduced with permission of a) Scottish-Power Renewables and b) Ocean Renewable Power Company.)

electricity. There are currently a small number of tidal barrage sites in operation around the world, of which the largest is the La Rance power plant in France, with a generating capacity of 240 MW [94]. The requirement to dam an estuary or bay to create such capacity, however, is not always popular or justifiable, as it will not only affect tidal range but may also have significant ecological impacts. In the UK, multiple barrage schemes have been considered, particularly in the Severn Estuary, but the challenges to mitigate environmental impacts are significant [53]. As such, the tidal lagoon project in Swansea Bay is the only tidal range project in development in the UK at present [133].

Tidal stream turbines, by comparison, do not entirely block tidal flows with a dam. Instead, they rely on individual turbines, sometimes grouped in arrays, which only block the flow insofar as the tidal current is slowed down by their presence. They therefore operate in much the same way as wind turbines, capturing available power from the ambient freestream flow. As a result, they must be placed in locations with

Figure 1.2: SeaGen turbines (Image reproduced with permission of Atlantis Resources.)

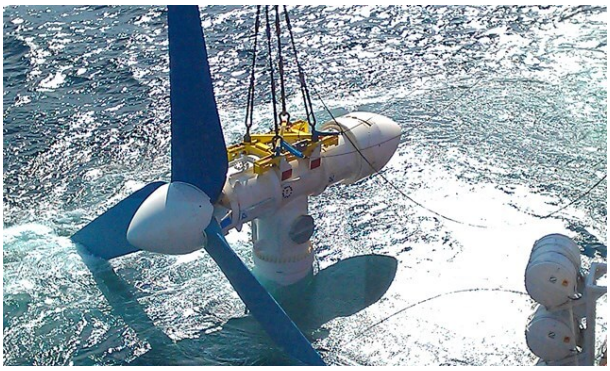

Figure 1.3: AR1000 prototype turbine (Image reproduced with permission of Atlantis Resources.)

relatively high speed tidal flows. There are two main types of tidal stream turbine design under development: axial-flow turbines, sometimes referred to as horizontal axis turbines, which extract energy from flow parallel to their rotational axis; and cross-flow turbines, which do so with flow transverse to the rotational axis. Cross-flow turbines can be either vertical or horizontal, and so the term 'horizontal axis turbine', which is sometimes used for axial-flow turbines, will not be used in this thesis to avoid confusion. The two types of technology are shown in Figure 1.1. Given that the majority of recent deployments of prototype turbines have been axial-flow turbines [94], this thesis will assume that deployed turbines are likely to be of the axial-flow variety. It should be noted, however, that this is only relevant to the work described herein insofar as the turbine cross-section perpendicular to the flow is generally assumed to be circular.

It is worth noting that other tidal stream energy devices are also under development, such as oscillating devices or tidal 'kites' [100], however these are currently at early stages of design and prototyping, and are not considered within this thesis.

1.1 Current State of Industry

Tidal stream turbines are approaching the stage of industry maturity where multiple large-scale prototypes are undergoing testing, with the first full-scale installations now underway. The UK in particular has several commercial-scale prototypes in testing or development, as well as imminent commercial deployment of a small number of turbines. Examples of large-scale axial-flow prototype turbines include the dual-turbine SeaGen installation in Strangford Narrows, as shown in Figure 1.2, which has 1.2 MW capacity and has been exporting power to the grid since 2009 [94]. This two-turbine structure is now in the process of being decommissioned after exporting a total of 10 GWh to the grid. ScotRenewables have recently deployed a 2 MW dual-turbine floating generator as shown in Figure 1.4 which will operate at the European Marine Energy Centre (EMEC) test site in Orkney, UK [99]. A number of other device prototypes have also been or are currently being tested at EMEC, whose facilities include grid connection and performance monitoring. Examples include the single turbine models of Atlantis Resources' AR1000 as shown in Figure 1.3 and Andritz Hydro Hammerfest's HS1000 [48] as shown in Figure 1.6. Full-scale commercial installations of tidal turbines are due to be constructed within the near future, with MeyGen's initial 4-turbine array in the Pentland Firth to be installed by the end of 2016. Cable installation on this project is now complete, subsea turbine structures have been installed and the first of four 1.5 MW turbines manufactured by Andritz Hydro Hammerfest and Atlantis has now been installed and is producing power [98]. Similarly in France, OpenHydro have deployed a ducted, open-centre turbine as shown in Figure 1.7, recently completing installation of the second turbine in a two-turbine array at Paimpol-Bréhat which will export 1 MW to the grid [93]. EDF and OpenHydro are working towards the 'Normandie Hydro' installation of a full commerical array of seven 2 MW turbines in 2018 [93]. These projects will yield the first large-scale data regarding tidal stream turbines deployed in arrays, although

Figure 1.4: Deployment of ScotRenewables' SR2000 dual-turbine floating generator (Image reproduced with permission of Scotrenewables Tidal Power Ltd.)

the widespread successful deployment of tidal arrays which could lead to continued, long-term industrial investment is still some way off [12].

1.2 Tidal Resource Assessment

Tidal resources are geographically diverse around the globe, with most locations suitable for tidal stream turbine deployment restricted to a relatively small number of countries with sites of high tidal stream velocity. As a result, only countries with these resources are prioritising investment in tidal stream technology; examples of such countries are the UK, Ireland, Canada and New Zealand, where sites with high tidal flows are found. A map of the peak spring tidal flow speeds in UK waters is shown in Figure 1.5.

Resource assessments are crucial to understanding the potential for tidal energy extraction. Uihlein & Magagna [124] summarised the various resource assessments that have been undertaken in multiple countries around the world; in the UK, several studies have been undertaken to attempt to quantify the total tidal resource available. Given the complexity of the problem, and the difficulty in obtaining the required wealth of data, estimates of available resource can vary widely. When interest in tidal stream turbines began increasing in the late 20th century, estimates of available

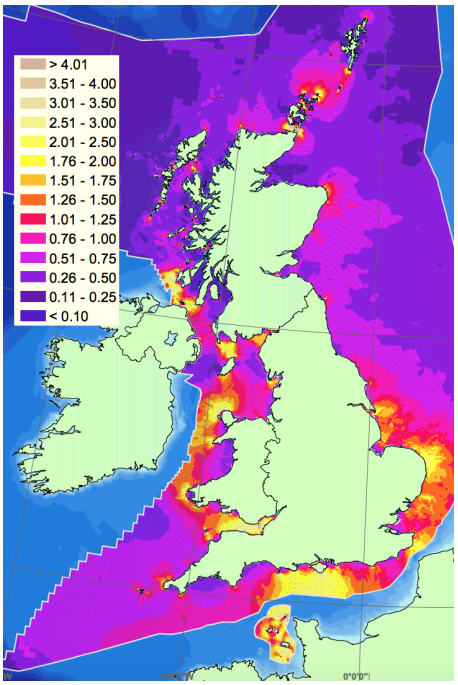

Figure 1.5: Peak flow speed in m/s for mean spring tide around the UK. (Image reproduced from Atlas of UK Marine Renewable Energy Resources, DTI, 2004 [69] with permission of ABPmer. Data sourced from http://www.renewables-atlas.info/. ©Crown Copyright.)

power were usually based on kinetic energy flux, similar to the wind industry [39]. This assumption continued to be used in detailed assessments of the tidal resource as the first industrial-scale turbine installations in the UK were under discussion and development [42]. However, subsequent tidal energy studies have highlighted that this approach is not always correct for tidal power, particularly since tidal flows are not unbounded, whilst wind is usually assumed to be. Exemplifying the variability, the Carbon Trust published two reports, in 2005 and 2011, which respectively estimated the UK's available resource at 18 TWh/yr and 29 TWh/yr [9] [15]. This can be compared to the total UK energy supply of 360 TWh in 2015 [31]. The earlier Carbon Trust report used a simple kinetic energy method, as used in the wind industry, while the latter amended this in line with more recent tidal research to model tidal turbine farms as frictional drag terms within a coastal-scale model. Subsequently, the Crown Estate published a revised figure of 95 TWh/yr [37], using the same hydrodynamic

Figure 1.6: HS1000 prototype turbine
(Image reproduced with permission of Andritz Hydro Hammerfest.)

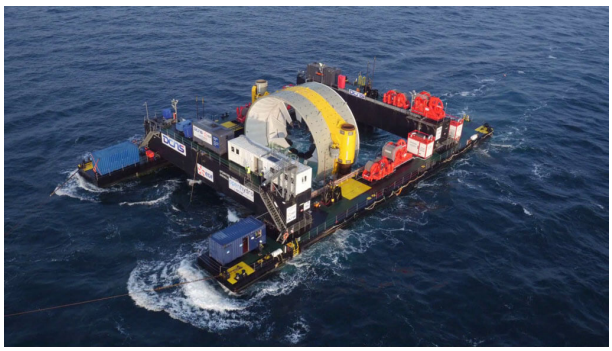

Figure 1.7: OpenHydro deployment at Paimpol-Bréhat
(Image reproduced with permission of DCNS/OpenHydro.)

methodology as the Carbon Trust 2011 report but relaxing several of its constraints to allow more shallow-water and low-energy sites to be included [38]. While these energy estimates for all UK coastal waters are very variable, the local estimates of the tidal resource within specific tidal basins are more immediately relevant to developers. Therefore, the British Standards have recently been updated to include guidance on standardised methodology to assess the available tidal energy [57] at sites identified for potential development. Specific computational studies of individual areas for potential development will be discussed further in Section 2.3.3. As resource assessments become more accurate, developers' certainty in power predictions will increase and aid general confidence in the industry.

1.3 National and International Policies

Renewable energy as a whole has been undergoing growth around the world, and is the second largest contributor to global electricity generation [56]. The majority of renewable generation at present comes from hydropower, as shown in Figure 1.8a. However, there has been recent significant growth in wind and solar generation, particularly in the more wealthy countries of the Organisation for Economic Co-operation

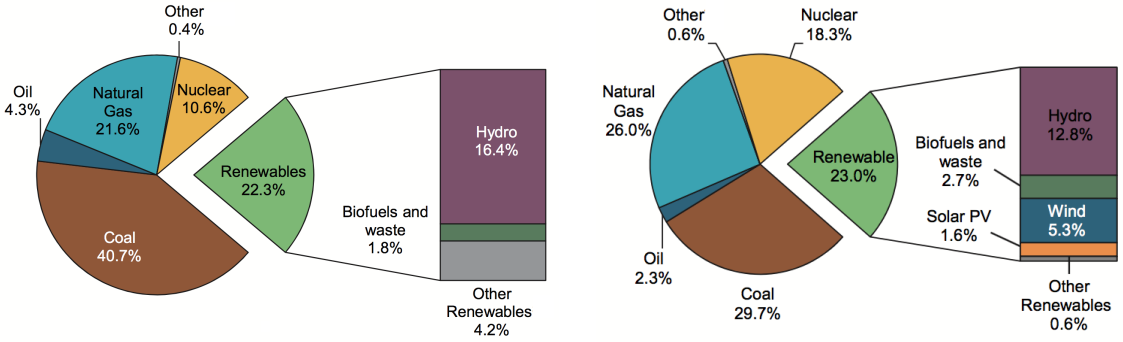

(a) World (b) OECD

Figure 1.8: Energy source shares in a) world and b) OECD members' electricity generation, 2015. (Image ©OECD/IEA 2016, Key Renewable Trends, IEA Publishing [56]. Licence: www.iea.org/t&c.)

and Development (OECD), as shown in Figure 1.8b. Many countries have set targets for renewable energy generation in the future, including the European Union's target for 20% of energy generation from renewables by 2020, as set in 2009 [95]. This target of 20% varies by country according to their previous energy mix and potential; the UK's 2020 target, legally binding within EU law, is 15% [28]. This target includes all forms of energy generation and consumption, i.e. not only electricity but also heat, transport etc. Although progress towards this target continues to be made [30], it has recently been identified by the UK's National Grid, studying multiple scenarios for future energy usage, that the target will be missed [50]. This is not due to the generation mix for electricity, however, which remains on target, but due to the likely failure to meet heat and transport targets.

The European Commission has a target to reduce greenhouse gas emissions to 80-95% below 1990 levels by 2050 [21]. Having considered various scenarios for achieving this target, it is noted that all rely on increased electricity generation to replace transport and heating reliance on carbon-intensive fuels. Renewable electricity generation will have an important part to play in this process.

Within electricity generation in the UK, technologies such as onshore wind energy

and hydropower are now solidly established, coupled with rapid growth in solar energy and offshore wind energy. Tidal energy is not as advanced as these technologies, but has high predictability and potential for high density energy generation. It is therefore identified as an important area for incentivisation and growth. It is a key element of the UK's Renewable Energy Roadmap (published in 2011 [28]), and is supported through ongoing policies thereafter [29]. There continues to be support for research and development, including support for pre-commercial array demonstrations such as the initial MeyGen deployment, partially funded by the the Marine Energy Array Demonstrator grant scheme [30]. Support such as funding and provision of testing sites such as EMEC are allowing the UK tidal energy sector to lead the world in deployment of early commercial turbine models. Government policies such as this are crucial to the development of tidal stream energy in the UK and around the world, together with co-operation between developers. This will be particularly important in the next decade as the industry strives to reach technological maturity and bring costs of energy down in line with market values [12].

1.4 Future Development

Although individual or dual turbines have been deployed, as described above, significant commercial success at array scale must be achieved before the tidal stream industry can be considered to have reached maturity [12]. Successful deployment will be reliant on better understanding of the resource, fluid dynamics, turbine build costs, offshore maintenance, electrical transmission costs etc. In particular, understanding the behaviour of turbines within arrays is essential, as no single turbine can extract all the available power in the most promising tidal sites. Array behaviour is known to be complex, and can increase or decrease extractable power based on non-intuitive relationships. As such, much work is being undertaken to investigate the behaviour

of tidal turbines in arrays, as discussed by Vennell *et al.* [129]. Enhancing the understanding of this behaviour will be critical to ensuring commercial success at array scale, and is the focus of this thesis.

1.5 Aims and Outline of this Thesis

A large body of work has been carried out to investigate the behaviour of tidal turbines, but there are still gaps in understanding which prevent knowledge being easily applied to future design and installation of such devices. In particular, array behaviour is the subject of much recent study and has complexities beyond those previously considered for wind turbines. This thesis focuses on analytical models as a simple, computationally light tool to allow fundamental behaviours of tidal turbine arrays in constrained flows to be studied. Recognising, however, that analytical models are often seen as being too far removed from real fluid flow to allow for their use in the commercial design process, experimental work is also included to validate these models and develop corrections for them. The thesis focuses on array-scale modelling as being the most relevant to the current state of technological development, as arrays are now being designed and built for commercial operation. Given the large body of work indicating that single row arrays perform optimally for power extraction (as will be further discussed in Chapter 2), the thesis will focus on this type of array layout.

- Chapter 2 undertakes a literature review of modelling methods used for tidal turbines: analytical, computational and experimental. Modelling of arrays in particular is highlighted, and conclusions drawn regarding the general trends seen.

- Chapter 3 explores a new analytical model which has been developed to investigate the potential for splitting a single row array into multiple shorter row arrays across a wide tidal channel. The formulation of this model is described, and results are presented which show that there is potential to further improve energy extraction beyond that of a single unbroken row array in such a channel.

- Chapter 4 discusses the set-up and results of a short scoping experiment carried out using existing equipment to investigate the single row array model of

Nishino & Willden [87]. This scoping exercise was designed to confirm the viability of further experiments and to focus the planned parameter space and measurements to be taken. Results from these experiments are compared to predictions from analytical theory.

- Chapter 5 describes the implementation of experimental testing designed to fully investigate and validate the single row array model of Nishino & Willden. The design of experimental equipment to facilitate these tests is discussed, and data quality methodology observed during testing is described.

- Chapter 6 presents the results of the main experimental testing of a single row array of eight porous discs, varying spacing and disc porosity to investigate changes in behaviour. Results for both thrust and extractable power are discussed and compared to the predictions of analytical theory. Wake measurements of flow behaviour are studied to investigate the validity of assumptions made within the analytical theory. Differences between a short row array and the quasi-infinite array assumed in analytical theory are discussed.

- Chapter 7 looks at ways to implement the impact of end effects on a short row array as seen in the experimental results. A revised analytical model with capacity to vary resistance across an array is presented, and its results are compared to experimental results. Recommendations are made regarding further work required to fully model end effects.

- Chapter 8 presents conclusions to the work of this thesis, and gives recommendations for further work which could be carried out in this area to extend the current understanding of row array behaviour of tidal stream turbines.

Chapter 2

Review of Modelling of Tidal Turbines and Arrays

Given high potential energy yields, and government policies encouraging tidal energy development, much work is presently being undertaken to further develop the technology. Tidal turbines are large, expensive devices to commission, install and maintain. Understanding their potential energy yield, build requirements and lifetime maintenance cost are crucial to ensuring that installations are profitable and deliver the performance expected. The design decisions in each of these areas are driven by the fluid mechanics of the environment in which the turbine will be located, in terms of the forces on the turbine and the energy resource available. Installing more than one turbine in the same area (i.e. building a tidal array) will incur additional inter-turbine effects through interactions with fluid flow. It is therefore critical to understand the fluid flow through and around turbines and arrays prior to design and installation of production-scale devices. Modelling of fluid dynamics is complex, whether done analytically, computationally or experimentally, and will inevitably require some compromises and assumptions to achieve results over a reasonable timescale. A large amount of research has already been undertaken in this area, some of which is now

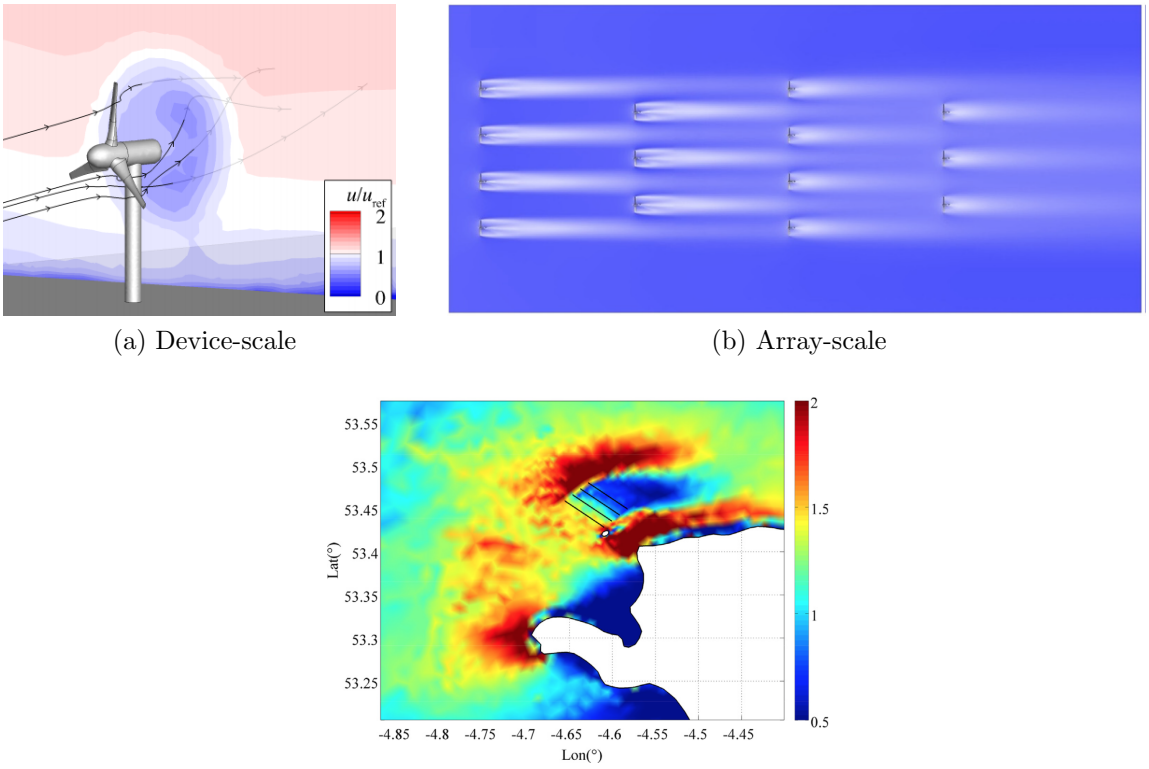

(a) Device-scale

(b) Array-scale

(c) Basin-scale

Figure 2.1: Examples of different scales of computational modelling: a) the velocity field around a single rotor (from Fleming, 2014 [40]); b) the velocity field around a staggered array of turbines (from Malki *et al.*, 2014 [73]); c) the velocity field around row arrays in the Anglesey Skerries basin area (from Serhadlıoğlu *et al.*, 2013 [107]). (Images reproduced with permission of a) C. Fleming and b, c) Elsevier.)

being used to guide the design of the first generation installations of tidal turbine arrays.

The flow around a turbine, or an array of turbines, is governed by fluid interactions at multiple scales. As such, modelling has focused on understanding the fluid behaviour at each different scale, often attempting to decouple interactions where possible to simplify the problem. Device and array scale modelling are usually carried out using channels of rectangular cross-section with prescribed flow speeds, while basin scale modelling includes accurate bathymetry and tidal forcing but simplifies power extraction to avoid the need to fully model a tidal turbine interacting with the flow. The different scales are exemplified in Figure 2.1, which shows computational

results from work at each of these scales. This chapter reviews the available literature, considering modelling work performed in terms of scale of model and types of model (experimental, analytical (theoretical) and computational). This thesis focuses on understanding the behaviour of tidal turbine arrays through analytical and experimental modelling, and as such these areas are discussed in more depth.

2.1 Device Scale Modelling

Device scale modelling is taken to be any modelling which focuses only on a single device. Such modelling typically analyses either the performance of a specific rotor design, or a specific aspect of tidal turbine behaviour which can be analysed using only one device. These models can also form the basis of expanded models for array or basin modelling if they are simple enough to be replicated.

2.1.1 Experimental Modelling

Experimental modelling of single devices ranges from the large-scale testing of prototype production turbines in offshore conditions down to small-scale models of device behaviour using either rotor scale models or porous emulators in recirculating flumes or towing tanks. In all cases, these tests are undertaken to establish loads on the device, potential power output and consequences to the surrounding fluid flow and local environment.

2.1.1.1 Porous Discs

A porous disc, which can emulate the flow resistance of a tidal turbine, can be used to investigate flow patterns around a device and the thrust loading on it. They are restricted by their inability to simulate swirl or other rotational properties of a turbine, and the fact that they have no power take-off mechanism. However, if these

restrictions are considered of low importance to the area of study then porous discs afford a simple, cheap and reliable way to investigate device-fluid interaction without complicated scaling or power take-off (PTO) requirements. The porosity of the disc determines its resistance to the flow, and as such a variety of different resistances can be easily investigated using multiple discs.

Porous discs were previously used in experimental investigation of wind turbine wakes for this reason, as described in Sforza *et al.* [108] in the early 1980s, where a series of experiments were carried out using multiple porosities of a single porous disc to investigate the relationship between wake development and turbine thrust.

Similar studies have been carried out more recently for tidal turbine research. Porous discs have been used in small-scale experiments where dimensions are restricted by available testing facilities. In such situations, attempts to use scale rotors result in extremely high tip speed ratios if scale similarity is achieved (which then induce unrealistic swirl and pressure gradients into the flow field). Porous disc studies of this kind typically focus on the relationship between device thrust, which can be replicated through varying disc porosities, and downstream wake development.

Bahaj *et al.* [5] carried out one of the earliest evaluations of the feasibility of experimental testing of marine tidal turbines in 2007, identifying and investigating the parameters which govern wake development and recovery. Having identified thrust coefficient as one of the most important characteristics to correctly simulate, they drew on the earlier use of porous discs as wind turbine simulators and carried out a series of experiments using porous discs in a water flume. They successfully demonstrated that porous discs could adequately simulate the far wake region of a tidal turbine, allowing them to be used for simple experimental simulation where wake interactions were of foremost importance.

Whelan (2010) [135] used both a porous disc and a rectangular porous strip, as shown in Figure 2.2, to investigate the effects of free-surface proximity on the thrust

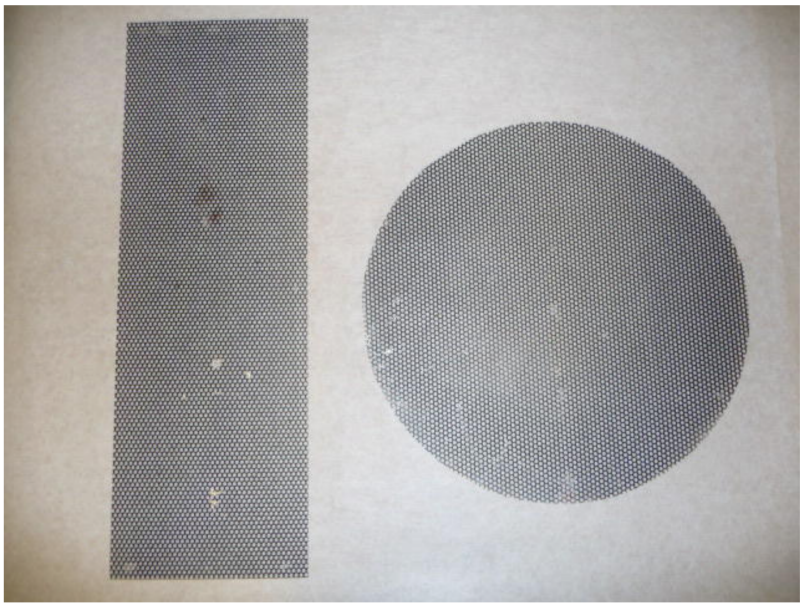

Figure 2.2: An example of an experimental porous strip on the left, and porous disc on the right. (Image reproduced from Whelan, 2010 [135] with permission.)

performance of tidal devices. The output of this work was used to inform a revised analytical model for free-surface effects.

Sun (2008) [117] used discs with two different porosities to investigate the differences between an experiment in a towing tank and an experiment in the more natural channel of a dam overflow, as well as comparing these results to predictions from a computational actuator model. The results showed higher force on the less porous disc, as would be expected, but also found variations in thrust loading between the channel experiment and the towing tank. These were judged to be due to both a sheared profile in the channel and the influence of ambient turbulence. It was also found that increased flow speed resulted in increased energy extraction but also increased wake recovery length.

Multiple experimental studies with single porous discs have been carried out at the University of Southampton. Harrison *et al.* 2010 [52] compared wake measurements downstream of porous discs to wake predictions from a three-dimensional computational method using actuator discs, and found good agreement. Myers & Bahaj 2010

[84] and Bahaj *et al.* 2012 [4] investigated the streamwise wake velocities downstream of a single porous disc, using discs of varying porosity at varying depths within the water column. They concluded that higher resistance discs had a greater wake velocity deficit immediately downstream but that this difference disappeared by approximately six disc diameters downstream. This result agrees with other work carried out using scale rotors [81] [82] and shows that far wake mixing is governed primarily by ambient turbulence. Immersion depth of the rotor was also studied, together with a variation in bed roughness. It was discovered that turbines low in the water column have a wake that persists further downstream, and that increasing bed roughness can exacerbate this problem. The potential requirement for a non-axisymmetric model to incorporate these factors was identified.

There is also an area of research that focuses on understanding the behaviour of porous discs themselves, and their potential weaknesses for simulating rotating devices, despite their ease of deployment. Taylor [119] is widely recognised as having developed reasonable theoretical relationships in the 1940s governing the behaviour of porous discs' drag coefficients as related to their open area ratio, but further work has improved upon this understanding. Graham [49] compared Taylor's theory to experimental measurements in the 1970s and found that the prediction of drag coefficient was only reasonable for relatively low disc resistance. Castro [17] found a distinct change in disc behaviour once disc open area ratio dropped below approximately 20%. This work was largely focused on wind turbine applications, but more recently the behaviour of porous discs has been revisited by Blackmore *et al.* [10], with a focus on tidal channels and experimental simulations. This new study found a dependence of porous disc drag coefficients on both the turbulence intensity and turbulence length scales of the oncoming flow. This result has implications for relating experimental results from porous discs directly to real-world behaviour of turbines in tidal flows.

2.1.1.2 Scale Rotors

Unlike porous discs, which are usually adopted for small experimental work where facility constraints mean that rotors would be difficult to accurately construct or run, scale rotors can be deployed in larger tests, up to and including prototype testing of commercial tidal turbine rotors. An example of the latter would be the testing undertaken by Andritz Hydro at the offshore EMEC test facility [48], where the rotor diameter of 21 m gave a rated output of 1 MW. Similar large-scale testing is also being undertaken by other major developers such as Alstom [78].

The majority of research, however, is still being done using smaller-scale rotors in well-instrumented test facilities. This leads to lower Reynolds numbers, due to the reduced diameter of the rotors (and often reduced flow speed of the facilities versus real tidal sites). As a result, differences in tip speed ratio, thrust coefficient and power coefficient are experienced in such experimental testing. The Froude number of an experimental facility may also vary significantly from that of a real tidal channel. It is possible, however, to match some of these non-dimensional parameters where required for the study of specific aspects of rotor behaviour.

An early set of experiments carried out by Myers & Bahaj [83] on a 1:30th scale rotor of 0.4 m diameter in a recirculating flume with 0.84 m water depth experienced significant variation in free surface height before and after the rotor, including a hydraulic jump downstream due to some flow becoming supercritical. This was judged to be due to the effects of a much higher Froude number in the experimental channel than would be found in real tidal channels, combined with a high blockage ratio (determined as being the ratio of device frontal area to channel cross-sectional area). A further set of experiments by Bahaj *et al.* [3] explored a scale rotor of 0.8 m diameter in both a cavitation tunnel and a towing tank of 1.8 m depth, but with a focus on the thrust and power characteristics of the rotor, rather than its wake. Tests were carried out at different rotational speeds and blade pitch angles to establish representative

thrust and power curves, and to establish whether cavitation was probable. Cavitation was not recorded for tip speed ratios lower than 7, and further work carried out by Batten *et al.* identified appropriate tip speed ranges below this to avoid cavitation.

Whelan [135] undertook scale rotor experiments as well as porous disc experiments, investigating the phenomenon of free-surface influence and the characteristics of unsteady flow, including inertial terms. The scale rotor was deployed in both a small flume channel and a wind tunnel of much larger cross-section. This work validated an analytical model for free-surface effects [134] and provided insight into the inertial effects of unsteady flow around the rotor. Possible corrections to numerical models which could be made accordingly were identified. Further investigation into the effects of unsteady flow on the thrust performance of a scale rotor was carried out by Milne *et al.* [80]. Unsteady loads associated with stall were found to be far greater than those in unstalled conditions, meaning that turbines operating near the blade stall point risk large increases in thrust and hence fatigue.

Whelan & Stallard [136] proposed the use of a scale rotor that was not geometrically scaled to match a proposed full-scale design, but instead designed to perform better at low experimental Reynolds numbers whilst maintaining similar rotational speeds to full-scale turbines. This enabled performance parameters such as the relationship between thrust coefficient and tip speed ratio to be matched to the full scale. This was prioritised because wake development and wake interaction are governed by momentum extraction and by swirl (both directly influenced by thrust coefficient and tip speed ratio). Data collected from such representative rotors may well be more applicable to field behaviour of full-scale rotors than the behaviour of exactly geometrically scaled copies of those rotors would be. This is particularly relevant for scale modelling of arrays, where wake interactions are particularly important.

The alternatively scaled rotor design has been used in subsequent experimental work undertaken at the University of Manchester. Several studies of small arrays

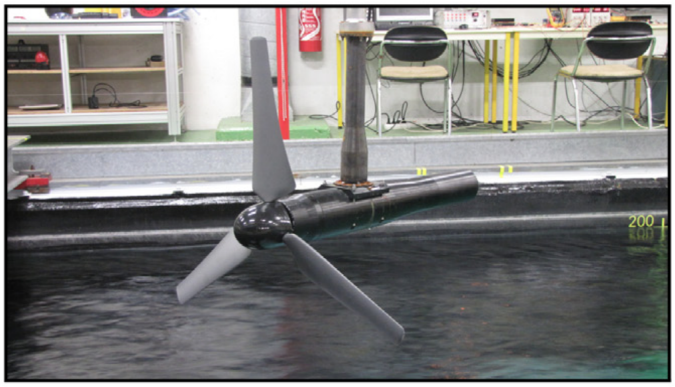

Figure 2.3: An example of an experimental scale rotor. (Image reproduced from Mycek *et al.* 2014 [81] with permission of Elsevier.)

and wake interactions using this rotor are discussed in Section 2.2.1.2. The rotor's individual performance and wake generation were fully investigated and discussed by Stallard *et al.* 2015 [114]. It has also been used as a single rotor to study the influence of waves by Olczak *et al.* [92], being placed in a recirculating flume with waves generated opposing the current. The variation in wake deficit downstream of the rotor for different wave climates was explored. For all wave heights considered, a reduction in wake deficit was measured downstream of the turbine, showing increased mixing due to waves. The depth to which the wake was affected by this was determined by the significant wave height, with more energetic waves found to cause more rapid wake recovery. Similar results have been found by de Jesus Henriques *et al.* [26], who extended their study [27] to the reduction of wave-induced thrust loads through appropriate blade pitching.

The rotor used in the de Jesus Henriques studies was originally designed and deployed by Tedds [120] [121], and includes a variable number of blades and with variable blade pitch angle. This rotor was deployed in a flume where inlet turbulence and inlet velocity profile could be varied, so that the effects of these parameters on the turbine wake could be studied. Comparisons were also drawn to the porous disc studies of Harrison *et al.* [52] and Myers & Bahaj [84], and it was found that turbulent

kinetic energy decayed significantly faster behind the turbine than behind the disc. This was expected, due to additional turbulent mixing caused by rotor swirl and tip vortices, and was confirmed by this testing. Additionally, significant turbulence anisotropy was discovered in the wake regions for all testing configurations, casting doubt on assumptions of turbulence isotropy which are often made in computational work. However, little variation in wake behaviour was found by varying the inlet turbulence intensity from 2% to 5%, or in introducing a sheared profile. It was concluded that perhaps these changes had not been significant enough to witness wake variation as reported by others such as Chamorro *et al.* [18]. Chamorro's study showed significant coupling of turbine response with onset flow turbulence below a critical frequency, which could impact the behaviour of deployed devices in real tidal flows near to sources of large energetic vortex structures, such as submerged rock pinnacles or human-built structures. However, Mycek *et al.* [81] also performed single rotor experiments with varying turbulence, and found that even though wake behaviour was strongly impacted by freestream turbulence, mean rotor performance was less affected. The rotor used in this experiment is shown in Figure 2.3.

Experimental deployment of scale rotors continues to be one of the most well-regarded ways to investigate the behaviour of single turbines, and recent work continues to cover a wide scope of areas of investigation. This ranges from Jordan *et al.*'s [63] confirmation of lack of wake recovery for rotors near to the bed as highlighted in Bahaj *et al.*'s 2012 porous disc work [4], through Jeffcoate *et al.*'s [59] investigation of rotor submergence which found power losses when a rotor is too close to the free surface, all the way up to ocean deployment of full-scale commercial devices such as SCHOTTEL's relatively small rotor [60] or Alstom's much larger one [78].

2.1.2 Analytical Modelling

Analytical modelling of tidal turbines involves reducing the governing fluid equations to a point where they can be fully closed and solved without the need for a discretised computational solver. This is done by making assumptions about the flow, and the turbine, which are appropriate to the conditions of turbine operation. While it is not possible to extract full operating parameters and flow regime information from such models, they can provide a generalised and simple method to investigate trends of turbine/flow interaction. They are of particular interest for studying interactions at array scale, where the 'ideal' array layout is often unclear or non-intuitive. They can be used to establish trends of behaviour or facets of generalised flow behaviour in tidal channels which can then be taken advantage of to maximise power extraction or energy efficiency.

Initial analytical models of a single rotor in unbounded atmosphere were developed in the early 20^{th} century. Lanchester [68], Betz [8] and Joukowsky [64] all developed simple models for the flow through an unbounded propellor: given the difficulties in scientific communication between England, Germany and Russia during the First World War it seems likely that they each developed these independently [125]. These one-dimensional models are based on balancing mass, momentum and energy across a control volume through and around the rotor, and rely on a few simple assumptions. Most importantly, that the flow can be split into a 'core flow' which passes through the rotor and a 'bypass flow' which does not (separated by a streamline), with no viscous effects and no mixing in the vicinity of the rotor. Far downstream, static pressure is assumed to return to atmospheric pressure prior to any mixing taking place. All three models are similar, and demonstrate several key features of flow around a wind turbine, such as half of the flow deceleration taking place upstream of the rotor and half downstream. They each also derived the theoretical upper limit of energy extraction which such a turbine can achieve: $\frac{16}{27}$ or 59% of the available kinetic

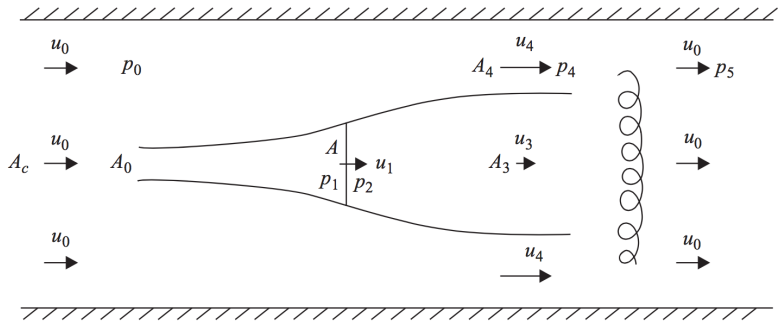

Figure 2.4: An analytical device model adapted for the case of a tidal channel. (Image reproduced from Garrett & Cummins, 2007 [46] with permission of Cambridge University Press.)

energy in the flow. This is obtained at an ideal flow speed through the rotor of 2/3 of the undisturbed flow speed. This limit is now known as the 'Betz Limit', and has been taken as the ideal maximum performance coefficient of wind turbines throughout their development. It is also frequently referenced by tidal turbine developers, as it is a well-known benchmark, however the model uses assumptions applicable to wind turbines in the open atmosphere. As such, it includes assumptions such as the downstream induction factor at the static pressure recovery point (the ratio of downstream flow speed to undisturbed upstream flow speed) being twice the induction factor at the disc plane. This is a consequence of assuming full static pressure recovery downstream of the wind turbine as the flow through the turbine regains atmospheric pressure. This and other assumptions need to be amended to provide a more accurate representation of a tidal turbine in flow bounded by a free surface or channel edges.

This amendment was carried out by Garrett & Cummins in 2007 [46], who revised the wind turbine assumptions to those likely to prevail for single tidal turbines: a relatively shallow channel with a bounding free surface and a total depth not likely to be more than a few turbine diameters in total. This makes the area of the tidal turbine significant compared to the cross-sectional area of the channel; the ratio of these two areas is referred to as 'blockage', ie the proportion of the channel's cross-sectional area blocked by the turbine. Given the incompressibility of water and the

proximity of bounding surfaces, the assumption of downstream static pressure returning to atmospheric (or upstream) pressure is unrealistic when blockage is significant. This assumption is replaced by a requirement for downstream flowspeed to return to upstream flowspeed, following static pressure equalisation across the channel and subsequent mixing of core and bypass flow. The channel set-up for this model is shown in Figure 2.4. Reframing the equations in this form changes the relationship between upstream and downstream speeds such that it is no longer true that half the flow deceleration takes places upstream and downstream of the rotor. It also shifts the point of maximum energy extraction away from an induction factor of 1/3, and increases the theoretical maximum of energy extraction by a factor of $\frac{1}{(1-B)^2}$, where B is the blockage ratio defined previously. This indicates that tidal turbine efficiency can actually exceed the Betz limit in blocked flow, extracting a higher proportion of the available kinetic energy. It should be noted, however, that this energy 'extraction' refers to all energy removed from the flow, not just the energy successfully converted into electricity (or any other form of useful work).

The Garrett & Cummins model assumes a rigid lid, i.e. no free-surface deformation between upstream and downstream of the tidal turbine, which is justified by restricting the model's applicability only to channels with relatively low Froude number (particularly when blockage becomes high). This restriction was addressed by Whelan [134], following experimental work to investigate free-surface deformation as discussed in Section 2.1.1.2. Her revised model allows for solution of the case where the free-surface deforms over a single rotor, so long as the flow remains subcritical. This showed that increasing Froude number increases the available extractable power, with the model validated through the experimental work for high and low blockage conditions. Draper *et al.* [34] extended the model further to include an expression for the downstream mixing, allowing device efficiency to be measured and also enabling the analytical actuator disc model to be embedded within the computational solution

of the shallow water equations. Arrays of multiple rows of turbines were also considered, and are discussed further within Section 2.2.2. Similarly, Vogel *et al.* [132] proposed a correction for two-dimensional depth-averaged computational simulations based on an LMADT model.

2.1.2.1 Blade Element Momentum Theory

Blade Element Momentum theory (BEM) was originally developed by Glauert in 1935 [47]. It is a revised formulation of the momentum equations used in actuator disc modelling, which allows for variation of thrust and flowspeed across the disc. The theory discretises the disc into multiple annuli, which can then model the properties of a turbine at any radius. Assuming an infinite number of blades, the turbine's blade properties (i.e. lift and drag coefficients) are then smeared around the rotor at each radius to create a homogenous axisymmetric model. Corrections are made to account for the number of blades being finite, and to correct for three-dimensional effects such as tip loss [109]. Given that BEM allows modelling of a turbine blade's true lift and drag characteristics as opposed to the homogenised single thrust coefficient for an actuator disc, while still being an efficient method numerically, it has become a popular tool for modelling wind turbines [13]. It has recently been adapted for tidal turbine modelling by both Masters *et al.* [76] and by Vogel [130], the latter including a blockage correction which removes the wind-turbine assumption that the induction factor at the downstream pressure equalisation point must always equal twice the induction factor at the disc plane, as previously discussed for the actuator disc models.

2.1.3 Computational Modelling

Although this thesis is not focused on the use of computational modelling methods, a large amount of research is devoted to such methods because they can enable de-

tailed design of turbine rotors without the requirement for repeated experiments. If computational efficiency improves further, they could also be used for detailed design and optimisation of large arrays of turbines within realistic bathymetry for a designated tidal site. Computational studies also inform experimental and analytical work undertaken, and vice versa. An overview of computational modelling methods available, and of the main highlights of modelling to date in each area, is therefore given here and in the later array-scale and basin-scale sections.

As with all modelling of tidal turbines, computational fluid dynamics (CFD) methods are largely based on historical work previously developed for wind turbines, with modifications to make the modelling techniques more applicable to the tidal context. The majority of these methods are based on simplified application of the governing Navier-Stokes equations, in particular the Reynolds-Averaged Navier Stokes (RANS) equations which are generated through Reynolds decomposition of the flowspeed into average and fluctuating terms. Substituting this decomposition into the Navier-Stokes equation and taking a time average gives the following governing equation of RANS:

$$\frac{\partial \bar{\mathbf{u}}}{\partial t} + (\bar{\mathbf{u}} \cdot \nabla)\bar{\mathbf{u}} = -\frac{1}{\rho}\nabla \bar{p} + \nu \nabla^2 \bar{\mathbf{u}} - \nabla \cdot \overline{(\mathbf{u}'\mathbf{u}')} \tag{2.1}$$

where $\mathbf{u}$ is the three-dimensional velocity vector, $\bar{\mathbf{u}}$ denotes the time-averaged value, $\mathbf{u}'$ denotes the fluctuating component, p is pressure, ν is kinematic viscosity and ρ is fluid density. The other governing equation of RANS is the continuity equation:

$$\bar{\nabla} \cdot \bar{\mathbf{u}} = 0 \tag{2.2}$$

In order to solve these equations, the turbulence effects (which are confined to the $\overline{\mathbf{u}'\mathbf{u}'}$ term commonly known as the Reynolds stress tensor) must be replaced by another term which can be more easily calculated. In general, this is done by relat-

ing it to an additional viscosity-type term, sometimes described as an eddy viscosity. This allows the time-varying terms to be replaced by average values to enable solution of the equations in a discretised, meshed form over a fluid domain of interest. Various industry and commercial codes such as ANSYS Fluent, OpenFOAM, STAR-CCM+ and others are available to implement this, with multiple options of 'turbulent viscosity' closures which can be applied as required.

Other numerical modelling options do exist which are not based on RANS; the most commonly used within tidal energy is Large Eddy Simulation (LES). Rather than using Reynolds averaging to simplify the Navier-Stokes equations, this approach applies a spatial filter to the Navier-Stokes equations, such that only scales greater than the filter scale, i.e. 'large eddies', are resolved. Smaller-scale structures are indirectly modelled with a subgrid-scale model. This allows modelling of strongly anisotropic flows dominated by large-scale structures very well, which is an advantage over the RANS modelling methods. LES has been used successfully in the wind industry [103] and has now been adopted for tidal turbine modelling as well. It does have significant drawbacks for modelling full-scale devices, since its computational cost is strongly dependent on Reynolds number. Additionally, where any solid boundaries and hence boundary layers are present, LES is considerably more expensive than RANS because its mesh resolution increases rapidly due to the requirement to resolve small-scale turbulent structures.

It is also possible to carry out simpler two-dimensional modelling by numerically implementing the shallow water equations across a discretised mesh: this is typically used for larger-scale modelling such as that of coastal basins where the flow can be treated as essentially two-dimensional.

2.1.3.1 Embedded Actuator Methods

Actuator methods are the simplest form of computational modelling regularly used to model single tidal turbines, and are based on the simple representation of any tidal device as a pure momentum sink, created in appropriate areas of the modelling domain where the device is present. These methods are often computationally simple enough to allow modelling of arrays.

The simplest version of this is an actuator disc or strip: an area of cells with a momentum loss term (equivalent to a force term) to model the presence of a turbine. Within a 2-dimensional grid or 3-dimensional meshed domain, actuator disc models can be solved with relatively low computational cost. However, they have drawbacks similar to those of porous discs in physical experiments; they cannot create rotational effects such as swirl or tip vortices in the flow. Due to their computational efficiency, though, they are popular for use in simulations where computational resources are limited or large/multiple simulations need to be performed. Early work using an in-house CFD code was carried out by MacLeod *et al.* [71]. Further instances of actuator disc modelling of single tidal devices in CFD include the work of Sun *et al.* [118], looking at both 2D and 3D models and validating the results against their experimental work, and Gant & Stallard [44] who investigated the use of unsteady RANS methods to improve turbulent behaviour. Harrison *et al.* [52] developed an embedded actuator disc method validated against experimental tests on single porous discs carried out by Myers & Bahaj [84]. The actuator disc method continues to be used, although given improvements in computational efficiency it is now more effectively used for complex scenarios such as multi-turbine arrays, as discussed in Section 2.2.3.

Actuator line models can also be employed. These were developed by Sørensen & Shen [112] for wind turbine simulations, and subsequently adapted to be embedded into RANS or LES solvers. Instead of representing a turbine as a single homoge-

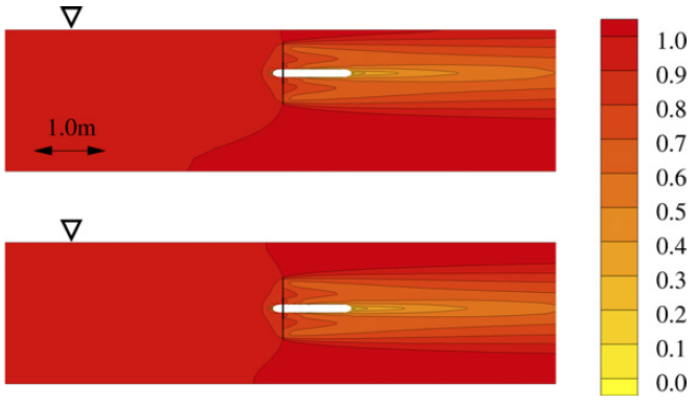

Figure 2.5: Contours of normalised velocity through a rotor in a BEM-CFD model, shown at two different submergence depths. (Image reproduced from Malki *et al.* 2013 [74] with permission of Elsevier.)

nous disc where force terms are applied, these represent individual turbine blades by lines of point forces. Embedded within a CFD model, these actuator lines can be rotated to move as a turbine, and thus introduce rotational effects on the flow from the turbine's presence which actuator disc models cannot replicate. While computationally more expensive than actuator disc modelling, this is still more efficient than CFD with fully-resolved rotating blades, and so has become popular for tidal turbine modelling. Single device models have been created for wind turbine cases [122] [104], but for tidal turbines actuator line modelling has mostly only been deployed for more complex array modelling, where its computational efficiency and improved accuracy over actuator disc models are most valued.

2.1.3.2 Embedded Blade Element Modelling

Blade element models can also be embedded within a CFD simulation to provide an improved version of an actuator disc simulation. This allows real turbine blade properties of lift and drag to be applied within the simulation, and also includes some three-dimensional effects through the addition of a swirl velocity and more accurate representation of blade loading with tip loss modelling. This works iteratively by calculating velocity terms within the CFD model, inputting those to the BEM model,

calculating resulting forces and momentum impact, then substituting those back into CFD and recalculating the velocity field. This is a computationally efficient model which requires no CFD modelling of complex areas such as boundary layers at the turbine itself. As such, it is frequently used in array modelling, but has also been used for modelling single turbines, as for example done by Malki *et al.* [74]. A set of velocity contours from this work is shown in Figure 2.5. Power and thrust coefficients of a rotor can be reasonably well matched to experimental results using this method, and as such it has significant value for modelling feasibility of turbine designs in terms of turbine loading and power output, as carried out by Hunter [54].

2.1.3.3 Blade-Resolved Modelling

The most computationally intensive form of numerical modelling is what is known as 'fully resolved' or 'blade-resolved' modelling, where all solid surfaces within the flow are fully represented: i.e. turbine blades, hub, support structure, seabed etc. This requires detailed meshing of all areas where boundary layers are present in order to capture the small turbulence scales properly, which strongly increases computational cost. Only a small number of blade-resolved CFD studies have been carried out at full deployment scale: McNaughton *et al.* [79], Sequeira and Miller [106] and Fleming [41] [40] all modelled Tidal Generation Limited's 1 MW turbine, which has a diameter of 18 m. The majority of other blade-resolved studies have, to date, modelled experimental scale turbines, often enabling comparisons between the CFD results and experimental results. For example, the experimental rotor reported in Bahaj *et al.* [3] has a sufficiently full data set attached that it has been used for validation of CFD models by McNaughton [77] and Afgan [2], who carried out both RANS and LES simulations of the same rotor. In general, blade-resolved CFD models provide the most accurate computational representation of tidal turbines.

2.2 Array Scale Modelling

In order to achieve significant amounts of energy extraction, multiple tidal turbines will have to be deployed at any potential site, forming an array of turbines similar to wind turbine arrays or 'wind farms.' Even the commercial prototype SeaGen installation in Strangford Narrows, consisting of two rotors mounted to the same cross-beam, is an array of sorts with the potential for interaction between the two rotors, affecting both rotors' performance. Given the constrained space requirements for many tidal sites, complex bathymetry and tidal turbine wakes which persist far downstream, tidal arrays cannot be constructed similarly to wind farms where the spacing aims to minimise interactions between turbines. Investigation of array behaviour, and interactions between turbines, is therefore a priority as the industry moves into the first commercial array deployments, and much work has been undertaken across all forms of modelling to understand the behaviour of tidal turbines in various array layouts.

For the purposes of this review chapter, an 'array' is defined as any local group of turbines (2 or more) which is modelled within its local flow, but does not extend to modelling many tens of turbines individually within tidal farms, where modelling of the wider flow and bathymetry in the surrounding tidal basin is required: these are discussed in Section 2.3.

2.2.1 Experimental Modelling

Even more than single device modelling, experimental array modelling is restricted by the size of experimental facilities available, as multiple devices need to be modelled. Reducing the size of devices reduces the Reynolds number and potentially makes the results less applicable to full-scale turbines, so most array modelling is carried out in relatively shallow channels with a reasonable width/depth ratio. The exception to this is devices being modelled in each other's wake, where the length of the channel

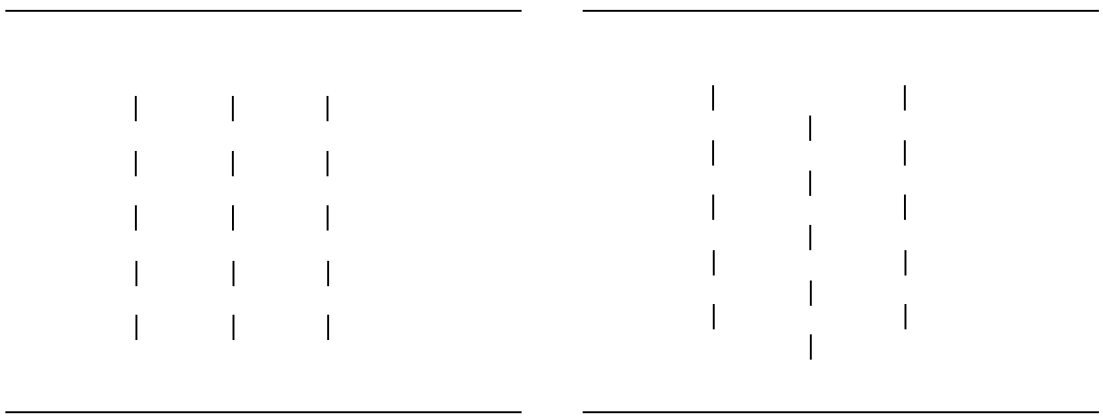

(a) In Line (b) Staggered

Figure 2.6: Simple illustration of a) in line and b) staggered configurations for multi-row arrays.

matters more than the width. A small amount of research using small-scale array models is also being undertaken in open water to avoid these constraints, although there are additional considerations of consistent inflow and the ability to fully measure the flowfield.

When testing multiple scale models in an array configuration, there are obviously limitations on how many devices can be arrayed in the testing facility, and an inability to simulate all possible configurations, even for a small number of devices. Such testing is often used to validate numerical models so that further configurations can be investigated computationally. The research discussed below, therefore, is focused on a small number of array configuration types: devices in line behind one another; and devices side-by-side across the flowstream. When multiple row arrays are considered, the configurations considered are 'in line' or 'staggered' arrangements, as simply shown in Figure 2.6.

Figure 2.7: Experimental set-up of three porous discs in a staggered, two-row configuration. (Image reproduced from Myers *et al.*, 2011 [86] with permission of Elsevier.)

2.2.1.1 Porous Discs and Strips

As for single devices, porous discs are an attractive option for array modelling due to their ease of manufacture, low cost and easy modification. They also have the benefit of being easily able to replicate exactly the same resistance to the flow across multiple discs simultaneously. Using rotors requires a control system to ensure the same tip speed ratio is achieved and maintained across all rotors in order for this to be true. As porous discs do not introduce this complexity, they have been used extensively in experimental array modelling.

Porous strips (usually rectangular in shape) can also be used to model an entire array as an area of resistance to the flow. An example of this is Daly *et al.* [24], who mounted a single 100 mm $\times$ 300 mm porous strip at varying distances from the side wall of a flow channel. This was done to investigate the effects of positioning an array either centrally or off-centre within a tidal channel. Array positioning closer to the edge of the channel was found to lead to lower intensity, more diffuse wakes downstream, but this came at a cost of increased velocity close to the channel edge and thus potentially increased scour in a real tidal channel.

Myers *et al.* [86] [85], meanwhile, investigated the case of two porous discs side by side with varying separation. They found an increase in thrust at the closest

spacing (0.5 disc diameters between disc edges), identifying that the wakes of the two discs merged downstream to become a single wake. The flow between the discs was also slower than the inflow velocity. For a wider spacing of 1 disc diameter, a 'jet' of high-speed flow was identified between the two discs, persisting some distance downstream, so that the wakes merged further downstream than in the closest case. Increasing the spacing to 1.5 disc diameters prevented the wakes merging at all in the 25 diameter downstream distance observed. They also investigated the case of a '2-row' array: in this case, a single third disc placed downstream of the two parallel discs at 1.5 diameter separation, within the accelerated jet flow created between them. This arrangement is shown in Figure 2.7. It was found to be subject to a higher thrust force than the two upstream discs. The wake from this disc was seen to merge with that of the two upstream discs, as well as appearing to contribute to their earlier dissipation and re-acceleration. An opportunity to optimise the performance of staggered turbine arrays through careful choice of inter-turbine spacing was identified.

Xiao *et al.* [137] investigated the behaviour of porous discs placed directly downstream of each other. They found that, in an array of 4 discs placed in a line downstream, the third and fourth discs had similar loading and similar wake patterns, and thus concluded that the array effect was fully developed by disc 3 and that disc 3 and its wake was a good representation of a disc in an infinitely long array. They found that the first disc in such an array experienced higher thrust. They also found that velocity deficit was slightly decreased immediately behind the fourth disc of a 4-disc array versus a single porous disc, however the TKE values were significantly higher and the wake persisted further downstream overall.

2.2.1.2 Scale Rotors

A configuration of three 3-bladed in-line scale rotors was investigated by Jo *et al.* [62] and used to validate a CFD model. The rotors were aligned, with hub separations of 1

diameter and 1.5 diameters tested. The rotors were free to rotate, and their rotations per minute (RPM) were recorded to evaluate the interactions between them. It was found that a significant drop-off in rotor speed occurred between the first and second rotors and between the second and third, in the order of 15% at 1 m/s flow speed. From the data available, it was projected that adding additional rotors downstream would lead to additional losses.

Mycek *et al.* [82] similarly studied two 3-bladed in-line rotors, having concluded that the dataset presented by Jo *et al.* [62] was insufficient for comparison to other work. Their study varied the turbulence intensity in the flume, with one test carried out at 3% freestream turbulence intensity and one at 15%. They instrumented only the second rotor in the configuration, but were able to compare its performance to a single rotor studied in [81]. They found a very significant drop in power coefficient for the low turbulence case, with even as large a rotor separation as 10 diameters leading to a drop-off of 50% in power for flow with 3% turbulence intensity. However, they found significantly more promising results for the 15% turbulence intensity case, where from 6 diameters downstream the rotor performance began to approach that of the single rotor case. Wake properties downstream of the second rotor were measured and were also found to be very similar to those behind a single rotor for the high intensity cases. From these results, the authors conclude that the downstream turbine's performance in high turbulence is similar no matter the inter-device distance, and from this they project that multiple turbines could be similarly aligned behind each other without further impacting performance. However, they do highlight that this could be affected by staggered configurations which would affect the surrounding flow differently, and suggest that more experiments should be carried out on this type of array.

Stallard *et al.* [113] studied a group of up to five 3-bladed rotors arranged laterally across the flow in a 'row' or 'fence' array configuration. They compared wake

behaviour in the case of a single rotor to that of two, three or five rotors side-by-side in the same experimental facility. Flow measurements were taken up to 12 diameters downstream of the array, allowing wake evolution to be compared across the different cases. They also included the effect of waves opposing the current in some cases and studied the effect on velocity deficit and turbulence decay in the wake. For the three-rotor case, they altered the separation between rotors and concluded that the wake behaviour approached that of separate single rotors for spacings of two diameters or greater between rotor centres. However, for closer spacings such as 1.5 diameters there was an array influence on the wake behaviour, whereby the wakes were seen to merge within 4 diameters downstream. Waves opposing the flow were seen to have limited effect, increasing velocity fluctuations but not substantially changing the lateral or vertical flow profiles. Olczak *et al.* [91] also report results for multiple rows of rotors, some in line with upstream rows and some staggered, which show significant drop-off in thrust measured on the downstream rotors except where they extend into accelerated bypass flow around the edges of the array.

Olczak's work also discusses the concept of superposition of far-wake velocity profiles, allowing the wake of downstream rows to be predicted by an additive combination of single wake profiles. This superposition model is developed and explored further by Stansby & Stallard [116]. A wake velocity profile from a single rotor is superimposed onto the freestream flow behind a row array to determine inlet velocities for downstream rows of rotors; these rotors' wakes are then similarly superimposed taking into account their modified inflow velocity; and this process is repeated until the flowfield is complete. Geometric blockage corrections were applied to ensure that the same volumetric flux passed through each row. The predictions from this simple model were found to agree reasonably well with experimental results, although they tended to under-predict the velocity deficit closely behind the array. It should be noted that, while the results were not quite as well matched to experimental data as

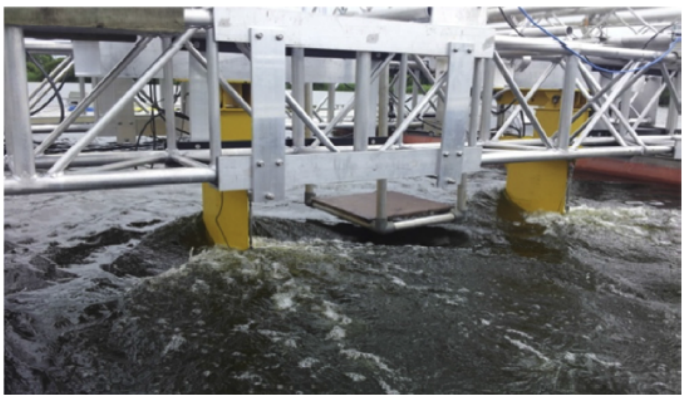

Figure 2.8: Support structure for two scale rotors being tested side-by-side in open water. (Image reproduced from Jeffcoate *et al.* 2016 [61] with permission of Elsevier.)

those produced by Olczak's RANS-BEM model as defined in [91], this method is much more efficient numerically. It is thus suited to the problem of array optimisation. The positions of rotors were allowed to move both laterally and longitudinally within the flow, with the superimposed wakes being recalculated in each case and a maximum of the net power produced by the array being sought. This yielded several interesting array configurations, which were significantly different depending on whether the flow was modelled as uni-directional or bi-directional. In the bi-directional case, which is most applicable to tidal turbines, the rotors remained broadly in parallel rows, but their spacing altered to achieve maximum power output. Note that the results of this optimisation were not validated against experimental results, though the fixed array results were.

Jeffcoate *et al.* [61] tested two larger, 4-bladed scale rotors of 1.5 m diameter in open water, using a previously designed platform to push rotors through the still water of a lake. These rotors were tested in a side-by-side configuration and a downstream in-line configuration, with measurements of rotor thrust, torque and mechanical power being taken. The support structure and rotors in the water are shown in Figure 2.8. The rotors were large enough to contain onboard electrical generators in the hubs, so full electrical power measurements were also taken. Firstly, individual

rotor performance upstream and downstream of its own support structure was tested, and found to be independent of positioning. It was noted that this may be more a function of geometry for this particular rotor/support structure combination, and less of a general result. Rotor performance in parallel was then tested, with the two rotors being placed side by side at 1.5 diameters and 2 diameters centreline separation. A slight increase in performance of each rotor was found in this configuration, of approximately 6% for each rotor (at both spacings). The rotors were then rearranged into an in-line configuration with one turbine directly behind the other and retested at 2 diameters and 6 diameters spacing. A significant power drop was witnessed on the downstream rotor, with reductions of 63% at two diameters downstream and 59% at six diameters downstream. Comparison was made to the results of Mycek *et al.* [82] and it was concluded that the low turbulence in the still lake water, considered to be lower than 3% turbulence intensity, may have been a contributing factor to this significant drop-off in power. A final configuration with the second rotor both downstream and offset from the first rotor was tested, where performance returned to match the single independent turbine case. It was therefore concluded that the wake of the first rotor was relatively narrow and did not impact rotors 1.5 diameters away from the centreline at 6 diameters downstream.

2.2.2 Analytical Modelling

Given the complexities of modelling large arrays either experimentally or computationally, a significant area of research involves developing analytical models to predict array behaviour, or upper limits of possible array behaviour, to guide future research and design. Following Garrett & Cummins' [46] adaptation of momentum theory for a single device within a confined tidal channel, others have extended the work in different ways to consider the problem of an array of tidal turbines within a channel.

Vennell [126] [127] combined the 2007 Garrett & Cummins model [46] with previ-

ous work by Garrett & Cummins [45], which focused on the flow through a channel between two tidal basins, and the reduction in that flow when resistance is presented to the flow in the form of tidal turbines. Combining the two models allowed Vennell to produce an analytical model which accounted for a reduction in flow speed when tidal turbines are placed in the flow, so long as the tidal turbines are considered to occupy only a short section of the total length of the channel. Given that the 2007 model of Garrett & Cummins could equally model a single device or multiple devices with the same operating parameters, this allowed Vennell to model a tidal 'farm' of either a single row of identical turbines or multiple rows of them (with the assumption that the arrays were far enough apart for there to be no wake interaction). A number of findings resulted from this work, in particular the need to 'tune' tidal turbines to achieve optimal performance in different channel conditions: this has particular implications for array development where part of an array is built first, and then more turbines are added later, since the optimal tuning for the first turbines installed will no longer be optimal once later turbines are built. It was also found that, if designing an array to minimise the total number of installed turbines (and hence, most likely, the cost) then the number of turbines per row should be prioritised over the number of rows in an array: arrays with fewer rows and more turbines per row perform better. This model does however make some assumptions which may not be true for all arrays: in particular, it assumes that the turbines are spread equally across a channel, each occupying the same local proportion of channel area.

The work of Vennell was combined with the work on single actuators by Whelan *et al.* [134] and Draper *et al.* [34] to allow analytical modelling of potential turbine arrays in a real tidal site at the Bay of Fundy by Karsten *et al.* [65]. They found that such arrays could potentially generate up to 2500 MW of power with only a 5% reduction in flow rate through the tidal channel of interest. They then considered constraints on turbine location such as channel depth, and studied the rate of power

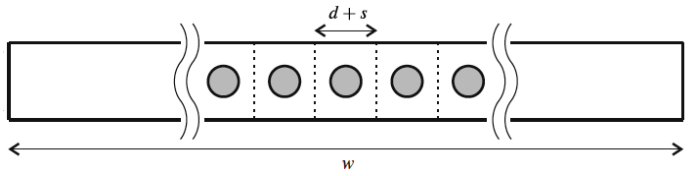

Figure 2.9: Cross-section through a 'partial array' of devices which only partially span the width of a tidal channel. (Image reproduced from Nishino & Willden 2012 [87] with permission of Cambridge University Press.)

increase as additional turbines were added to the model, demonstrating that the potential size and power of any array is strongly restricted by the locational constraints on where turbines can actually be placed.

Draper *et al.* [34] considered arrays of rows of turbines as well as single devices, and is one of the few studies to recommend increasing the number of rows within an array. This is based on a measure of turbine efficiency calculated as a ratio of power extracted at the turbine to total power extracted from the flow (i.e. including mixing losses downstream, though excluding bed friction in this case). This prioritises low head drop across turbines and as such more rows with fewer turbines, exerting lower thrust on the flow, are preferable. This does not, however, mean that greatest overall power extraction can be achieved with such a configuration.

Nishino and Willden [87] took a different approach from Vennell to allow a 'partial array' to be modelled, spanning only some of the width of the channel, as shown in Figure 2.9. Working only from the Garrett & Cummins 2007 model, they defined two different scales of fluid behaviour, device-scale and array-scale. By making the assumption that these scales are entirely separate due to mixing lengths of one device versus a long row array, they were able to replicate the Garrett & Cummins model inside itself at the two separate scales. In this new model, the concept of 'blockage' - the area ratio of device cross-sectional area to local channel area - becomes more complex, as in the inner model the local channel area effectively becomes the cross-sectional area of channel around that device only. The blockage for this inner model

is referred to as 'local blockage', while the effective blockage of the outer array model - the ratio of total array width to channel width, assuming depth is constant across the channel - is referred to as 'array blockage.' Equating the total device thrust at both scales enables the inner and outer models to be coupled, and the performance of the entire 'partial array' to be analysed. Individual devices are again assumed to be identical to one another, and it is also assumed that the row array is sufficiently long that expansion effects in the local channels can be ignored. An optimal combination of local and array blockages could be found for any device (with characteristics defined by its total induction factor), and that the theoretical maximum of energy extraction exceeded that predicted by Garrett & Cummins [46]. A correction to this model was later developed, also by Nishino & Willden [88], to allow for shorter row arrays where expansion in the local channels was possible. This was done through the introduction of flow expansion factors, whose relationship to the number of turbines was approximated by a power law. It was still assumed that all devices have the same induction factor, and that all local channels have the same expansion factor. This revised model was compared to a 3D-RANS model with embedded actuator discs. The results of predicted power and thrust coefficients were found to have reduced slightly from the original partial array model of [87], bringing them closer to the RANS results although still slightly higher. The closest match to the RANS simulation occurred with highest simulated turbulence.

Vogel *et al.* [131] amended the original Nishino & Willden model for a long row array [87] to include a deformable free-surface and the effects of Froude number, analogous to the correction carried out by Whelan *et al.* [134] for the original Garrett & Cummins model and including the downstream mixing as developed by Draper *et al.* for a single device [34]. This showed a similar improvement in array performance at higher Froude numbers to that seen by single device models, due to a reduction in bypass flow cross-section caused by increased deformation of the free surface with

increased Froude number.

Draper & Nishino [35] also revisited the original Garrett & Cummins 2007 model [46] to consider rows of tidal turbines placed in an in-line or staggered configuration. To allow downstream rows to be modelled, they assume that streamwise spacing between rows is sufficient for pressure equalization to occur, but not sufficiently large that significant wake mixing has occurred in the upstream wakes. This allows in-line downstream actuators to be placed within the wake of an upstream actuator while maintaining conservation of energy in all surrounding streamlines, thus enabling the equations to be closed and solved. In the case of staggered devices, conversely, the downstream actuator is defined as being in the bypass flow of the upstream one. It was found that the performance of staggered devices was dependent on global blockage, since in the entirely unblocked case the bypass flow speed would not alter due to the presence of the upstream device and as such the downstream device would behave as an independent device in unconstrained flow. This model identified a trend of power coefficients across various array configurations with one or two rows as follows: maximum power was found for a single row with all turbines in the same plane; then two rows of staggered turbines with close spacing such that accelerated bypass flow can be exploited; then two rows of staggered turbines with large separation between the rows; and finally lowest power for two rows of rotors in-line behind each other. A recommendation was therefore made that, where possible, turbines be placed in a single row array in the same cross-stream plane.

2.2.3 Computational Modelling

Computational modelling of arrays is limited by the scale and complexity of the problem. As such, computationally intensive methods such as blade-resolved RANS simulations are usually not appropriate, and simpler embedded models for the turbines are used. Most studies to date have focused on either replicating experimental

data to validate computational methods, or evaluating potential array layouts.

2.2.3.1 Actuator Methods

An actuator strip was embedded in a RANS implementation by Daly *et al.* [25] with varying velocity inlet profiles, with previous experimental work [24] using a porous strip used to validate the numerical results. A 1/8th log law velocity profile specified at the upstream boundary was found to provide the best fit to experimental results. An uncertainty was also raised regarding the design of the porous strip, and the lack of guidance available on hole distribution to achieve a uniform resistance to the flow. Generally, though, the numerical results were found to provide a good match to the experimental ones.

Bai *et al.* [7] used an embedded actuator disc approach to model arrays of 1, 2 and 3 rows of staggered turbines in a 3D RANS simulation. They found improvements in power performance due to the blockage effect when additional devices were added in the same row, but did not find this same effect when more rows were added downstream. Additionally, they found a feature whereby moving downstream rows further downstream, away from the upstream rows, caused a drop-off in power, which was counter to their expectations that row arrays would perform better when more widely separated down a channel.

Hunter *et al.* [55] embedded a varying number of actuator discs in 3D RANS simulations and used them to investigate the possibilities for 'tuning' each turbine's resistance to the flow, i.e. allowing actuator discs in different positions to present varying resistance to the flow. This was then used to investigate a number of theories regarding the optimal arrangement of row arrays, in particular whether best performance is achieved with a single row or with a staggered array. Arrays of 4, 7 and 8 devices were modelled within a channel to investigate this. Figure 2.10 shows the variation in static pressure upstream and downstream of a 7-device array from this

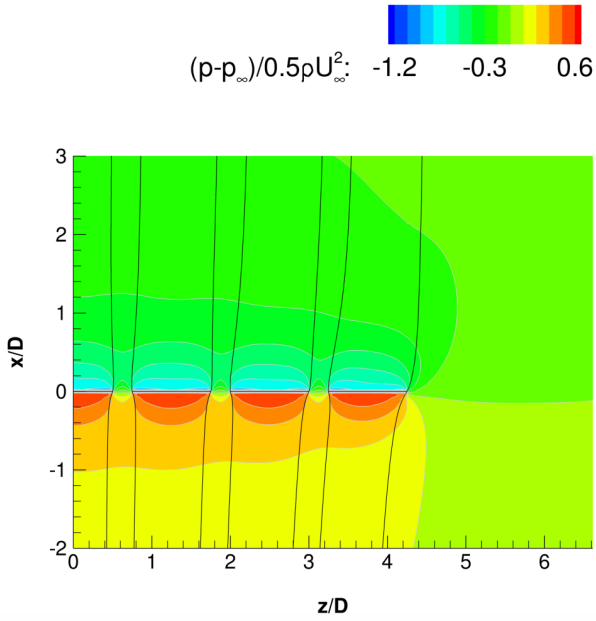

Figure 2.10: Contours of pressure coefficient around a row array of seven actuator discs. Flow is in the positive x-direction. (Image reproduced from Hunter, 2015 [54] with permission.)

work. The findings showed that, within a single row of devices, optimal power performance was achieved with a uniform resistance coefficient across the array. When the array was then staggered, power was seen to drop off with increasing distance between upstream and downstream turbines. It was not seen to be possible to increase the total array power coefficient above the maximum that was achieved with a single row with uniform resistance. However, it was found that if an array were staggered, its performance could be slightly improved by tuning the downstream discs to have lower resistance than the upstream ones. This was also found to have the added benefit of making thrust distribution more similar across all discs. However, this result was obtained in uni-directional flow. For a bi-directional flow such as most tidal sites, therefore, the tuning of upstream and downstream rows would need to be varied between flood and ebb tides to achieve this performance.

Churchfield *et al.* [20] used an actuator line method embedded in an LES simulation to investigate two effectively infinitely wide rows of turbines, in staggered

and non-staggered configurations. They came to the same conclusion as several other studies regarding staggered versus non-staggered downstream rows, namely that rows staggered to place downstream turbines in the location of flow which has been accelerated between upstream turbines produce significantly better performance than rows which are not staggered in their positioning. They also found that the performance of non-staggered rows improved with increased streamwise separation between rows. Their use of LES and rotating actuator line models also enabled them to study the potential for counter-rotating turbines and the existence of asymmetric wake behaviour. They concluded that counter-rotating turbines offered limited benefit. Asymmetric, sometimes meandering wakes, as developed within their model, were concluded to be an inevitable consequence of a sheared inflow profile causing a sheared rotating wake flow. This can be visualised by imagining a sheared inflow profile into the wake which, within a 90° rotation downstream, now has higher streamwise velocity on one side than on the other. Conclusions were also drawn regarding the minimum domain size necessary for LES to simulate the largest turbulent structures within the flow.

2.2.3.2 Blade Element Models

Embedding BEM models of turbines within a RANS simulation, so-called coupled RANS-BEM or RANS-BEMT modelling, has become an increasingly popular way of studying small arrays, and a number of different areas of interest have been investigated recently using this methodology.

Turnock *et al.* [123] simulated a single turbine in a domain of varying widths, representing a turbine within an infinitely wide array, with lateral separation equal to the domain width. Downstream wake measurements were also taken to estimate the performance of potential further turbine rows downstream. It was found that power capture was maximised when lateral separation between turbines in the same row was minimised, but longitudinal separation between rows of turbines was maximised.

Malki *et al.* [72] also used a coupled RANS-BEM model to study a variety of arrangements of turbines. They investigated the available power in the flow accelerated between two upstream turbines towards a downstream turbine positioned in a staggered configuration between them. It was found that the power output of the downstream rotor was a function of both lateral spacing between the upstream turbines and longitudinal spacing to the downstream one: generally, lower longitudinal spacing was required with lower lateral spacing, until lateral spacing became sufficiently low that upstream turbine wakes impinged on the downstream turbine. Optimal downstream positioning was found to be less than two diameters behind the upstream rotors for most configurations. Further work was carried out [73] to additionally investigate two laterally spaced rotors alone and two longitudinally spaced (in line) rotors alone, as well as carrying out a study on an array of 14 turbines. The performance of the downstream rotor was found to suffer in the in line configuration, as has been reported in other studies, with performance recovering towards that of a solo turbine the further downstream it is placed. Lateral spacing closer than two diameters did not affect the performance of the two laterally spaced turbines, but was found to hinder flow recovery downstream. Finally, the 14 turbine array was compared in two configurations: that of a staggered 4-row arrangement with equal spacing between all rows; and a configuration where the first and second staggered rows were brought much more closely together, with the third and fourth rows further downstream and equally closely spaced with respect to each other. These two configurations are shown in Figure 2.11. The altered configuration was chosen based on the trends witnessed in the two- and three-rotor cases. It was found that this alteration achieved a 10.7% power performance increase.

Schluntz & Willden [105] used a coupled RANS-BEM model to design rotor geometries for specified blockage ratios, representing rotors in row arrays with different spacings. They ran simulations of single rotors at these blockage ratios and iteratively

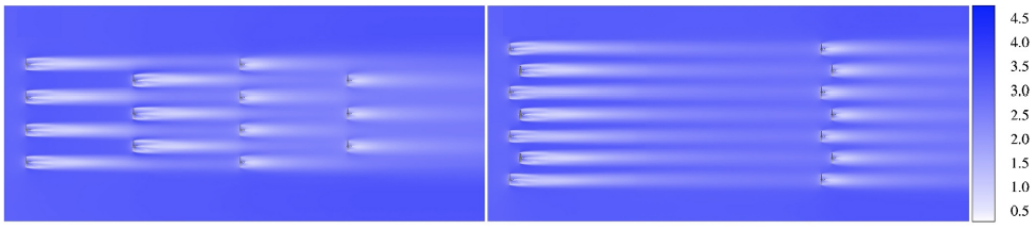

Figure 2.11: Velocity fields around two staggered array configurations of 14 rotors, one conventionally spaced (left image) and one adjusted according to studies of lateral and longitudinal spacing (right image). (Image reproduced from Malki *et al.* 2014 [73] with permission of Elsevier.)

adjusted the rotor blade chord and twist to achieve the highest possible power coefficient. Having done this for four different blockage ratios, the performance of each specific rotor design was then tested in other blockage cases, i.e. off-design blockage conditions. The rotor designed for highest blockage, i.e. closest lateral spacing to other turbines in a single row array, was able to achieve the highest power coefficient. However, it would also need to be designed to withstand the highest thrust coefficient. The rotors designed for higher blockage condition had significantly higher solidity and slightly lower twist. When operating rotors away from their design blockage, all rotors witness an improvement in performance under high blockage, as might be expected. Operating a rotor in a blockage condition for which it was not designed was found to lead to performance up to 21% below that of the rotor designed for that blockage condition. It was also found that the rotor designed for highest blockage imposed greater than optimal thrust forces on the flow, extracting maximum power at the cost of increased mixing losses.

Bai *et al.* [6] used a RANS-BEM method to model three turbines mounted to a triangular support structure. Having validated their model for a single turbine against the Bahaj *et al.* [3] experimental results, they investigated the effect of flow directionality by simulating the support structure in three different rotational positions relative to the incoming flow, and with differing inter-turbine spacings. Turbines downstream of other turbines' wakes were found to suffer significant performance

losses. A revised support structure design placing the turbines in the same lateral plane, with one vertically above the other two instead of longitudinally behind them, was proposed to avoid these issues.

Olczak *et al.* [91] carried out a series of RANS-BEM simulations of the experimental work undertaken by Stallard *et al.* [113] [114], as well as comparing the simulation results to the wake superposition model developed by Stansby & Stallard [116]. The RANS-BEM model generally gave good agreement with experimental data for in-line arrays when appropriate turbulence models were applied, however it was found to consistently over-predict thrust on a row array by around 10%. It was also less good at predicting the flowfield for the case of a staggered array where downstream rows were laterally offset from upstream ones. The error in thrust prediction increased for downstream rows, with up to 38% discrepancy seen in the final row of a 3-row array.

2.2.3.3 Other Methods

Due to the computational complexity of performing blade-resolved simulations on multiple rotors simultaneously, this method is not popular for array simulations. Early work by O'Doherty *et al.* [90] used such a simulation to investigate the behaviour of a support structure with 5 turbines, and to evaluate the required coefficient of friction between frame and seabed to prevent movement if no other fixings are used. The five turbines were arranged in a V-pattern. It was found that the power performance of the array was reduced by approximately 12% when the structure was arranged such that the apex of the V was upstream as opposed to downstream in the flow. The turbines at the ends of the two arms were found to extract most power from the flow in either orientation. It was also found that the requirement on sliding prevention through bed friction would not be achieved for a standard steel/concrete frictional interface, and as such additional anchorage or piling would be required.

Carlier *et al.* [16], by contrast, used a different computational implementation,

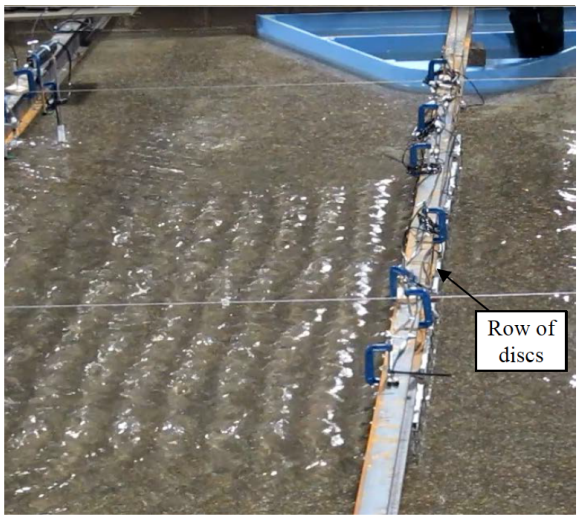

Figure 2.12: Set-up of experimental arrangement including a headland model and a row array of porous discs. (Image reproduced from Draper *et al.* 2013 [36] with permission from EWTEC.)

of panel-based turbine representation with vortex methods to allow a representation of turbulence in the flow. They investigated the case of two in-line turbines and three staggered turbines, and compared them to the experimental results reported by Mycek *et al.* [82] and Kervella *et al.* [66] respectively. Good agreement was found for the in-line turbines, but less so for the staggered arrangements of three turbines. The effect of ambient turbulence is also highlighted and proposed for further investigation.

2.3 Basin Scale Modelling

As highlighted in Section 2.2, 'basin scale' modelling for the purposes of this review is considered to be any work that takes into account the wider area around a tidal installation, including realistic bathymetry, coastlines and tidal forcing. The complexity of modelling such a large system is obviously high, and as such only relatively simple models have been used to date to investigate this scale. Many results are also specific to a particular installation being considered due to the influence of the local tidal behaviour.

2.3.1 Experimental Modelling

Very little experimental work has been carried out to date which reflects basin-scale channel geometry and relatively large arrays. One example is Draper *et al.* [36], which included a headland model as shown in Figure 2.12. Rows of porous discs were used in this work to model turbine arrays stretching across a wide channel, with and without a headland model present, in both steady and oscillatory (i.e. bi-directional) flow. The Froude number was relatively well-matched between experiment and actual values for real tidal sites. The Reynolds number was not, however the flow was always turbulent. No significant increase in force on the porous emulators was witnessed as the rows of discs were moved closer to the headland feature. A depth-averaged numerical model was simultaneously developed and compared, with reasonably good agreement but with differences in areas where velocity deficits should exist, i.e. in device wakes or behind the headland.

2.3.2 Analytical Modelling

Garrett & Cummins [45] were the first to propose an analytical, one-dimensional model for the flow through a constrained channel between two tidal basins, with a row array of tidal stream devices extracting power within the channel. The channel is assumed to be short compared to tidal wavelength, which is reasonable for most tidal channels. Governing equations of motion for the flow through the channel are established, with the flow assumed to exit as a jet into the lower tidal basin, with an associated energy loss. A drag term proportional to flowspeed squared is introduced to represent the force imposed by the turbine fence on the flow. Given that the flow through the channel is driven by the elevation head difference between inflow and outflow, this can be balanced against flow acceleration and opposing forces from turbines and bed friction. This calculation allows a maximum power which can be extracted from the flow to be calculated, given that if the flow is too strongly opposed

it will slow down and less power will be available. The findings from this work indicate that there is an upper bound of energy that can be extracted from any tidal channel, which is calculated to be approximately $0.22\rho g\Delta h Q_{max}$ where ρ is the density of water, g is the gravitational constant, Δh is the amplitude of tidal head and Q_{max} is the maximum volumetric flux through the undisturbed channel. This value is found to depend slightly on whether bed friction or turbine friction dominate the opposing force terms. This study gives a simple relationship between a channel's geometry and bulk flow and the ability to extract power from it, and as such has been included in later analytical work focusing on arrays in channels, such as Vennell's studies [126] [127].

Blanchfield *et al.* [11] subsequently extended the Garrett & Cummins model to allow for channels which connect to the open ocean on one side but to a constrained lagoon on the other. They also developed variables to describe the bay geometry which influence the available power relationship. However, they found that the upper bound on extractable energy developed in the previous work [45] was still the average result for this new configuration, albeit with slightly wider variance.

Vennell [128] also expanded this model to investigate the types of energy loss taking place within the flow: losses to bed friction, mixing, support structure drag and actual useful energy production. Tidal channels were divided into two distinct types, large straits and shallow channels, and the behaviour of each was observed to be significantly different in terms of these types of energy loss. Large straits, where bed friction does not dominate the channel behaviour, were observed to have significantly more potential for tidal energy extraction.

Smeaton *et al.* [110] [111] have also developed these models between unconstrained basins and between a basin and a constrained lagoon to investigate the effect of channel constriction. Introducing a smoothly curved restriction in either channel width or depth, they studied the effect of varying restriction size on channel power

potential. They concluded that depth constrictions caused greater potential loss than width constrictions, although noted that this was due to their assumption that channels were wide and that bed friction did not apply on the vertical sides of the channel. They also showed that, for a channel between two large basins, introducing a constriction could only ever reduce the power potential of the channel. However, for a channel connecting a smaller lagoon to the ocean, resonant modes were possible which could lead to a peak power potential with increasing channel constriction. It was noted, however, that extracting the maximum power in any scenario such as these would result in a reduction in flow rate sufficiently large to be ecologically unacceptable in most cases.

2.3.3 Computational Modelling

Given the complex bathymetry, geometry and flow regimes of basin-scale problems, most computational modelling to date has utilised a variety of the two-dimensional, depth-averaged version of the Navier-Stokes equations, also known as the shallow water equations. Within these models, turbines and arrays can be embedded as simple frictional energy sinks, although this can lead to an over-prediction of power, as discussed by Vogel *et al.* [132]. It is preferable to use a momentum sink term based on an LMADT model of the momentum loss across an array.

Draper *et al.* [33] investigated the case of a tidal row array located next to a generalised headland, similar to the experimental case studied in [36]. The array was represented as a line momentum sink within the simulation, and resultant power extraction and flow patterns were studied. Similarities were found to the case of a tidal channel, in that available power is maximised as array blockage ratio increases. However, differences from the channel case were also identified, notably the asymmetry of array bypass flows between the headland side and the ocean side, and the fact that maximum extractable power is limited due to the ability of the flow to bypass the

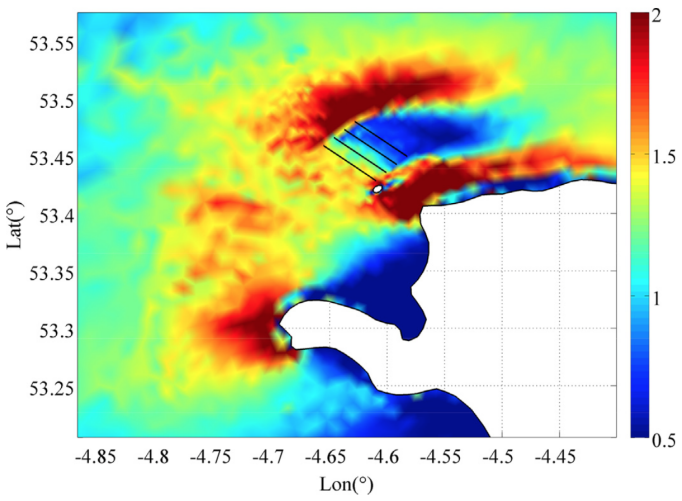

Figure 2.13: Velocity field around a potential array near the Anglesey Skerries, implemented in a SWE model including bathymetry and coastline. (Image reproduced from Serhadlıoğlu *et al.*, 2013 [107] with permission of Elsevier.)

array on the ocean side. It was also found that high residual shear stresses existed at the bed around a tidal array site, and as such the impacts on sediment movement or even coastal erosion could be significant.

Adcock *et al.* [1] and Serhadlıoğlu *et al.* [107] focused on exploring the potential of various tidal array positions within areas of interest for tidal energy in the UK, namely the Pentland Firth and Anglesey Skerries respectively. They both used an implementation of the shallow water equations with LMADT implementation of turbines embedded as described by Draper [34]. Adcock *et al.*, looking at the tidal channel site of the Pentland Firth, found that bed friction could play an important role in the available power which an array could target, particularly for small arrays. It was also found that multiple row arrays of turbines in different parts of the Pentland Firth had significant interaction with each other in how they remove energy from the flow through the whole channel. It was therefore recommended that the process of site leasing be reconsidered to reflect this. To extract the maximum potential power from the Pentland Firth, it was found that arrays would need to span the entire channel, causing up to 30% reduction in flow rate. Serhadlıoğlu *et al.*,

meanwhile, investigated the headland site of the Anglesey Skerries and the effect of placing multiple row arrays in series or parallel configurations offshore. It was seen to be better for tidal power extraction to place arrays closer to the Skerries (which are small islands just offshore from the headland), and to place rows in parallel rather than in series.

Sánchez *et al.* [101] [102], meanwhile, considered the case of a tidal estuary in the north of Spain, the Ria de Ortigueira, and used a three-dimensional model using the shallow water equations with vertical layers implemented in a domain encompassing the entire estuary to allow evaluation of vertical phenomena. They used this model to investigate the effect on transient and residual currents within the estuary caused by the presence of a tidal turbine array, concluding that the residual currents are affected more widely around the array, but that the fundamental patterns of estuarine circulation are not changed by the presence of an array. This model was also used to study differences in the resulting flowfield between an array of floating devices and an array of bottom-mounted devices, implemented as momentum sinks within the appropriate vertical layers. It was found that the floating array could extract up to 60% more power, due purely to the higher flow velocities at the top of the water column, but that the impact of the two arrays on the wider estuarine circulation was similar. However, significant differences in flow behaviour were found close to the array, where flow retardation and acceleration were seen in different vertical layers. The results from this study also highlighted the importance of site-specific modelling, since some flow behaviour was unexpected, such as surface flow speed decreasing above a bottom-mounted array despite flow diversion.

Chen *et al.* [19] carried out modelling of proposed row arrays near Zhaitang island, off the east coast of China. The turbines were again modelled as a momentum sink, within a three-dimensional domain that allowed for varying bathymetry around the island. A variety of array spacings were investigated, and similar findings to

other studies were reported: the power coefficient of multiple in-line row arrays is generally lower than for a single row, and for a single row performance improves when blockage is increased. For total power extraction, an array with the lowest lateral spacing considered (2 diameters) and moderate longitudinal spacing between rows (10 diameters) was found to best maximise the potential of the area available for tidal turbine deployment.

Instead of modelling a specific area of interest for tidal energy, Harang *et al.* [51] created an idealised model of a tidal channel linking two large bodies of water, with flow driven by tidal head forcing. This forcing allows for replication of real tidal behaviour and linking the channel to the open basins allows for replication of flow features such as a jet exiting the channel, which was seen to exist in simulation results. A number of configurations of array arrangement were simulated, some uniform, some staggered, some asymmetric across the channel. A uniform single row was still found to be optimal, but staggered arrangements which overall occupied the entire width of the channel (even if part of the array was offset downstream) were found to extract a significant amount of the available power, up to 95% of the optimal value. This may be valuable if it is not possible to span an entire tidal channel with turbines, e.g. where shipping channels are required.

Divett *et al.* [32] utilised an LES-type implementation of the two-dimensional depth-averaged Navier-Stokes equations to investigate the tuning of large arrays in tidal channels, with adaptive mesh to better resolve eddies in turbulent wakes. They simulated up to 7 in-line rows of turbines in a channel driven by tidal head forcing, and again established that there is a significant drop-off in power captured per turbine as the number of rows increases: 20 turbines are required in a 2-row array to capture more power than 12 turbines in a single row. They also found a strong linear relationship between the power extracted by any array tuned to extract maximum possible power and the resultant reduction in freestream velocity, which is in agreement with

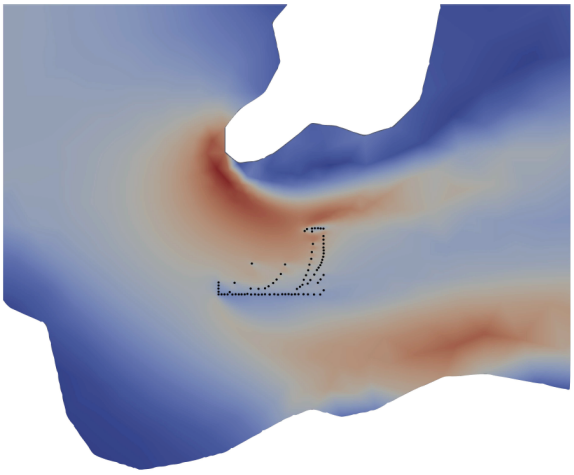

Figure 2.14: Velocity field at peak flood and array layout for 80 turbines following optimisation routines in a SWE model of the Pentland Firth Inner Sound. (Image reproduced from Culley *et al.*, 2015 [23] with permission of EWTEC.)

one-dimensional analytical models.

Funke *et al.* [43], Kramer *et al.* [67] and Culley *et al.* [23] have developed and extended an optimisation tool for tidal array development which implements turbines as bed friction terms within large two-dimensional domains modelled using the shallow water equations. A gradient-based optimisation is employed to move turbines within a specified domain according to increasing parameters of interest, such as energy extraction or cost. A standard initial rectangular layout of in-line rows of turbines was used as the starting condition for multiple simulations, carried out in idealised channels and also in a simulated region of the Pentland Firth. When the optimisation routine was applied, it was found that turbines would move away from their initial regular spacing and form fewer rows of more densely-packed turbines, including turbines lining the edges of the rectilinear area they were restricted to. These rows would be approximately perpendicular to flow direction where possible, as shown in Figure 2.14. Increases in energy extraction of up to 24% were witnessed in the Pentland Firth simulation with an array of 80 turbines. Jacobs *et al.* [58] aimed to investigate the validity of the configurations generated by this optimisation approach, and as such implemented both a two-dimensional steady-state model with high vis-

cosity and a two-dimensional LES-type model to investigate the power produced by regular configurations and by those produced by the optimisation model. The regular configurations considered were multi-row arrays, with 7.5 diameters lateral separation between turbines and 10 or 20 diameters longitudinal separation between rows, both in-line and staggered, in a generalised rectangular channel. An optimised configuration for the same number of turbines in the same channel was also considered. The optimised configuration was found to extract significantly more power than the 'standard' ones in both steady-state and LES models, in the order of 40% greater. This was despite the fact that the 'optimised' solution had not fully converged, and had asymmetry suggesting a local maximum rather than a global one. However, it should be noted that none of the 'standard' array configurations considered in any of these studies had the high blockage ratios and small number of rows indicated as optimal by many of the other studies discussed in this section, which might be expected to perform rather better than the non-optimised ones considered in these studies.

2.4 Conclusions

A large quantity of work has been undertaken to model tidal turbine behaviour at device, array and basin scale. Computational models are widely used to study individual rotor design, and to model tidal channels with varying bathymetry. Analytical models provide an opportunity for simple examination of trends and prediction of available upper limits of power extraction. Experimental models provide validation to computational and analytical work, while highlighting areas of interest that require further investigation. When considering array design, it is clear from the experimental, computational and analytical work undertaken that aligning turbines downstream of each other results in significant power losses, while aligning them side by side into a row array has the potential to increase power extraction. However, there are lim-

itations to the analytical models available for row arrays of this type, and there are only a small number of experimental studies of row array configurations of more than a few devices. This thesis will focus on addressing these limitations and providing new analytical tools for the design of row arrays of tidal turbines, supported by data from experiments.

Chapter 3

Modelling Sub-Arrays Within a Tidal Turbine Farm

Analytical modelling has been widely used in investigation of tidal turbine behaviour, both for single devices and for arrays of devices. The advantage of analytical modelling is that it is (usually) mathematically simple, requiring minimal computational capacity. It is also device-independent, as it simulates any device as a simple actuator (i.e. momentum sink) within the environment. The results of analytical theory are therefore applicable to all turbine designs, so long as their thrust behaviour is adequately captured. However, since all analytical theory in this area centres on one-dimensional models, there are significant limitations to the geometric complexity that can be sensibly modelled.

Analytical modelling has been extended in many ways since its development for wind turbines by Lanchester, Betz and Joukowsky in the early 20th century. It was first adapted for tidal turbine configurations by Garrett & Cummins in 2007 [46] and has since been applied in multiple ways to investigate potential array configurations for tidal turbines, to explore theoretical limits to power extraction [126] [127] [87] [35].

This chapter introduces the assumptions and governing equations for Linear Momentum Actuator Disc Theory (LMADT), and discusses how these have been adapted for the investigation of a single 'partial fence' array of a row of turbines partially spanning a wide tidal channel. A new model will be presented in Section 3.3 onwards to extend the concept to consider the potential of multiple co-linear partial row arrays, designated as 'sub-arrays' for clarity.

3.1 Modelling of Wind Turbines using LMADT

Modelling of wind turbines using momentum theory to gain insight into their maximum potential for power extraction was first carried out by Lanchester in 1915 [68]. It was independently repeated by Betz [8] and Joukowsky [64] in 1920, and the upper theoretical limit derived from this work is now commonly known as the Betz (or Lanchester-Betz) limit.

Linear Momentum Actuator Disc Theory (LMADT) involves a one-dimensional model of momentum balance through an actuator disc that exerts force on the flow. Several significant assumptions are made to simplify the fluid mechanics of the problem. The set-up for an actuator disc representing a wind turbine is shown in Figure 3.1. The main assumptions are: that there is a uniform 'core flow' which passes through the disc plane, surrounded by a uniform 'bypass flow' which does not, and that these two flows are separated by streamlines with no mixing across them; that the problem can be considered one-dimensional, with axisymmetric streamtube expansion; and that the size of the atmosphere is sufficiently large, relative to the size of the device, that atmospheric pressure can be assumed throughout the bypass flow. The flow is assumed to be incompressible, and irrotational while the streamtube is expanding. What occurs downstream of the point where the streamlines become straight and parallel is not modelled, and turbulent mixing is assumed to occur there.

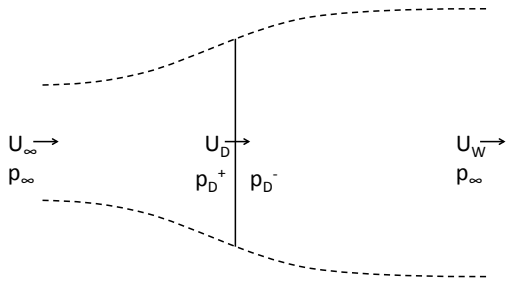

Figure 3.1: Illustration of a streamtube expanding around an actuator disc in unconfined flow.

A full derivation is given in Burton *et al.* [13], however the following provides a summary of the governing equations. Firstly, conservation of mass along the core streamtube is used to create geometric relationships between the flow speeds at each location:

$$\rho A_\infty U_\infty = \rho A_D U_D = \rho A_W U_W \tag{3.1}$$

where ρ is air density, A and U denote areas and flowspeeds respectively, and the subscripts are as follows: ∞ for the far upstream freestream flow prior to any expansion, D for the disc plane and W for the point in the wake at which pressure p returns to p_∞ and the streamlines become straight and parallel. This allows each flowspeed to be expressed in terms of the others through an area ratio. For example:

$$U_D = \frac{A_\infty}{A_D} U_\infty \tag{3.2}$$

for the relationship between flowspeed at disc plane and inflow speed. This is more commonly expressed as

$$U_D = \alpha U_\infty \tag{3.3}$$

where α is an induction factor. [Note: the term 'induction factor' is also used in the literature for a, where $\alpha = (1 - a)$. Thus α represents the proportion of inflow velocity remaining at the disc plane, while a represents the reduction in velocity from

inflow to disc plane. In this work, however, α will be used for preference.]

The ratio of wake velocity to inflow velocity can be calculated similarly as:

$$U_W = \gamma U_\infty \tag{3.4}$$

where

$$\gamma = \frac{A_\infty}{A_W} \tag{3.5}$$

Conservation of momentum is then used to equate the force on the flow to the change in momentum of the flow through the core streamtube. Given that the surrounding bypass flow is at atmospheric pressure, this force comes entirely from the pressure difference across the actuator disc:

$$(p_D^+ - p_D^-)A_D = (U_\infty - U_W)\rho A_D U_D = (U_\infty - U_W)\rho A_D \alpha U_\infty \tag{3.6}$$

The pressure terms are removed through consideration of Bernoulli's equation along a streamline, where the core flow is split into upstream and downstream sections to evaluate the pressures upstream and downstream, excluding the disc plane where energy is removed. Assuming incompressibility and constant flow height along the core streamtube, this leads to:

$$\frac{1}{2}\rho U_\infty^2 + p_\infty = \frac{1}{2}\rho U_D^2 + p_D^+ \tag{3.7}$$

and

$$\frac{1}{2}\rho U_W^2 + p_\infty = \frac{1}{2}\rho U_D^2 + p_D^- \tag{3.8}$$

These combine to give:

$$(p_D^+ - p_D^-) = \frac{1}{2}\rho(U_\infty^2 - U_W^2) \tag{3.9}$$

Combining Equations (3.6) and (3.9) yields the result that:

$$U_W = (2\alpha - 1)U_\infty = (1 - 2a)U_\infty \tag{3.10}$$

which shows that half the core flow speed is lost upstream of the actuator disc, and half downstream. This is a key result used in much analytical theory for wind turbines.

The definition of power as the rate of work done by the flow at speed U_D passing through an actuator disc and exerting a thrust T_D allows a power coefficient, defined as:

$$C_P = \frac{P}{\frac{1}{2}\rho A_D U_\infty^3} \tag{3.11}$$

to be calculated as:

$$C_P = 4(1 - \alpha)\alpha^2 \tag{3.12}$$

Differentiation of this equation yields a maximum C_P of $\frac{16}{27}$ or 0.593 at an optimal α of $\frac{2}{3}$. This upper theoretical bound on power coefficient is known as the Betz limit, or Lanchester-Betz limit. However, this only holds true for the case of a wind turbine in unconfined atmosphere, where the pressure can be assumed to be atmospheric in the bypass flow, and to eventually return to atmospheric pressure in the wake.

3.2 Modelling of Tidal Turbines and Arrays

The one-dimensional model of flow through a wind turbine was extended by Garrett & Cummins in 2007 [46] for the case of a tidal turbine in a relatively confined tidal channel. When modelling a tidal turbine instead of a wind turbine, the original assumptions need to be revisited. The assumptions of one-dimensionality, irrotationality and no mixing across streamlines are largely unaffected by the change from wind to tidal. The incompressible assumption is in fact more justifiable in water than in air. However, the assumption of constant atmospheric pressure surrounding the core

flow, and a return to atmospheric pressure in the wake prior to any mixing taking place, is no longer adequate for the case of a confined tidal channel.

To resolve this, Garrett & Cummins assumed that the flow in a tidal channel was subject to 'rigid lid' constraints, i.e. that the cross-sectional area of the flow downstream of the turbine is equal to that upstream. This is a reasonable assumption at low Froude numbers, and allows a boundary condition of flow speed recovery downstream to replace that of pressure recovery downstream. As shown in Figure 3.2, this requires the inclusion of a 'mixing' zone downstream of the pressure equalisation point, which returns all flow to the inflow velocity (with an associated pressure drop).

The model for a single tidal turbine, as developed by Garrett & Cummins, is described below, followed by an extension by Nishino & Willden which expands the single turbine model to a partial array model.

3.2.1 Single Turbine (Garrett & Cummins)

A single device in a channel is shown in Figure 3.2, with the channel, device and bypass flow speeds (designated by U_C, U_D and U_B respectively) shown at various locations along the channel axis in terms of the device and wake induction factors, α and γ. The locations correspond to positions of interest within the channel. Position 1 is the upstream undisturbed flow, where velocity and pressure are equal across the channel, while positions 2 and 3 are immediately upstream and downstream of the turbine within the core flow, and as such witness the same flow speed. Wake expansion takes place prior to position 4 where pressure equalisation across the channel occurs, and position 5 is sufficiently far downstream that all mixing events have occurred and velocity has equalised across the channel cross-section.

The 'local' subscript L is not strictly necessary, but is introduced to denote the scale of channel flow immediately surrounding the device, as distinct from the array and tidal farm scales discussed later. It is also necessary to introduce the concept

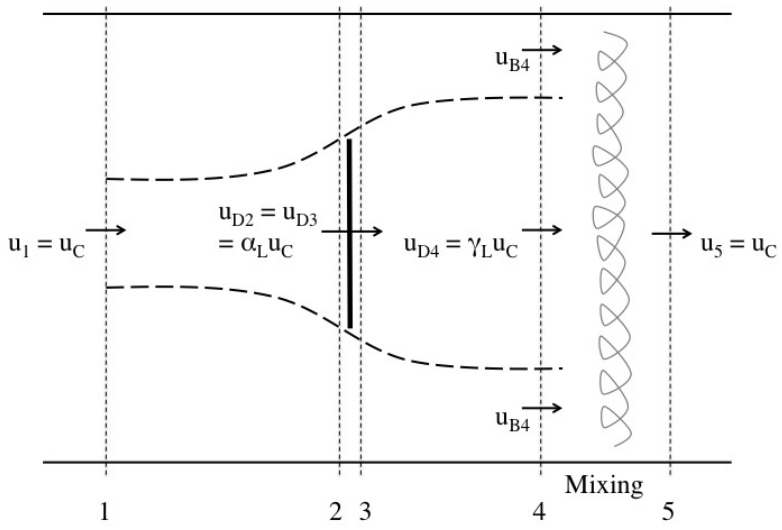

Figure 3.2: Schematic of a single device in a constrained channel.

of local blockage into the model: the proportion of the local channel cross-sectional area taken up by the device. The analytical model presented is a function of non-dimensional blockage and is not dependent on either turbine form or channel shape. However, circular axial flow turbines and rectangular section channels are used to exemplify array configurations for ease of understanding. The definition of local blockage, B_L, for such a turbine in a channel is:

$$B_L = \frac{\pi d^2/4}{hw} \tag{3.13}$$

where d is the turbine diameter, and h and w are the channel height and local channel width respectively. Note that $0 \leq B \leq 1$ for all types of blockage, since it denotes a percentage blockage of the surrounding channel. In particular, for the case of the blockage ratio of a circular turbine within its local channel, this local blockage ratio can never exceed the area ratio of a circle in a square, i.e. 0.785.

The upstream flow speed is now denoted by U_C, the undisturbed channel flow speed, instead of the U_∞ traditionally used for freestream flow. The flow speed ratios

α_L and γ_L are defined as α and γ previously. As the bypass flow speed also changes along the channel length due to the constriction imposed by the channel, a new speed ratio is introduced:

$$U_{B4} = \beta_L U_C \tag{3.14}$$

where, through geometric relationships, β_L can be expressed as a function of α_L and γ_L:

$$\beta_L = \left(\frac{1 - \alpha_L B_L}{1 - \frac{\alpha_L}{\gamma_L} B_L}\right) U_C \tag{3.15}$$

As for the unconfined model, equations of conservation of mass and momentum are set up, but with the total force on the flow through the disc including a force from the pressure difference $p_1 - p_4$. This can be resolved by invoking Bernoulli's equation along the bypass flow, which must have the same energy at position 1 as at position 4, as it does not pass through the disc and no other work is done on it. The governing equations become the geometric relations of conservation of mass:

$$A_1 U_C = A_D U_{D2} = A_{D4} U_{D4} \tag{3.16}$$

$$(A_C - A_{D4}) U_{B4} + A_{D4} U_{D4} = A_C U_C \tag{3.17}$$

conservation of momentum:

$$T_D = \rho(A_C U_C^2 - (A_C - A_{D4}) U_{B4}^2 - A_{D4} U_{D4}^2) + A_C(p_1 - p_4) \tag{3.18}$$

$$T_D = A_D(p_2 - p_3) \tag{3.19}$$

and conservation of energy, or Bernoulli's equation:

$$p_1 + \frac{1}{2}\rho U_C^2 = p_4 + \frac{1}{2}\rho U_{B4}^2 \tag{3.20}$$

$$p_1 + \frac{1}{2}\rho U_C^2 = p_2 + \frac{1}{2}\rho U_{D2}^2 \tag{3.21}$$

$$p_3 + \frac{1}{2}\rho U_{D3}^2 = p_4 + \frac{1}{2}\rho U_{D4}^2 \tag{3.22}$$

Combining these equations shows that a relationship for the local thrust coefficient exists as a function of the local channel induction factors:

$$C_{TL} = (1 - \gamma_L)\left[\frac{(1 + \gamma_L) - 2B_L\alpha_L}{(1 - (B_L/\gamma_L)\alpha_L)^2}\right] \tag{3.23}$$

which in turn are related through:

$$\alpha_L = \frac{1 + \gamma_L}{(1 + B_L) + \sqrt{(1 - B_L)^2 + B_L(1 - 1/\gamma_L)^2}} \tag{3.24}$$

The power output can be characterised in this model as

$$P_D = T_D U_D = T_D \alpha_L U_C \tag{3.25}$$

which, through the standard definition of power coefficient as given in Equation (3.1), gives

$$C_{PL} = \frac{P_D}{\frac{1}{2}\rho U_C^3 \pi d^2/4} = \alpha_L C_{TL} \tag{3.26}$$

It is therefore possible to characterise the performance of the idealised turbine in terms of both power and thrust coefficients if either the device or wake induction factor is known (or assumed). In this way the performance of the device over a wide range of induction factors can be investigated for any given blockage ratio. When considering the maximum possible power coefficient achievable, it is found that this

increases because of the blockage effect:

$$C_{Pmax} = \frac{16}{27}\frac{1}{(1 - B_L)^2} \tag{3.27}$$

i.e. the available power is multiplied by a factor of $(1 - B_L)^{-2}$, which will always be greater than 1. B_L must, however, remain relatively low for the assumptions of rigid lid flow and constant channel mass flux to remain valid, as too high a flow resistance will result in significant changes to channel flux in a real tidal channel (as discussed previously by Garrett & Cummins in [45]).

While it is possible to correct this model for the rigid lid and low Froude number assumption, as done by Whelan *et al.* [134], we continue to use the rigid lid assumption throughout this work. It is noted that relaxation of this assumption tends to increase available power through reduction of channel area downstream of turbines and hence acceleration of flow through the turbine. As such the rigid lid version is a conservative estimate of available power.

3.2.2 Partial Array (Nishino & Willden)

When considering a 'partial array', i.e. a row array of tidal turbines which does not completely span the width of a tidal channel, a revised model is required. Following Nishino & Willden [87], the single 'device' within the channel now becomes an array, within which there are n local channels which operate in exactly the same fashion as each other, as shown in Figure 3.3. In each local channel there is a turbine, and the flow through the turbine can be characterised in the same way as described above, except that the upstream flow for each turbine local flow passage now becomes U_A - the flow speed approaching the array. U_A itself is determined within an outer LMADT model for the array. The modelling scale separation assumption requires pressure equalisation and velocity recovery to occur homogeneously across all n local

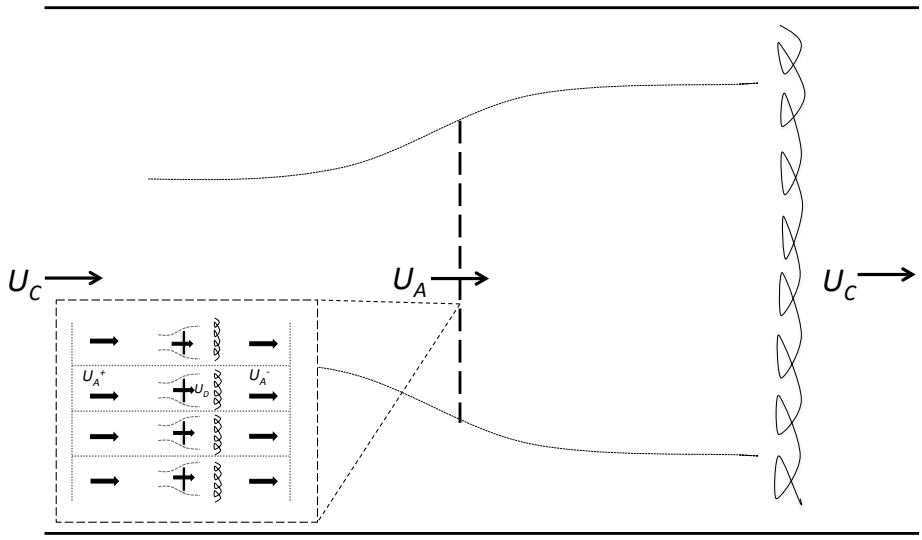

Figure 3.3: Illustration of the multiple scales of streamtubes in the partial array model.

flow passages, well upstream of the point where array scale mixing commences. Hence, the velocities at the upstream and downstream turbine passage boundaries are both equal to U_A and provide a kinematic matching point to the array scale problem.

The channel characteristics at array scale, such as induction factors, are now denoted with an A subscript to separate them from the local characteristics specific to the turbine channel.

This results in new expressions for the flow speed and induction factors within the local and array-scale channels:

$$U_D = \alpha_L U_A \tag{3.28}$$

$$U_A = \alpha_A U_C \tag{3.29}$$

Local blockage is defined as the ratio of the area of the device under consideration at each scale to the area of the local turbine channel:

$$B_L = \frac{\pi d^2/4}{h(d + s_L)} \tag{3.30}$$

and array blockage as the ratio of array width to overall channel width:

$$B_A = \frac{n(d + s_L)}{w} \tag{3.31}$$

where s_L is the local spacing between the edges of each turbine within the array. The array's 'area' is taken to be its width (n times the diameter of the turbines plus the spacing between them) times the channel height, thus giving each turbine an individual local channel of height h and width $d + s_L$.

As well as the local and array scale, a global scale is now introduced to relate directly from the devices to the full channel, to represent the turbines' performance in terms of the known upstream flow conditions. For example, the global induction factor, defining the flow speed through the device in terms of the upstream flow speed of the entire channel, becomes:

$$\alpha_G = \frac{U_D}{U_C} = \frac{U_D}{U_A}\frac{U_A}{U_C} = \alpha_L \alpha_A \tag{3.32}$$

It is then possible to consider conservation of mass, momentum and energy through each of the defined flow channels at local, array and global scale. The separate scales are related to each other through the kinematic matching of flow speeds as described above, as well as the fact that the total array thrust must equal the sum of the individual turbine thrust forces. As with Garrett & Cummins' single turbine model [46], this allows solution of the entire problem for thrust and power coefficients when the turbine's local induction factor is specified. Investigation of the maximum extractable power limit shows that it is once again found to increase, this time to a new maximum of 0.798 for an infinitely wide channel (compared to 0.593 in the original Betz limit).

3.3 Tidal farm model

There are limitations to the extensions of the partial array model that are possible in terms of modelling different physical channel situations, given the assumptions made regarding the flow within each theoretical channel. For example, a channel's bypass flow is treated as one single body of water, so that it cannot represent any asymmetrical positioning of an array within a channel, which may create pressure or flow speed imbalances within the bypass flow. This is a significant limitation on the application of analytical models to real deployments, where asymmetric positioning of turbine arrays is likely due to bathymetry or shipping channels, but within the bounds of a one-dimensional model it is not possible to allow for such cases. However, a further extension of the model is possible to represent the more realistic case of a single row of turbines divided into several smaller sub-rows. Thus, we consider an additional degree of scale separation, to allow for the situation involving a very long row of turbines within a wider channel split into m large sub-arrays, as shown in Figure 3.4. This creates an additional enveloping channel at the 'farm' level which can be subjected to LMADT analysis, much as the 'partial array' model of Nishino & Willden [87] created the outer array channel housing the inner turbine channel model.

In this problem, the flow field is considered at the local, array and farm scales. The local channel is the flow immediately surrounding each device, as in the partial array model. The array channel contains a single sub-array and half the spacing to each of the two neighbouring sub-arrays, analogously to the definition of the device channel within the array. The farm channel is then the full channel, where the entire farm of sub-arrays now partially fills the whole channel and is treated as the 'device' at this scale.

If n is sufficiently large, all device-scale flow events around the turbine will occur much faster than the array-scale events around them. This is a key assumption made by Nishino & Willden in the partial array model. If m is sufficiently large the same

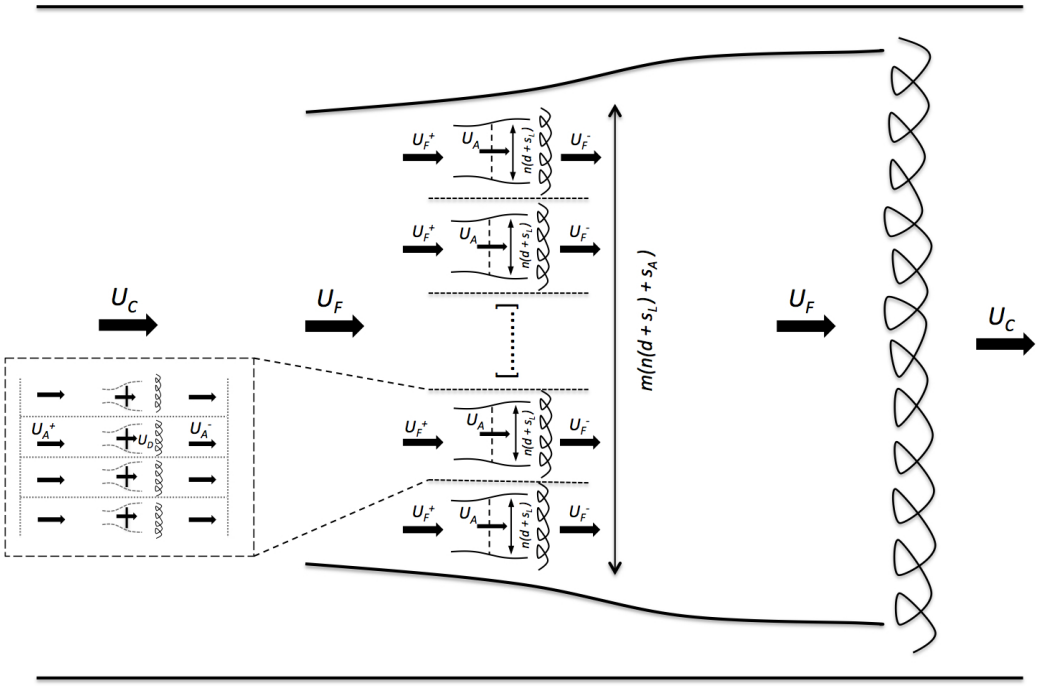

Figure 3.4: Example of a tidal farm layout with sub-arrays, showing device and sub-array channel scales. Superscripts + and - on flow speeds are included to show the recovery of the local channel speed from upstream to downstream of each scale of device.

will be true for the array scale flow events and the farm scale channel flow around them. This allows each scale of channel to be considered as a separate version of the single LMADT channel, whereby all mixing occurs before the flow equalises to that channel's inlet velocity (i.e. position 5 in Figure 3.2 for the local or array channel) and forms the device exit flow at the next channel scale (i.e. position 3 in Figure 3.2 for the array or farm scale channel), where pressure equalisation and mixing at that scale commence. Kinematic compatibility between scales is provided by the full velocity recovery within each problem scale, such that the channel scale velocity, U_C, is seen upstream and downstream of the farm scale, the farm scale velocity, U_F upstream and downstream of each sub-array, and the array scale velocity, U_A, upstream and downstream of each device. Low Froude number is assumed to ensure this, as was also done by Garrett & Cummins [46] and Nishino & Willden [87]. However, it is

noted that a free-surface correction could potentially be applied if desired, following Whelan [135] and Vogel [130]. Such a correction would be expected to increase the maximum extractable power due to downstream cross-section reduction. However, the trends of power extraction would be expected to remain the same, so the model presented is equally valid to investigate the manipulation of sub-array blockages to achieve greater power.

Induction factors are redefined at each scale as:

$$U_D = \alpha_L U_A \tag{3.33}$$

$$U_A = \alpha_A U_F \tag{3.34}$$

$$U_F = \alpha_F U_C \tag{3.35}$$

where the subscript F denotes the farm scale. The local, array and farm blockage ratios within this model are defined as

$$B_L = \frac{\pi d^2/4}{h(d + s_L)} \tag{3.36}$$

$$B_A = \frac{n(d + s_L)}{n(d + s_L) + s_A} \tag{3.37}$$

$$B_F = \frac{m(n(d + s_L) + s_A)}{w} \tag{3.38}$$

where s_A is the spacing between sub-arrays, analogous to the local spacing s_L between turbines. An alternative view of an example tidal farm, simplified for clarity, is shown in Figure 3.5 with these blockage ratios illustrated.

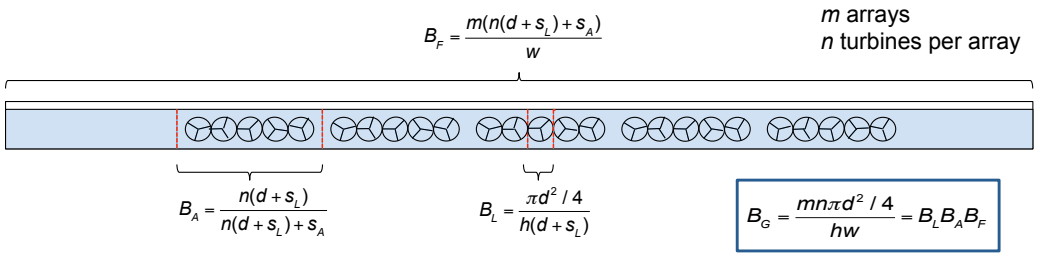

Figure 3.5: Illustration of blockage at multiple scales within sub-array model. Note: it is mathematically assumed that m and n are both significantly greater than 5, but for clarity of illustration they are displayed as such here.

It is also useful to define the global induction factor and blockage ratio, relating the turbine local fluid flow and turbine geometry to the overall channel characteristics:

$$\alpha_G = \frac{U_D}{U_C} = \frac{U_D}{U_A}\frac{U_A}{U_F}\frac{U_F}{U_C} = \alpha_L \alpha_A \alpha_F \tag{3.39}$$

$$B_G = \frac{mn\pi d^2/4}{hw} = B_L B_A B_F \tag{3.40}$$

As before, following the work of both Garrett & Cummins [46] and Nishino & Willden [87], the equations of conservation of mass, momentum and energy along the channels at each scale can be combined to obtain the array and farm thrust coefficients at each scale, as well as the relationship between the induction factors. These equations are versions of equations (3.23) and (3.24) for each of the other scales of channel:

$$C_{TA} = (1-\gamma_A)\left[\frac{(1+\gamma_A) - 2B_A\alpha_A}{(1-(B_A/\gamma_A)\alpha_A)^2}\right] \tag{3.41}$$

$$C_{TF} = (1-\gamma_F)\left[\frac{(1+\gamma_F) - 2B_F\alpha_F}{(1-(B_F/\gamma_F)\alpha_F)^2}\right] \tag{3.42}$$

$$\alpha_A = \frac{1+\gamma_A}{(1+B_A)+\sqrt{(1-B_A)^2+B_A(1-1/\gamma_A)^2}} \tag{3.43}$$

$$\alpha_F = \frac{1+\gamma_F}{(1+B_F)+\sqrt{(1-B_F)^2+B_F(1-1/\gamma_F)^2}} \tag{3.44}$$

The key relationship which allows these equations to be solved is the fact that the total thrust at all scales must be the same. This allows the thrust coefficients at each scale to be related to each other through geometry and velocity (in which q denotes the dynamic pressure):

$$C_{TL} = \frac{\text{Thrust on single device}}{\text{Local inlet } q \times \text{single device area}} = \frac{T_D}{\frac{1}{2}\rho U_A^2 \pi d^2/4} \tag{3.45}$$

$$\begin{aligned} C_{TA} &= \frac{\text{Thrust on single array}}{\text{Array inlet } q \times \text{array frontal area}} \\ &= \frac{nT_D}{\frac{1}{2}\rho U_F^2 hn(d+s_L)} = \alpha_A^2 B_L C_{TL} \end{aligned} \tag{3.46}$$

$$\begin{aligned} C_{TF} &= \frac{\text{Thrust on entire farm}}{\text{Channel inlet } q \times \text{farm frontal area}} \\ &= \frac{mnT_D}{\frac{1}{2}\rho U_C^2 hm(n(d+s_L)+s_A)} = \alpha_F^2 \alpha_A^2 B_A B_L C_{TL} \end{aligned} \tag{3.47}$$

Considering the entire channel, it is possible to define thrust and power coefficients at the global scale, which relate total thrust and power to the upstream channel inlet flow speed and total device frontal area:

$$C_{TG} = \frac{mnT_D}{\frac{1}{2}\rho U_C^2 mn\pi d^2/4} = \alpha_A^2 \alpha_F^2 C_{TL} \tag{3.48}$$

$$C_{PG} = \frac{mnT_D U_D}{\frac{1}{2}\rho U_C^3 mn\pi d^2/4} = \alpha_L \alpha_A^3 \alpha_F^3 C_{TL} \tag{3.49}$$

The above relationships (3.46) and (3.47) between the thrust coefficients form the

link between the different scales of the model. Substitution of the thrust coefficient equations at each scale, equations (3.23), (3.41) and (3.42), yields array and farm scale relationships between the axial and wake induction factors. Given that these induction factors are already related to each other through equations (3.43) and (3.44), it is therefore possible to solve the simultaneous equations for α_L and γ_L, and subsequently for α_A and γ_A, α_F and γ_F. Note that although equation (3.47) appears to create a direct link between the device-scale and farm-scale problems, the array-scale problem must still be solved because the array-scale induction factor α_A is still required in this equation, and it cannot be otherwise determined.

All of the above equations can thus be solved, either analytically or numerically, for a given value of either α_L (or equivalently γ_L), which is a function of device design and operation. For each possible combination of blockage ratios, there will be an optimal axial induction factor, relating to an unspecified optimal design, which will result in maximum C_{PG}. This theoretical maximum may be found by considering an appropriate range of induction factors.

3.4 Results

Within the model described above, there are four independent variables which can be set to explore different scenarios: three blockage ratios and an induction factor. The model is solved numerically to obtain all power and thrust parameters of interest. This results in a large parameter space which is best understood by considering specific different scenarios as outlined below. Each of these represents a particular design case where this model would be relevant.

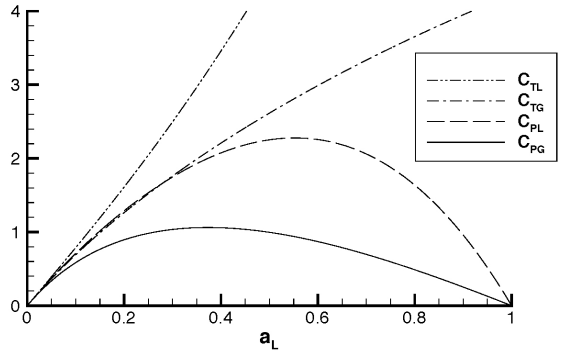

Figure 3.6: Variation of C_{TL}, C_{TG}, C_{PL} and C_{PG} with a_L ($a_L = 1 - \alpha_L$), for $B_L = 0.49$, $B_A = 0.61$, $B_F = 0.44$ and $B_G = 0.131$.

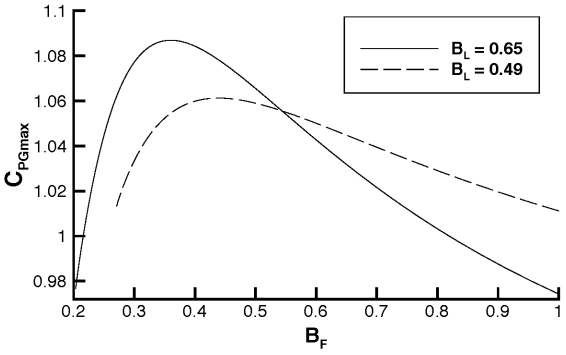

Figure 3.7: Variation of maximum C_{PG} against B_F, for fixed $B_G = 0.131$, showing cases of fixed $B_L = 0.65$ and $B_L = 0.49$.

3.4.1 Fixed Array

The simplest case to consider is that of an array where the geometry of the array layout and the basic turbine design have already been developed, such that all blockages are fixed. The only variable remaining is the turbine induction factor, representing the ability to tune turbine performance in such a case (assuming that all turbines are tuned to the same induction factor). It is therefore possible to plot the maximum power coefficient that such an array can achieve against the local turbine induction factor.

This relationship, together with those for C_{PL}, C_{TL} and C_{TG} is shown in Figure 3.6 for a case where $B_L = 0.49$, $B_A = 0.61$, $B_F = 0.44$ and thus $B_G = 0.131$. This is a specific value of global blockage considered by Nishino & Willden [87], and the results are therefore plotted against a_L instead of α_L to enable comparison with this work. For this selection of blockage ratios, it can be seen that C_{PL} peaks at a higher value of a_L than C_{PG}. This is due to the fact that at higher a_L, i.e. greater flow resistance through the turbines, C_{TL} increases significantly. This decreases flow speeds through the turbines and so reduces the total power coefficient based on global channel flow speed, C_{PG}. This is similar to previous results by Nishino & Willden [87] for a partial

array.

3.4.2 Fixed Global Blockage

Another realistic scenario for tidal array development is that of an array where site selection has been completed, and investment has been secured, effectively prescribing the number and size of the turbines. With this knowledge of total turbine frontal area and channel cross-sectional area, the global blockage ratio is fixed. However, local, array and farm blockages can still be varied based on the final design of the turbines, their support structures and the overall proportion of the channel to be used. We again consider the specific case of $B_G = 0.131$, which could equate to a tidal farm of ten arrays of ten 20 m diameter turbines in an 8 km wide channel with 30 m depth.

In Nishino and Willden's partial fence model, at this level of global blockage, it was found numerically that maximum power was available when $B_L = 0.49$. This can be replicated within the farm model as the case where $B_A = 1$ and all arrays are joined end-to-end to create one single partial array. Doing so produces identical results to the [87] model at this value of local blockage. Retaining the same local blockage, but moving the arrays apart to increase farm blockage (and decrease array blockage), produces an increase in the maximum global power available, as can be seen in Figure 3.7.

Also shown in Figure 3.7 is a similar power curve for the case of $B_L = 0.65$, which at this global blockage corresponds to the maximum C_{PG} available within the farm model. (See later discussion of Figure 3.8.) This local blockage ratio would represent an 'over-blocked' scenario in the partial array model (where $B_A = 1$, so $B_F = 0.2015$). This can be seen from the fact that the maximum C_{PG} available at this lower bound is significantly below that at the lower bound of the $B_L = 0.49$ case that resulted from the partial fence model (here, $B_A = 1$ corresponds to $B_F = 0.2673$). This is due to the fact that, in a continuous partial fence with a local blockage of 0.65, the increased

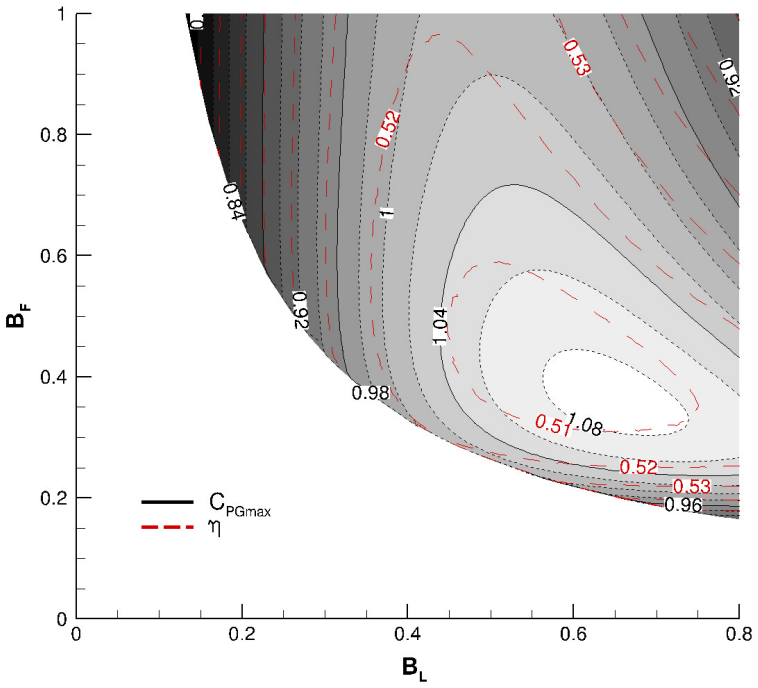

Figure 3.8: Contours (in greyscale) of maximum C_{PG} for a range of B_F and B_L, for fixed B_G of 0.131. Dashed red contours overlaid show corresponding basin efficiency η.

resistance of the array blocks the flow and reduces power output. It can be seen that moving the sub-arrays apart and allowing internal bypasses between sub-arrays quickly increases the power output and allows the farm to achieve greater power than was possible with a continuous array, for both the $B_L = 0.49$ and $B_L = 0.65$ cases. Note that the scenario of fixed B_L and B_G is one of a fixed device design and a fixed number of devices available for deployment in a known channel and therefore represents a realistic scenario in which the design variables are the spacing between sub-arrays and the tuning of the turbines (determining B_F and α_L).

If local blockage is allowed to take any value, the surface of maximum achievable power coefficient at all possible B_L, B_A and B_F is shown in Figure 3.8. Each point in this plot represents the maximum C_{PG} at a specific blockage combination for any α_L, i.e. the peak value of the Figure 3.6 equivalent at every point. While B_A is not shown

explicitly in this plot, it is determined at each point because it is inversely related to B_L and B_F, as they are related through Equation (3.40) and B_G is constant. The curved lower boundary shows where $B_A = 1$, i.e. along this line the sub-arrays meet with no array bypass flow between them and the model reduces to the single partial array model of Nishino & Willden [87] .

It can be seen that for the given global blockage of 0.131 it is possible to increase C_{PG} from the partial array model maximum of 1.011 to a new maximum of 1.087, i.e. a 7.5% increase. The increase in maximum C_{PG} when sub-arrays are allowed is achieved by increasing the local blockage ratio from 0.49 to 0.65 and spacing out sub-arrays such that the farm spreads from occupying 27% of the overall channel width to occupying 36% of it. If such a high local blockage is not achievable, however, it should be noted that even with the local blockage optimised for the Nishino & Willden [87] partial array model at 0.49, it is still possible to increase C_{PG} by 5% as shown in Figure 3.7 merely by breaking the continuous fence into sub-arrays, decreasing B_A and increasing B_F so that the farm covers 44% of the channel (up from 27%). This corresponds to moving vertically up the plot from the $B_A = 1$ lower boundary at $B_L = 0.49$. At low values of B_L, there is very little variation in C_{PG}, but where higher local blockage is possible then the use of sub-arrays can achieve significant gains in extractable power.

It is clear when considering the form of the C_{PG} plots and their maxima at any level of global blockage that there is a hierarchy of which blockage is most important for power output. The point of maximum power for $B_G = 0.131$ occurs at $B_L = 0.65$, $B_A = 0.56$ and $B_F = 0.36$. This pattern of $B_L > B_A > B_F$ at C_{PGmax} is repeated at all global blockages considered. This shows that high local blockage is the most important to increase power output, supported by lower surrounding blockages at the array and farm scales.

3.4.2.1 Basin Efficiency

While C_{PG} is an important measure of the potential power extraction that a tidal farm can achieve in a given location, it may also be important to consider the basin efficiency η, which is the ratio of power extracted by the turbines to total energy removed from the flow due to their presence. Within this model, the basin efficiency is related to the global induction factor, a_G, by:

$$\eta = \frac{\text{power extracted}}{\text{power removed}} = \frac{mnP_D}{mnT_D U_C} = \frac{U_D}{U_C} = \alpha_G = (1 - a_G) \tag{3.50}$$

The basin efficiency achieved at the point of maximum C_{PG} is also shown in Figure 3.8 as a function of B_L and B_F. The contours of basin efficiency show that, in general, basin efficiency decreases as extractable power is increased. Since power and thrust are directly related through channel flow speed in this model, increasing thrust increases power extraction, which contributes to low basin efficiency by increasing the difference between core and bypass flow speeds at each scale. Increased flow speed differentials lead to increased shear between the bypass and core flows, causing greater energy dissipation at the boundary and thus reducing basin efficiency as this energy is lost from the flow. However, it should be noted that the lowest values of η do not completely correspond with the highest values of C_{PG}, and so it would be possible to achieve a compromise situation with a relatively high power coefficient which would avoid the worst energy losses for the channel as a whole. This could be important where channels are likely to contain more than one tidal turbine farm along their length, to ensure there is as much energy as possible remaining in the flow after it passes the upstream farm. It is also important where environmental concerns are significant, and changes in the flow environment need to be minimised. It can be seen that it is possible to increase farm output power without reducing basin efficiency: for example, following the $\eta = 0.52$ contour to the right from the curved $B_A = 1$

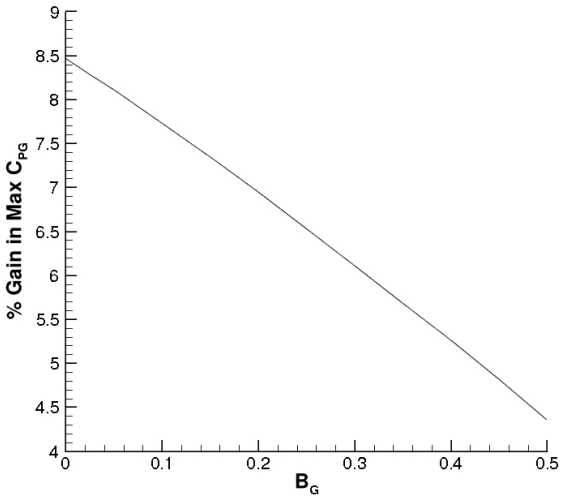

Figure 3.9: Potential % gain in maximum C_{PG} possible in moving from partial array model to farm model, for a range of B_G.

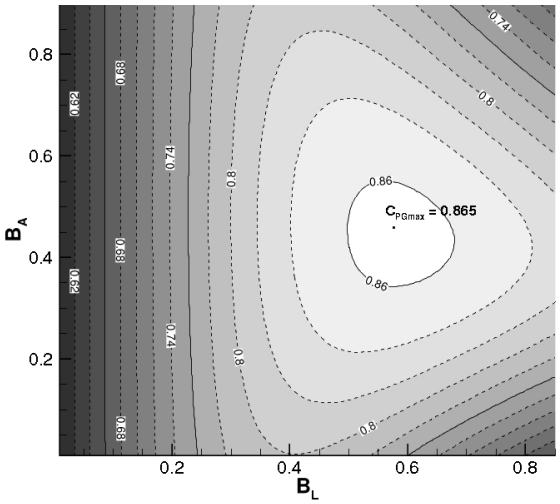

Figure 3.10: Contours of maximum C_{PG} for an infinitely wide channel ($B_F = B_G = 0$).

boundary tracks up the contours of C_{PG} while retaining the same basin efficiency. In doing so, B_F, i.e. total width of fence, remains approximately constant. This physically corresponds to taking a partial array and splitting it into sub-arrays by increasing B_L, i.e. bunching turbines more closely together to open up bypass flows between sub-arrays.

Note that the basin efficiency at maximum C_{PG}, $\eta = 0.51$ (i.e. $a_G = 0.49$), falls far below that anticipated by unblocked Lanchester-Betz type theory, for which $\eta = 2/3$ ($a_G = 1/3$) at the point of maximum power extraction.

3.4.3 Effect of Global Blockage

Figure 3.9 shows an exploration of the potential of this tidal farm arrangement of turbines for varying levels of global blockage within a channel. It starts from the position of the partial array model, and shows the percentage increase in maximum possible C_{PG} when moving to the farm model, i.e. splitting up the long array to form sub-arrays. This potential increase in available power is shown over a range of global blockage from 0 to 0.5, assuming all other blockages are free to take any value in order

to achieve C_{PGmax}. It can be seen that the potential to exploit the tidal farm model and gain increased available power by creating a sub-array structure is highest at low global blockages. (It should be noted that the percentage gain in available power continues to decrease within the model at values of $B_G > 0.5$. However, geometric constraints mean that it is unlikely that this value of global blockage will ever ever be exceeded in a real channel.) However, at low global blockage it can be seen that there is significant potential to increase power output merely through the creation of sub-arrays, possibly in the order of 5-8%.

3.4.4 Infinite Width Channel

It is finally of interest to consider the case of an infinitely wide channel, where $w \to \infty$ and $B_G \to 0$ (as $B_F \to 0$), and the far field effects of the tidal farm become negligible. For tidal turbines, which exist in a constrained medium, this case is analogous to the wind turbine in free atmosphere, where the Lanchester-Betz limit of 0.593 is the maximum power coefficient achievable. For the partial array model, Nishino & Willden found a limiting maximum power coefficient for the infinite channel width case of 0.798, where the local blockage contributed to the increase in extractable power. Both of these cases can be seen within the parameter space shown in Figure 3.10. The Betz limit is seen at the graph's origin, where $B_L = B_A = 0$, and the partial array limit occurs where the highest value of C_{PG} is found along the $B_A = 0$ axis.

Allowing both B_L and B_A to vary in the tidal farm model, the limiting value of C_{PGmax} as $B_F \to 0$ is found to be 0.865 at $B_L = 0.576$ and $B_A = 0.459$. This is a more than 8% increase over the partial array case. As was the case at non-zero global blockage, this is achieved at a higher local blockage than that of the partial array C_{PGmax}.

3.5 Discussion

The results presented in this chapter show that there is potential to optimise tidal turbine power yield through the careful choice of turbine and array spacing. The above analysis assumes that actuator discs are perfect energy extractors and as such it is not expected that the theoretical power maxima presented above could actually be reached by a real turbine farm. Further, the assumptions in the model require arrays and channels much larger than are currently under consideration for any commerical tidal power installation. In particular, the assumption that all wake mixing events at each scale take place within that scale well prior to initiation of wake mixing at the wider scales results in a very long overall channel length required to permit this assumption, potentially longer than most channels in which such a large tidal farm could be placed. The computational work of [88] to validate the partial array model showed that, although maximum theoretical values of C_{PG} as predicted by their partial fence model were not achieved in the computational simulation, the shape of the performance curves generally agreed and showed maxima at similar points. The computational results were also much closer to the partial array model predictions than to the simple single device model of [46], showing that the theoretical device-channel scale separation did reflect a dominant part of the flow behaviour. It is therefore thought likely that in the new farm model, when introducing an additional such layer of scale separation, the predicted gains in available power in moving from a continuous array to multiple sub-arrays are also real and achievable, even if viscous effects render those gains less than the analytical model might suggest.

This model does not consider many physical constraints which will affect the ability of a real tidal farm to achieve the blockages and power outputs predicted. The densest possible packing of circular, horizontal axis turbines within a channel the same depth as the turbine diameter is 0.785, which is not much greater than the optimal local blockages suggested by this model (0.65 for $B_G = 0.131$), and in practice would

be very difficult to achieve given bathymetry constraints and the natural change of channel depth over the tidal cycle. (As an example, the estimated variation between highest and lowest tides at EMEC's Fall of Warness test site is 3.5 m, with total water depth at lowest tide from 13 m at the shallowest test position to 49 m at the deepest [70]. This would significantly affect the maximum blockage that could be achieved at high water when devices must avoid breaking the surface at low water.) Even in the case where the local blockage remains the same, moving from one long partial array style row of turbines to multiple sub-arrays as posited here might invoke losses due to array end effects on each of the sub-arrays. It should also be noted that increasing thrust to the level required to extract maximum power may reduce the flow rate through a channel, but this is dependent on each channel's characteristics: geometry, bed friction, and tidal forcing. Any consideration of flow rate reduction must therefore be undertaken on a site-specific basis for any given installation, as the impact will vary between sites.

It is suggested that most real tidal turbine installations will set their approximate global blockage relatively early in the design process, once a site has been identified and a total number of turbines (and their size) has been proposed. It is clear that the greatest potential for gains from creating sub-arrays comes in channels where there is reasonably low global blockage, although given the quasi-inviscid and scale assumptions within the model, these gains may not apply to small arrays in narrow channels. However, for larger installations in wide channels (but maintaining low global blockage), local, array, and farm blockages will be determined following the selection of a site, based on device design and bathymetry constraints (B_L), support or sub-array design (B_A), and wider channel usage allowing for shipping lanes and other marine use (B_F). At this stage of development, the model shows that there is potential to improve power yield by considering blockage at all these scales before the tidal farm layout is fixed.

3.6 Conclusions

A new theoretical model has been proposed to investigate the efficiency of a long cross-stream tidal farm partially blocking a wide channel in depth-constrained flow, where the tidal farm is comprised of multiple sub-array fences in a single plane. This model creates three scales of fluid flow around the device, the sub-array and the tidal farm, in a manner similar to the two-scale 'partial array' model of Nishino & Willden [87].

The power that can be extracted from the flow is found to be maximised by careful selection of local, array and farm blockages, where high local blockage is found to be the most influential for increased power. The new model shows an increase in extractable power compared to the single fence 'partial array' model of up to 8% at low global blockage. In the case of an infinitely wide channel, this increases the maximum power coefficient achievable from the Lanchester-Betz limit of 0.593 in unconstrained flow, past the Nishino & Willden partial fence maximum of 0.798, to a new theoretical maximum of 0.865.

This model provides a theoretical framework of a new mechanism to potentially increase tidal farm power. Further physical investigation would be required to establish the practicalities of implementing this in a real tidal farm, as real bathymetry and turbine dimensions will affect whether an arrangement of sub-array turbine rows such as this could actually be constructed. Each row array may also suffer from end losses due to being shorter than the quasi-infinite length assumption made here.

Chapter 4

Scoping Exercise for Partial Array Experiments

As discussed in Sections 2.2.2 and 3.2.2, the analytical model of Nishino & Willden [87] predicts improvements in available power when a row array of turbines is arranged to take advantage of blockage effects. Computational modelling was carried out by Nishino & Willden which partially validated this model [88], however no experimental modelling of such a row array has previously been completed. Previous experimental work by Myers *et al.* [85] studied the behaviour of two porous discs next to each other, and found an increase in thrust as the discs were moved closer together. This is expected given the trends of increasing thrust with increasing local blockage in the Nishino & Willden partial array model. Stallard *et al.* [113] studied the wakes of three scale rotors arranged in a short row. Although they did not report thrust or power variation for varying inter-rotor spacing, they did identify that the rotor wakes merged to form a single array wake when the rotors were placed more closely together. This may be related to the assumptions of scale separation within the Nishino & Willden model, showing an overall array wake persisting much further downstream than individually distinct rotor wakes for closely spaced devices.

Given the lack of experimental data on row arrays, a series of experiments were planned to compare directly to the analytical model. Porous discs were chosen to represent tidal turbines, being simple to set up and not requiring careful torque or power control as scale rotors do. As discussed (in Section 2.1.1.1), porous discs are not perfect emulators of tidal turbines since they are irrotational and do not impart rotation or swirl to the flow. They do, however, offer a simple method of studying the interactions between device thrust, position, grouping etc and the resulting fluid behaviour. As such, they have previously been used to investigate the potential for tidal turbine interaction (e.g. Myers *et al.* [86] [85]).

The experiments were designed to be carried out on row arrays of porous discs in the 5 m wide recirculating flume at the University of Manchester, simulating a turbine fence array partially filling a tidal channel. The experiments targeted a parametric area where beneficial effects of close inter-disc spacing were expected, from the predictions of partial fence theory. Specific spacings and disc porosities were targeted to optimise the parametric investigation.

Initially, a short scoping experiment using two arrays of five porous discs was carried out over a two-week period in April 2014. The set-up and outcomes of this scoping exercise are discussed in this chapter. Following this, additional experimental equipment and methods were developed to design and test multiple arrays of eight porous discs across the parameter space of interest in two further experimental runs, as will be described in Chapter 5. The results of these eight-disc experiments are then discussed in Chapter 6.

A small suite of measurements were defined, which could reasonably be gathered within the two-week window available for this exercise: thrust measurements which could be gathered using strain gauges fitted to the towers, and a limited number of wake flowspeed measurements available from a single Acoustic Doppler Velocimetry (ADV) probe fitted to a moving traverser. All data were collected using LabView

routines already developed on the computer measuring setup. An array of five discs was chosen as this was the maximum number of support towers available at the University of Manchester, thus removing the need to manufacture additional equipment. Where measurement techniques remained the same between the scoping exercise and the later full experiments, they will be further described in Chapter 5, which details the set-up for the full suite of experiments.

The aims of the scoping experiment were twofold: (i) to investigate whether the increased thrust expected from partial array theory at close spacings was detectable on a short array in a scale flume at moderate Reynolds numbers; and (ii) to gain initial insight into the wake behaviour behind the array which could provide validation or interrogation of the basic assumptions of fluid flow underlying partial fence theory. The outcomes of this could guide the design of experiments to investigate the behaviour of partial arrays in more detail.

4.1 Equipment

The existing University of Manchester equipment used for disc mounting and positioning during the scoping exercise consisted of five individual strain-gauged towers, with discs centrally mounted slightly offset from their base. At their tops, the towers were mounted in rigid blocks which could be clamped to a gantry placed across the flume, as shown in Figure 4.1. In order to enable the downstream ADV traverser gantry, shown on the right of Figure 4.1, to move as close to the array as possible, the discs were mounted to a singly-supported gantry. This is shown in Figure 4.1, including a block of wood providing a simple support to the front edge of the gantry. This had disadvantages in terms of twist under self-weight, which was corrected with individual metal shims clamped under the top blocks to ensure verticality of the towers. As it was not possible to safely access the towers once the flume was running, it

is unknown whether any additional twist or non-verticality was caused by the thrust force exerted on the array by the flow. No obvious large deflection of the array was visible from the side of the flume, so the set-up was considered sufficient for the purposes of the scoping exercise.

The scoping exercise was carried out with the assistance of University of Manchester staff who had previously carried out experimental work using the same equipment, and set-up methods were replicated from previous work with their assistance. The general setup of the experiment was very similar to that shown in Figure 5.4 for the full set of experiments, although with five discs rather than eight. The disc array was positioned 6.6 m downstream of a porous weir at the flume inlet which dissipates large-scale turbulence. The total length of the 5 m wide flume is 12 m, although flow measurements were only taken up to 5 disc diameters (1.35 m) downstream of the

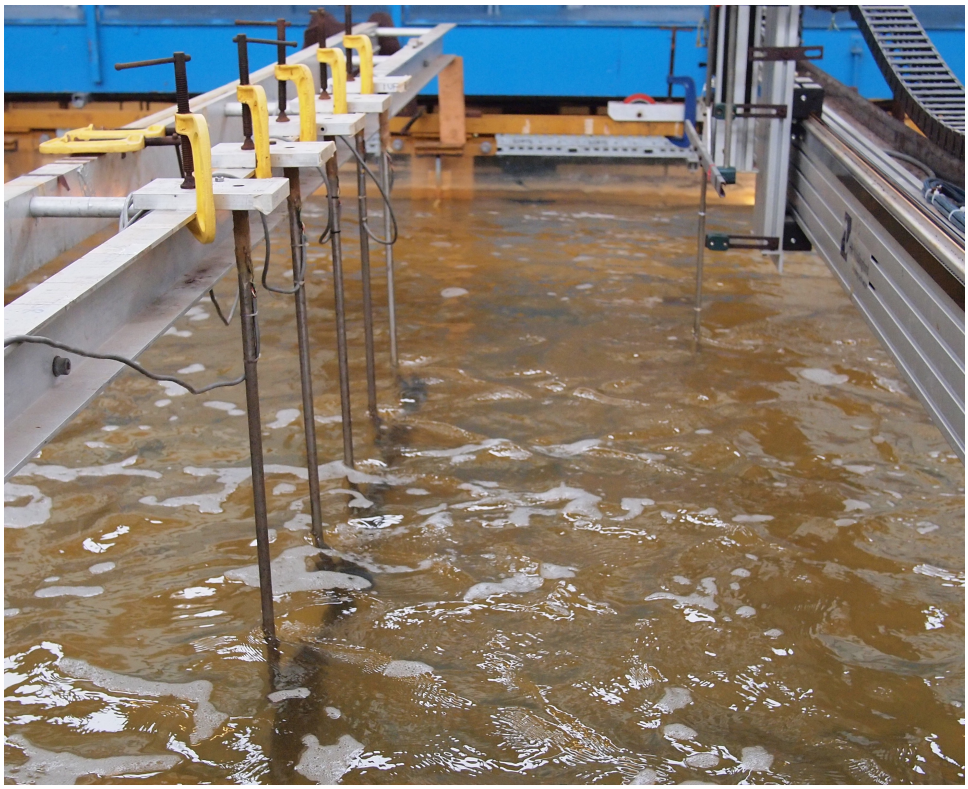

Figure 4.1: Set-up of initial scoping exercise, using equipment provided by University of Manchester. Towers are individually clamped and shimmed onto gantry.

array. The average flow speed in the working area was found to be 0.468 m/s.

4.2 Configurations

4.2.1 Disc Porosities

The polyvinyl chloride (PVC) discs used for the experimental work were 6 mm thick and 270 mm in diameter. Target porosities were achieved by machining multiple 12 mm holes in a regularly spaced pattern across the discs, except the area where the disc was mounted to the tower. The number of holes gives the porosity, or open area ratio, Θ, for the entire disc area.

Two different porosities of disc were used during the scoping exercise, with five discs of each porosity used to create the partial fence array. One porosity was chosen to be discs that the University of Manchester had already manufactured and used for other experimental work, to minimise additional manufacturing required. This set of discs had an open area ratio of $\Theta = 0.52$, created by machining 264 12 mm diameter holes symmetrically around a 270 mm diameter disc. Researchers at Manchester had previously recorded this disc porosity having a thrust coefficient of $C_T = 0.85$ when deployed individually in the flume, with C_T defined as:

$$C_T = \frac{T}{1/2\rho U_\infty^2 A_{disc}} \tag{4.1}$$

where A_{disc} is the disc area and U_∞ is the undisturbed upstream flowspeed, measured to be 0.468 m/s during the scoping exercise.

In order to compare the data to the analytical theory, it was initially assumed that the disc pressure coefficient, κ, defined in Equation (4.2), could be related to the disc open area ratio by Equation (4.3):

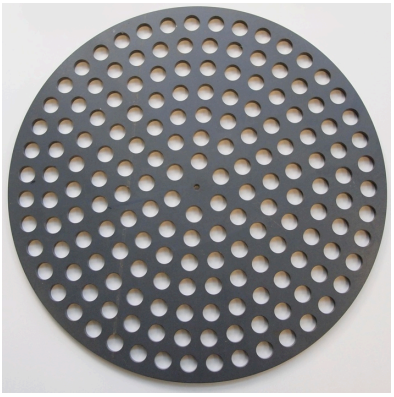

Figure 4.2: Example of $\Theta = 0.33$ porous disc as manufactured to fit Manchester support towers.

$$\Delta p = \frac{1}{2}\kappa\rho u_D^2 \tag{4.2}$$

$$\Theta^2 = \frac{1}{1+\kappa} \tag{4.3}$$

where u_D and Δp are the flow speed through and pressure drop across the disc, respectively. The second equation is an approximation of a relationship found by Taylor [119]. It is known that the actual relationship between κ and Θ may vary depending on the internal geometry of the porous disc as well as its open area, as demonstrated for example in [135], however further exploration of this relationship is not within the scope of the current work. Therefore, Taylor's relationship was taken as a first approximation to compare theoretical results, which can be expressed in terms of κ, to experimental work where only Θ is known. This assumption was later re-evaluated when experimental data on the true κ value of each disc became available, and is discussed further in Section 6.2.1.

The disc porosity of $\Theta = 0.52$ of the existing Manchester discs corresponds to a predicted disc pressure coefficient κ, as defined in Equations (4.2) and (4.3), of 2.68. This is quite a low pressure coefficient within the parameter space predicted to be of interest by the theoretical model, so an additional set of discs with lower porosity

and higher resistance was manufactured in Oxford. These discs were also of 270 mm diameter, with a central mounting point to fit onto the University of Manchester's towers, but manufactured with only 169 12 mm holes, resulting in an open area coefficient of $\Theta = 0.33$ and a predicted pressure coefficient of $\kappa = 7.97$. An example of this disc is shown in Figure 4.2. The different disc arrays will be referred to by their predicted pressure coefficient throughout this chapter.

4.2.2 Array Spacing

The aim of the scoping exercise was to examine one of the central predictions of partial fence theory, that closely-spaced arrays sustain more thrust and can thus potentially extract more power. This theory, as discussed in Chapters 2 and 3, predicts that, for a single partial array with a fixed total device area and fixed disc resistance, thrust will increase as local blockage B_L is increased. This corresponds to array blockage (B_A) reducing as the array length shortens and the array fills less of the total width of the channel.

It was therefore of interest to investigate a wide range of inter-disc spacing within the arrays, ranging from widely to closely spaced. All arrays were placed at the same lengthwise position in the flume, 6.6 m downstream of the inlet grid. Three array blockages were initially targeted as being of interest, starting from the base case of $B_A = 1$, where the discs are equally spaced across the channel to give no array blockage effect. This corresponds to an intra-array spacing, defined as the ratio of inter-disc spacing s to disc diameter d, of $s/d = 2.7$. A closest spacing was identified as $s/d = 0.1$, where the distance between the discs reduces to 2.7 cm, corresponding to an array blockage of $B_A = 0.36$. An intermediate spacing of $B_A = 0.54$, $s/d = 1$ was then chosen as a point where the array covered just over half the channel width.

For both disc porosities, arrays at these spacings were set up across the flume, and downstream measurements of wake flowspeed were taken to investigate wake be-

haviour. After these arrays were tested, an additional two intermediate array spacings were identified as desirable in order to explore the parameter space more fully and to enable the trend of behaviour to be assessed. These were the cases of $B_A = 0.405$ and $B_A = 0.675$. Unfortunately, wake measurements were not taken in these cases, but thrust measurements were recorded. An overview of the configurations tested and the wake traverses of measurements taken in each case is given in Table 4.1.

Table 4.1: Array Configurations

	Discs	
	$\kappa = 2.98$	$\kappa = 7.97$
Main Configurations (including four downstream wake measurement traverses)	$B_A = 1$, $s/d = 2.7$	
	$B_A = 0.54$, $s/d = 1$	
	$B_A = 0.36$, $s/d = 0.1$	
Additional Configurations (no wake measurement)	$B_A = 0.675$, $s/d = 1.5$	
	$B_A = 0.405$, $s/d = 0.5$	

4.3 Traverse Measurements

For each of the six main configurations (two disc porosities at three spacings), four sets of wake measurements were taken at $0.5d$, $1d$, $2d$ and $5d$ downstream. Typically 45 measurement points were taken at mid-disc height across the width of the array, with measurements taken both behind the discs and in the internal and external bypass flows. These measurements were taken using the programmable ADV traverser as described in Section 5.4. Due to the restrictions on lateral movement of the ADV traverser across the flume (given safety measures to prevent equipment contacting the edges of the flume or falling off the ends of the traverser), it was not possible to measure outside the edges of the outermost discs in the most widely spaced arrays of $B_A = 1$. No measurement of external bypass flow therefore exists for these configurations: however, as the discs are equally spaced across the flume in this case it would not be expected that the 'external' bypass flow would in fact differ from the

'internal' bypass flows in any way.

All ADV measurements were taken for 60 seconds in each position. Each configuration with downstream traverse thus accumulated approximately 180 total minutes of thrust data while the traverse measurements were being taken.

As discussed, no ADV measurements were taken downstream of the $B_A = 0.405$ and $B_A = 0.675$ configurations for either disc porosity, as these tests were included at the end to provide additional thrust data for the parameter space investigation. Thrust measurements for each of these configurations were recorded for a total of 10 minutes to ensure robustness of the mean thrust measurement.

Thrust measurements from the individual strain gauges on each tower were recorded through a National Instruments amplifier and DAQ setup, as this had been previously set up for this equipment. Other quality measures such as calibration and undisturbed flow measurements in horizontal and vertical traverses were taken, similarly to the full set of experiments as described in Chapter 5, and these were incorporated into the results. Average values of Turbulence Kinetic Energy (TKE) in the freestream were found to be of the order of 0.003 m^2/s^2, corresponding to a Turbulence Intensity (TI) of 9%.

The data collected during the scoping exercise were in the same format as those for the later experiments, and a small suite of data processing programs were created to interrogate the raw data gathered. These generated values of thrust coefficient, flow speed averages and time-varying turbulence quantities to be further analysed. These programs were later further developed, forming the model for the wider range of programs created for the full set of experiments later carried out, as discussed in Section 5.5.

4.4 Thrust Measurements

The theoretical thrust variation predicted for a partial fence array of this size in the channel width of the flume was calculated from the theoretical partial fence model described in Chapter 3. It should be noted that this calculation was done using the 2012 Nishino & Willden model [87], not their 2013 revision [88] to include short fence expansion factors, as these factors could not be measured during the experiment. Global thrust coefficient was then calculated for the arrays tested, as:

$$C_{TG} = \frac{\sum_1^5 T_{disc}}{1/2\rho U_\infty^2 (5A_{disc})} \tag{4.4}$$

These measured values of C_{TG} are plotted against the theoretically predicted values for a long fence array in Figure 4.3. A simple linear fit has been applied to the experimental values to allow the trends to be clearly seen.

It can be seen that there is a significant gap between all measured thrust coefficients and the theoretical predictions, across all configurations. This is expected as a result of the differences between the analytical case of a very long fence array and the actual case of a much shorter fence of discs. In particular, end effects can be expected to reduce the thrust on the outer discs, and with only 5 discs, these effects are likely to be felt across much of the array, leading to significant reductions in the overall global thrust coefficient. It is also likely that the separation of mixing scales assumption is less robust for shorter arrays, as the characteristic length of the array approaches the same order as the characteristic length of each individual disc. This would limit the ability of the partial fence arrangement to create higher flow speeds through the device bypass flows. An additional consideration is that the disc pressure resistance factor κ could not be experimentally measured for these discs. It is known that Taylor's relationship between open area ratio and pressure resistance factor, as

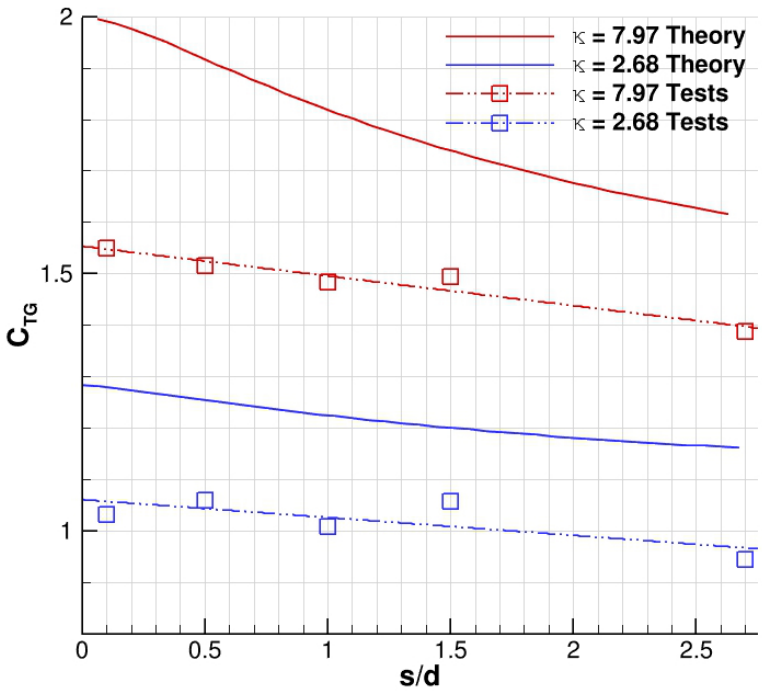

Figure 4.3: Comparison of experimental C_{TG} results with predicted theory, for discs with resistance coefficients $\kappa = 2.68$ and $\kappa = 7.97$. Experimental results have a linear fit plotted through them.

defined in (4.3), is not always reliable for all disc geometries. It is therefore possible that the κ calculated for each disc may not be correct.

However, despite these discrepancies, it can be seen that an overall trend of increased C_{TG} with increasing local blockage (i.e. decreasing s/d) exists, similar to that predicted by theory. For the case of the less resistive disc, $\kappa = 2.68$, there is a 9% increase in C_{TG} from the most widely-spaced case ($B_A = 1$, $s/d = 2.7$) to the most closely-spaced ($B_A = 0.36$, $s/d = 0.1$), from 0.94 to 1.03, which is very similar to the 10% increase from 1.16 to 1.28 predicted by the analytical model. In the case of the low porosity disc, $\kappa = 7.97$, there is a larger disparity: theory predicts a 23% increase in C_{TG} from 1.62 to 1.99, while experimental results show only a 12% increase from 1.39 to 1.55.The results for the higher resistance disc indicate that the disagreement between theory and experiment may increase with increasing thrust, causing greater flow diversion around this short length array. It might be expected

that these discrepancies would be reduced in longer fence arrays.

Generally, however, these trends of increasing thrust show that the effects of grouping together devices into partial fence arrays which are predicted by partial fence theory do indeed exist, and can be measured at an experimental scale even with a fence length as short as only five devices. This was therefore taken as justification to design an expanded experimental program of testing for a longer, 8-disc fence, as will be discussed in Chapters 5 and 6.

4.5 Flow Measurements

4.5.1 Downstream Velocity Field

Downstream flowfields were measured and analysed for the main configurations as shown in Table 4.1. This allowed insight into the flow behaviour downstream of the array, particularly relevant to assumptions made in partial fence theory, but also to inform measurement processes in the full set of experiments.

Measurements were taken at disc 'hub height' i.e. mid-depth behind all arrays, at $0.5d$, $1d$, $2d$ and $5d$ downstream of the array. The downstream flowfields for all six main configurations are shown in Figure 4.4. The lengths of velocity vectors in these plots have been scaled to avoid overlapping, and the x and y axes are not to the same scale. However, the x and y components of flow velocity are plotted in proportion to each other and as such the direction of each plotted vector is correct.

A number of things can be seen in this figure. Firstly, wake expansion immediately downstream of the array, followed by contraction further downstream, is observed as would be expected in a blocked, incompressible environment. This can be seen both at the individual disc scale (as in Figure 4.4f) and at the global array scale (as in Figure 4.4b). Secondly, it can be seen that wake mixing is not complete by $5d$ downstream, as flow speeds are not uniform and in many cases visibly not parallel.

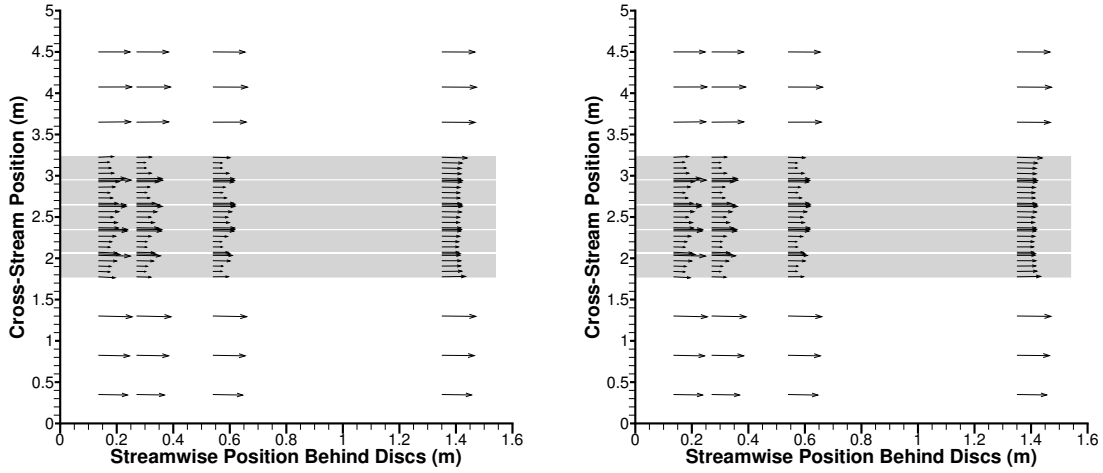

(a) $\kappa = 2.68$, $B_A = 0.36$

(b) $\kappa = 7.97$, $B_A = 0.36$

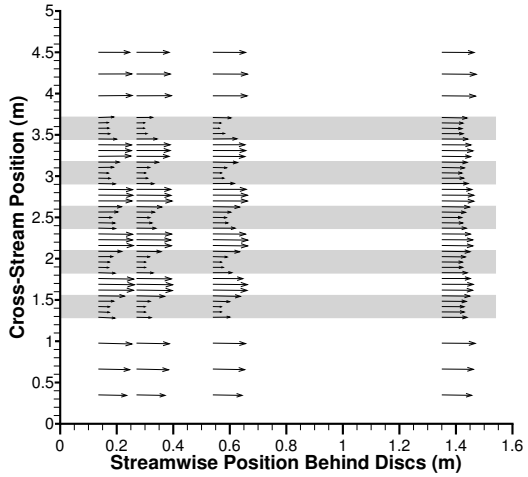

(c) $\kappa = 2.68$, $B_A = 0.54$

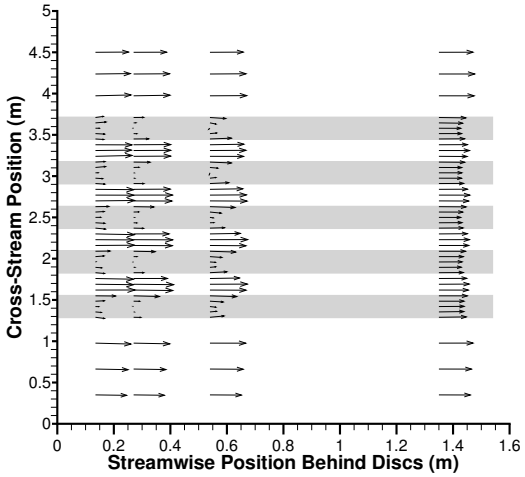

(d) $\kappa = 7.97$, $B_A = 0.54$

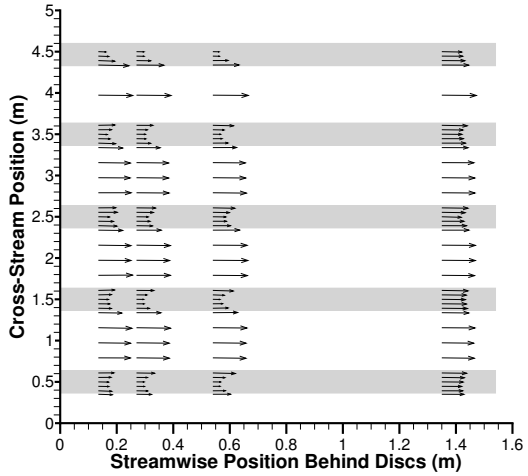

(e) $\kappa = 2.68$, $B_A = 1$

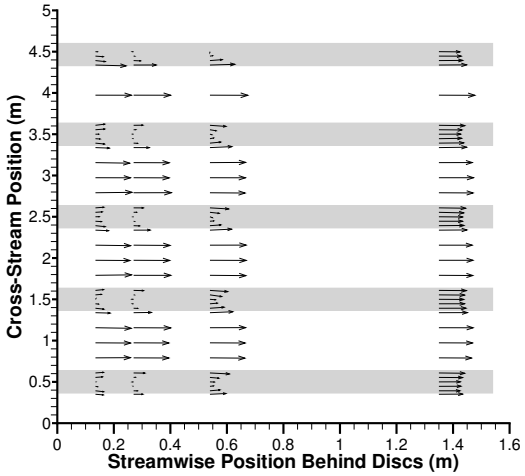

(f) $\kappa = 7.97$, $B_A = 1$

Figure 4.4: Plots of downstream flow vectors for all configurations with wake traverses. Upstream disc positions are indicated by grey bars.

This is expected, however, as the array width is $5(d + s)$ in all cases, and full wake mixing would not be expected prior to one array width downstream in any case. Given the overall restriction of the length of the flume at 12 m total, with the array placed 6.6 m downstream of the inlet, it is likely that full array wake mixing did not complete within the length of the flume.

As regards conclusions which can be drawn regarding the fluid dynamic processes which contribute to partial array behaviour, it is of interest to consider the varying levels of mixing which have occurred by $5d$ downstream for each array. The closely-spaced arrays show a nearly consistent velocity profile across the array wake itself, with velocity differences between disc flows and internal bypass flows mixing out. However, there is still a significant velocity deficit between the array wake and the external bypass flow. The more widely-spaced arrays, by contrast, still show velocity deficits downstream of the discs compared to the internal bypass flows, such that their internal array wake is less fully mixed by $5d$ downstream. This effect appears to be governed more strongly by array spacing than by disc resistance coefficient: there are few visible differences between the two disc types at $5d$ downstream for any spacing, even where the further upstream profiles differ significantly.

Regarding measurement techniques, it is clear that while there are sufficient measurements across the internal bypasses when the bypasses are reasonably narrow, such as in Figure 4.4c where a smooth profile is observable between disc core flow and bypass flow, in the wider spacings such as Figure 4.4f there is insufficient data regarding the transition from disc core flow to internal bypass flow. Similarly, there are large gaps for all arrays between the outermost measurements behind the outer discs and the next outward measurement in the external bypasses. Little information is gained by having widely spaced external bypass measurements stretching out to the edges of the flume, while information regarding the edge of the array wake is lost as no intermediate measurements were taken. This was noted as an area to be remedied in

future experiments. (It should be noted that only one measurement was taken in the internal bypass located at 4 m across the flume in the $B_A = 1$ arrays: this was due to an error in measurement processes.)

4.5.2 Measurements Away From Mid-Depth

Flow measurements taken in the internal and external flow bypasses were all at mid-depth, assuming that to be a representative mean flow speed (as later discussed in Section 5.3). Additional measurements were taken above and below mid-depth behind each disc in the closest downstream traverse at $0.5d$. There were 4 additional measurements per disc, arranged in an X-form as shown in Figure 4.5a. The intention of these additional measurement points was to gain additional data from which to calculate an overall average flow speed behind the disc, as well as potentially providing insight into mixing processes downstream of the discs. A vertical line of measurement points behind each disc was not included as it was considered likely that the influence of the upstream support towers would cause the uppermost half of these points to be unrepresentative.

Figure 4.5b shows an indicative example of the flow measurements gained at these additional points in comparison to those taken along the mid-depth line. The magnitude of each data point in this plot is scaled on the magnitude of U_x measured there. It can be seen that the additional points lying on the X-form provide some additional data, however it is difficult to draw many conclusions from this. Differences between the magnitudes of U_x from one side of a disc to the other can indicate slight misalignment of measuring points and disc position, however this can also be seen in the 5 mid-depth points measured behind each such disc as well. Differences in U_x magnitude between the top and bottom halves of each disc are no more significant than they are in the freestream, as would be expected. Otherwise, the pattern of flowspeed appears to be broadly rotationally symmetric around the discs shown

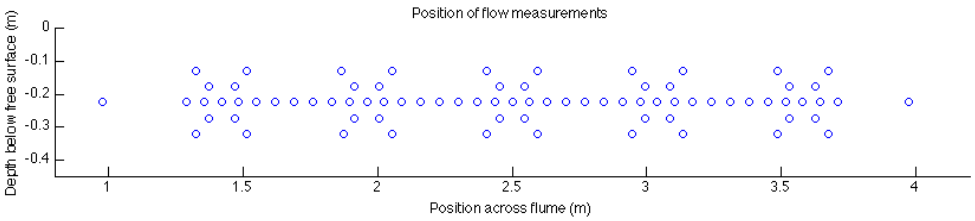

(a) Flow measurement positions at $0.5d$ behind a $B_A = 0.54$ array

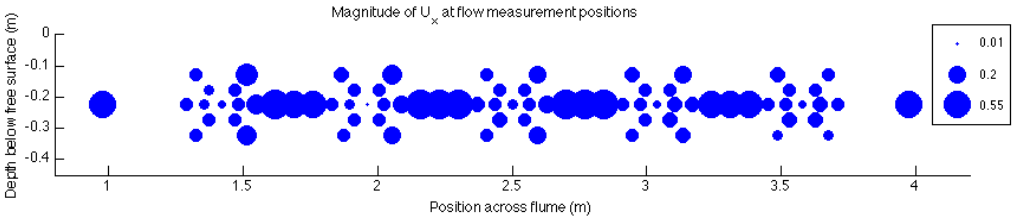

(b) U_x magnitude (m/s) at $0.5d$ behind a $\kappa = 0.797$, $B_A = 0.54$ array

Figure 4.5: Measurement points and example U_x magnitude at each point in the $0.5d$ downstream traverse for the $\kappa = 0.797$, $B_A = 0.54$ array. Note sides of flume are cropped so not all external bypass points are visible.

on the right hand side of Figure 4.5b, with the horizontal asymmetry of the other discs probably due to poor positioning of discs relative to ADV position. There is no consistent pattern across all five discs which can be extracted from this data to give worthwhile information about the flowfield away from mid-depth.

It is clear that a considerably higher density of points would be necessary to fully study the 2-dimensional variation of flow behind each disc area. Given that static porous discs do not fully emulate rotors, so that no information regarding wake swirl etc could be gained by doing this, it was decided that this would be an unnecessary use of experimental time. The purpose of this experiment was to analyse the quasi-two-dimensional interaction between device and array wake mixing in a short fence array of devices, which could be done using only mid-depth measurements. It was therefore concluded that off-mid-depth points should not be included within the further planned experimental work, as they almost doubled the measurements per disc and added no particular benefit to analysis.

4.5.3 Reynolds Stresses and TKE

It was possible to do investigate turbulence-related quantities in the array wake, in particular the Turbulence Kinetic Energy and the Reynolds stress per unit density in the x-y plane. These are defined as:

$$\tau_{xy} = -\overline{u'_x u'_y} \tag{4.5}$$

$$\text{TKE} = \frac{1}{2}(\overline{u'^2_x} + \overline{u'^2_y} + \overline{u'^2_z}) \tag{4.6}$$

where u'_x, u'_y and u'_z denote the fluctuating components of the x, y and z fluid velocities respectively, and an overbar denotes the time average. The Reynolds stress and TKE are both measures of the turbulent mixing energy present in the flow and can provide insight into the mixing processes occurring in the wake. Of particular interest is any difference between the mixing mechanisms at disc scale and at array scale, since these are crucial to the assumption of scale separation made in partial array theory.

The downstream profiles of τ_{xy} and TKE are shown in Figure 4.6 for the two closely-spaced configurations of the lower resistance disc ($\kappa = 2.68$; $B_A = 0.36$ and $B_A = 0.54$). The profiles plotted are line plots fitted to the data gathered at individual measuring points, and are therefore approximate in areas where fewer measurements were taken. (Measurement points can be seen in Figure 4.4 as the base of each flow vector.)

It is possible to observe several trends in these measurements, which support observations previously made about the flowfield, and which could also support the scale separation arguments in partial array theory. Once again, the more closely-spaced array shows more completed mixing across the array wake by $5d$ downstream, with the TKE plot (Figure 4.6a) no longer showing clear variation between disc wake

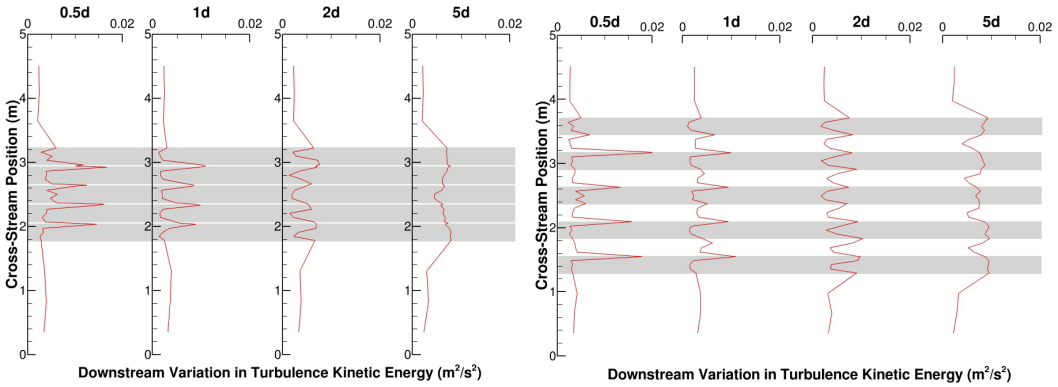

(a) $\kappa = 2.68$, $B_A = 0.36$ (b) $\kappa = 2.68$, $B_A = 0.54$

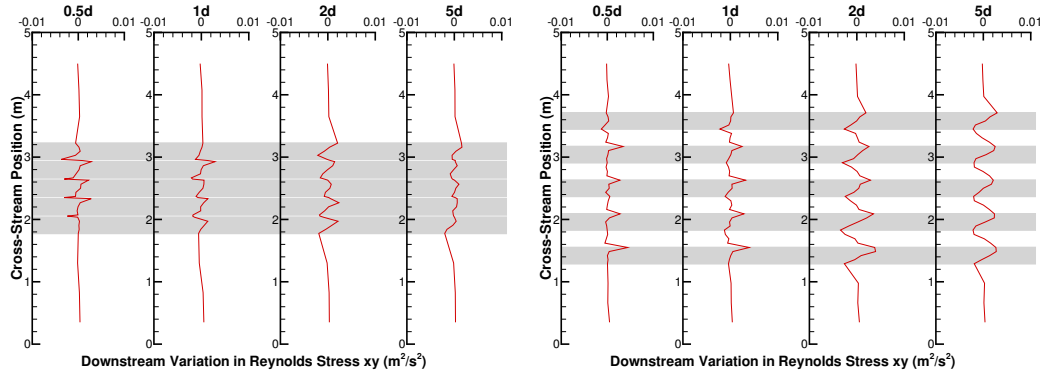

(c) $\kappa = 2.68$, $B_A = 0.36$ (d) $\kappa = 2.68$, $B_A = 0.54$

Figure 4.6: TKE and Reynolds stress τ_{xy} for two fence spacings. Upstream disc positions are indicated by grey bands.

and internal bypass flow. The τ_{xy} plot (Figure 4.6c) shows considerably less variation across each disc's wake than for the wider spacing (Figure 4.6d).

It can also be seen that some of the downstream measurement points were not as directly behind discs or within internal bypass flows as might have been desired. For example, the τ_{xy} variation in the lowest internal bypass for the closely-spaced array, shown in Figure 4.6c, is not of the same magnitude as those recorded in other bypasses in this array, even though the TKE measurement within this bypass is still recorded as being equally high. Similarly, both the TKE and τ_{xy} plots for the widely-spaced array show peaks at the lower edges of the internal bypasses, but not the upper edges, when by symmetry of the array one would expect them to be present in the shear

layers at both sides of each disc. This was considered likely due to the imprecision in setting up arrays with towers clamped individually at any point across the flume. The difficulty of positioning these perfectly within a limited time window - when the ADV positioning is absolute within the flume - could easily cause slight measurement offsets relative to the discs. This inevitably leads to some flow features being missed.

Relatedly, from these plots, one could conclude that mixing in the internal bypasses initiates more strongly immediately downstream of the array than mixing in the external bypasses. The peaks of TKE and τ_{xy} for both arrays are seen within the array wake and internal bypass flows, not within the external bypass or the shear layer between it and the array wake. This would support the assumption in partial array theory that mixing both initiates and concludes at device scale before initiating at array scale (which would potentially be around $5d$ downstream or beyond, so not visible in these measurements). This was indeed the conclusion drawn from this initial set of experiments and reported in [22].

However, care must be taken with this conclusion as a very low number of measurements were taken in the external bypass flows: only 3 measurements were taken in each external bypass, and they were equally spaced across the whole external bypass area that the ADV traverser was able to access. They are therefore very widely spaced, particularly in the case of the most closely-spaced arrays: for the $B_A = 0.36$ array, the first measurement in the external bypass is taken 425 mm beyond the last measurement in the array, or 420 mm beyond the edge of the outermost disc. For the $B_A = 0.54$ array, this reduces to 263 (or 258) mm, but it is still clear that these points are taken quite far away from the array in terms of the wake. They may therefore miss external bypass mixing processes occurring in the wake shear layer entirely if this shear layer is in fact narrow enough to occupy the space between the outside of the array and the first external bypass measuring point. This drawback to the measurement point positioning was not foreseen ahead of testing, and it was

not possible to retrospectively add additional measurement points closer to the array. Further investigation of TKE and Reynolds number in the full set of experiments, as discussed in Section 6.3.2, demonstrated that significant mixing events did indeed exist close to the edges of the arrays, which were missed in these measurements, and thus that the conclusion of complete scale separation was incorrect.

4.6 Conclusions

From the results obtained in this scoping exercise, it can be seen that the behaviour predicted by partial array theory, i.e. that more closely-spaced arrays can support higher thrust and thus therefore potentially produce additional power, can be witnessed in a small experimental set-up such as this, even with a fence array as short as five devices. Wake behaviour can also be captured which may help to explain the blockage effects and the interaction between the device and array scale fluid flow.

This study provided the impetus to plan and execute a larger set of tests on a longer array of eight discs, the results of which are described in the following chapter. However, lessons learned from this scoping exercise were invaluable in determining the scope and execution of the larger set of experiments. The key points are summarised here:

- A robust support structure was developed and designed as described in Section 5.1.1 to allow quick, repeatable movements of towers from one position to another when changing discs or altering array spacing.
- Disc and tower design was altered to allow a) mounting to new support structure and b) double-point fixing of discs to towers.
- Measurements were only taken at mid-depth in the later experiments, having established that taking a low density of points away from mid-depth added no particular understanding.

- The positioning of measurement points within the external bypasses was altered to skip the far outside flow where no mixing occurred, to focus on the flow nearer to the array and ensure that mixing events were captured.

- General positioning of measurement points behind discs and in internal bypasses was altered to improve the data capture if discs did become slightly offset, i.e. bringing points behind discs inwards to ensure that it was always certain that they were positioned in the disc wake.

- A means of measuring power extracted from the array needed to be developed, as while thrust behaviour could show increasing trends as predicted by theory, it could not identify an optimal spacing of peak performance, since only the power coefficient peaks and drops off in the over-blocked case: thrust coefficient continues to increase. This led to the investigation of 'inferred power', which will be discussed in more detail in Section 5.8.

- A greater range of disc resistances and spacings also needed to be tested to achieve any ability to identify this area of peak performance.

- Understanding of the wake behaviour immediately downstream behind the array is of more value when comparing to the assumptions of partial array theory, since it is most closely comparable to where the scale separation is assumed in the theoretical model. Therefore, traverses near to the array should be prioritised for establishing the validity of these assumptions, though with some further downstream traverses taken if possible to establish other trends of wake behaviour.

This knowledge gained from the short scoping exercise was thus used to inform not only the design of the equipment for further experiments as will be described in Chapter 5 but also the scope and detail of measurements taken and analysis performed, as will be discussed in Chapter 6.

Chapter 5

Experimental Methods to Investigate Partial Array Behaviour

Using the experience gained from the scoping experiment, a full suite of experiments using an eight-disc array was developed. New support methods were designed and implemented, and a variety of porous discs with multiple different porosities was made to allow a wider parameter space to be investigated. A method was also developed to allow investigation of power extracted from the flow, in addition to the thrust and flowspeed measurement capability. Two sets of experimental work were carried out, one in October-November 2014 and the second during April-June 2015.

This chapter describes the set-up for these experimental tests, the methodology employed in data recording and the data quality assessments made during testing. It also includes discussion of some differences in results obtained between the two sets of data, and makes a conclusion as to which results will be presented and discussed in Chapter 6.

5.1 Physical Set-Up

5.1.1 Support Structure

The experience of using the equipment for the scoping exercise described in Chapter 4 showed that, while the electrical system and data acquisition worked well, the physical set-up for each experiment was time-consuming and not always robust or repeatable. This was due to a number of factors: each support tower required individual measurements of verticality and shimming to correct for gantry twist; the single M4 screw connection between disc and tower led to significant flow-induced vibration and consequent loosening of the screws; and in order to take wake measurements closely behind the discs, a specific gantry needed to be used, which was only partially supported at each end, as shown in Figure 5.1a. This reduced the ability to control gantry twist, worsening the alignment problem. While it was possible to spend time on set-up for a single array and achieve robust, repeatable positioning, this was felt impractical for a scope involving multiple array configurations. A different, more robust, support structure which took account of these factors was designed as shown in the drawing of Figure 5.2. Figure 5.3b shows the system, with flow in operation and measurements being taken.

This new structure was compatible with the existing flume, sitting on top of a cross-flume gantry. However, the structure was also capable of being cantilevered off the back of the gantry, bringing it closer to the flow measurement equipment, and thus allowing a fully-supported gantry to be used (Figure 5.1b). The structure was fabricated from aluminium, avoiding known problems of corrosion, but was designed to be sufficiently rigid, with the towers mounted to a square box section. This mounting was achieved through M6 bolts and nuts, requiring no shimming, holding the tower attachments flush to the support structure as shown in Figure 5.3a. The support towers were regularly checked during testing, particularly after they had been

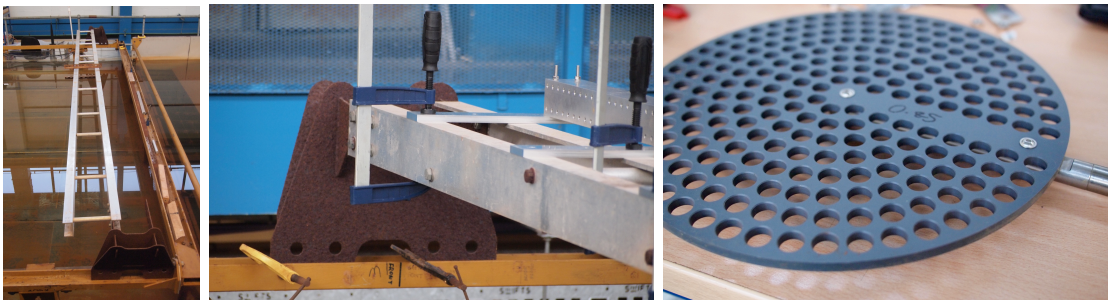

(a) Singly-supported (b) Doubly-supported (c) Disc mounting

Figure 5.1: Photographs of: a) a singly-supported gantry as was used in the scoping exercise to allow the ADV equipment to be positioned sufficiently close to the discs; b) a doubly-supported gantry as was used in the full experiment where the support structure was cantilevered off the front of the gantry; c) mounting detail between disc and tower in the full experiment.

relocated, to check their verticality. The full support structure was clamped to the gantry at every cantilever arm location to ensure a fully rigid system.

The disc support towers were manufactured from 15 mm diameter stainless steel tube, with an inner diameter of 10 mm. Flats were machined into the tube wall at the top of the tower, on which strain gauges were applied. Discs were mounted flush with the back of the tower, attached to a solid section with a machined flat surface. Each disc was fastened to this solid section through a screw at its centre and another 20 mm from the outer diameter, as shown in Figure 5.1c. This flush mounting of the disc, with two fixing points, was found to reduce high frequency flow-induced vibrations which had been observed during the scoping exercise.

Θ (Open Area Ratio)	0.25	0.3	0.35	0.4	0.45	0.5	0.6
No. of radii for holes	7	7	7	7	8	8	9
Total no. of 12 mm holes	127	152	177	203	228	252	302

Table 5.1: Porous Discs

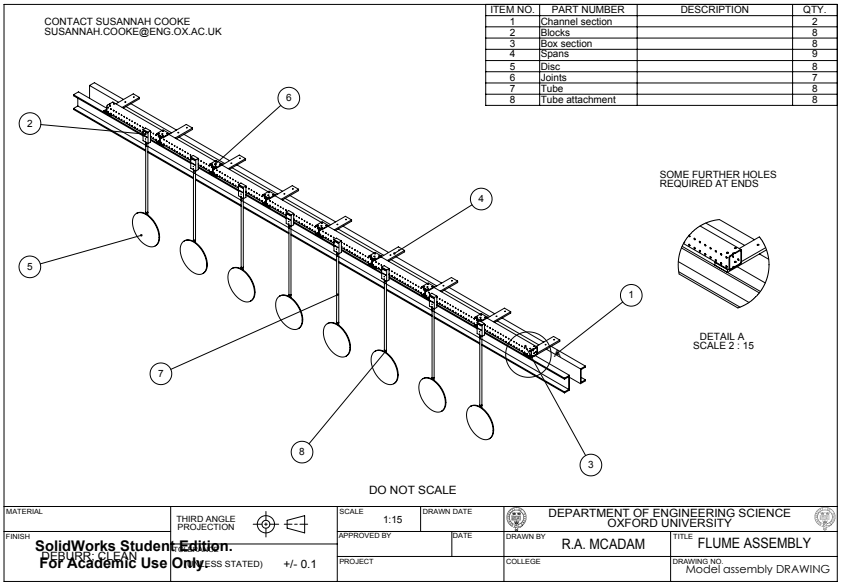

Figure 5.2: Assembly drawing of entire support structure, resting on a gantry.

(a) Single disc (b) Array of discs in position

Figure 5.3: Photographs of: a) a single disc and its support tower, seen from downstream of the array. Strain gauges are mounted under the black protective coating at the top of the tower; b) disc array seen from upstream of the array. ADV traverser equipment and probe support can be seen behind the array.

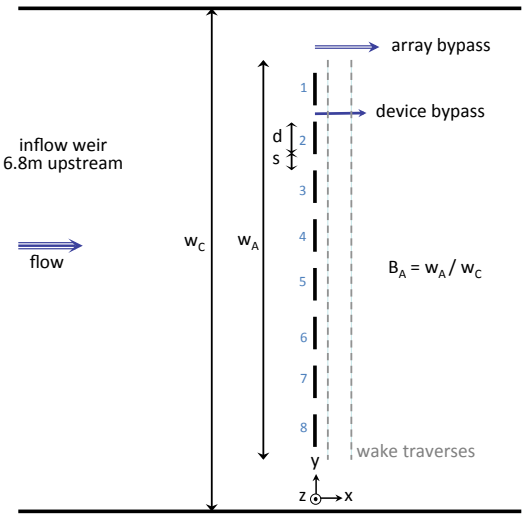

Figure 5.4: Diagram of experimental arrangement within flume, shown from above (not to scale). Flow direction is from the left. Example disc positions for an array are marked by bold black lines, and the disc numbering convention is shown.

5.1.2 Porous Discs

The PVC discs used for this experimental work were designed to be the same size as those used in the scoping experiment, 6 mm thick and 270 mm in diameter. Desired disc porosities were again achieved by machining multiple 12 mm holes in a regularly spaced pattern across the discs, except that the disc mounting arrangement was different, so a larger area had no holes in (as shown in Figure 5.1c). Eight discs were made for each of seven porosities, as detailed in Table 5.1. In order to design discs to target the area of interest in analytical theory, it was again assumed that the disc pressure coefficient, κ, defined in Equation (4.2), could be related to the disc open area ratio by Equation (4.3). This assumption will be discussed further in Section 6.2.1, given the results of measured thrust and κ values during this experiment.

The still water depth of the flume, h, was 0.45 m. The fence arrays of eight discs were positioned centrally within the flume width, at mid-depth, with equal inter-disc spacing between the discs. This inter-disc spacing, s, was varied to investigate the effect of spacing on array performance. A general arrangement is shown in Figure 5.4,

Masses, in order of use	Measured mass	Deviation from 100g
1	98.07 g	-1.93%
2	98.57 g	-1.43%
3	98.29 g	-1.71%
4	98.30 g	-1.70%
5	98.90 g	-1.10%
6	98.12 g	-1.88%
7	98.91 g	-1.09%
8	98.18 g	-1.82%
9	98.60 g	-1.40%
10	98.22 g	-1.78%

Table 5.2: The measured masses of the nominally 100 g weights used during calibration, and their percentage deviation from nominal mass.

identifying important parameters such as the disc diameter d and inter-disc spacing s, array and channel widths, w_A and w_C. Thrust on each individual disc was measured using a full bridge of linear strain gauges, mounted at the top of each support tower under a protective waterproof coating (see Figure 5.3a). Flow measurements were taken downstream of the array at mid-depth using a Nortek Vectrino$^+$ Acoustic Doppler Velocimetry (ADV) probe, aligned in the cross-stream direction. The axis origin is taken as being in the plane of the discs, at the water surface, at the right-hand edge of the flume relative to the flow, as shown in Figure 5.4. This gives a right-handed coordinate system with x positive in the streamwise direction, y positive across the flume and z positive upwards. Over the course of all testing, each array configuration had at least two downstream wake traverses of ADV measurements taken, at $0.3d$ and $1d$ downstream of the array. For a small number of arrays (i.e. those with highest or lowest total thrust) traverses further downstream were also taken. The approximate position of the $0.3d$ and $1d$ traverses is also shown in Figure 5.4.

5.2 Electrical Set-Up

At the top of each tower, two double linear EA-06-125PC-350 strain gauges produced by Vishay were mounted on flats machined into the tower to provide a full bridge of strain gauges measuring the axial strain along the tower, wired to measure bending. These strain gauges were individually connected to National Instruments SCC-SG24 'Strain Gage Input Module' amplifiers, with a gain of 100, mounted in a National Instruments SC-2345 carrier with shielding. Their output was passed to LabVIEW data acquisition software through a National Instruments analogue DAQ. The strain gauge system was calibrated multiple times during testing by clamping each tower horizontally and loading the disc central mounting point with calibration weights up to 1 kg, in 100 g increments. These weights were separately weighed to confirm their true mass, as they were designed with a $\pm 5\%$ tolerance. This mass, used for calibration calculations, is shown in Table 5.2. A tower undergoing calibration is shown in Figure 5.5a. An example of output voltage plotted against load during calibration is shown in Figure 5.5b. Table 5.3 shows the calibration factors calculated for all 8 towers across the 4 separate sets of calibration measurements taken during the second 6-week testing programme. It was not possible to directly compare with the calibration results from the first set of tests, since instrument amplifiers were exchanged between the two sets of tests.

For each array configuration, a number of initial and final measurements were taken for each test, to allow the total thrust on the discs to be isolated from the thrust on the towers: (i) strain gauge readings were taken in still water with only the towers present; (ii) in flow with only the towers present; (iii) in still water with the discs mounted to the towers. This enabled a disc-only measurement of thrust to be calculated. It should be noted therefore that only the calibration gain (load vs. output gradient) was required, as the force calculation process takes account of the no-flow condition, so no signal offset was required from the calibration.

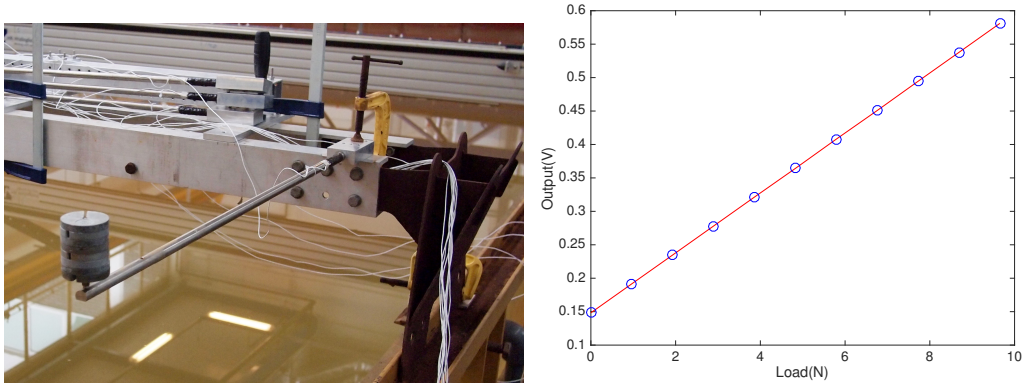

(a) Calibration set-up (b) Calibration example: Tower 2

Figure 5.5: Calibration: a) a photo showing the setup of calibration for each individual tower, clamped horizontally with calibration weights applied at the disc centre mounting point; b) an example of calibration results (for Tower 2, in Calibration 2) showing point data (blue circles) at every 100 g increased load and output voltage reported, with a least-squares linear fit applied (red line).

A relatively long period of measurement was required for each calibration point due to the difficulty of fully isolating the work area from ambient vibrations from surrounding equipment, such as other water pumps etc in the same building. Due to time constraints, calibration readings after each mass was added were restricted to 60 seconds for calibrations 1, 3 and 4. During calibration 2, however, 120 seconds was able to be allowed for each reading. It can be seen that the measurements taken in the other calibrations differ by no more than ±3%, and show no clear trends of change

Tower	Calibration 1	Calibration 2	Calibration 3	Calibration 4
	(Newtons/Volt)			
1	21.0820	20.7255	20.7670	20.9576
2	22.8386	22.3099	22.0890	21.7923
3	21.0496	20.7242	20.8071	20.8154
4	21.6458	21.2882	21.2563	21.2818
5	21.0943	20.7458	20.7873	20.8018
6	21.3813	21.0923	21.1007	21.0607
7	21.3343	20.9674	20.9108	20.9443
8	21.2497	20.8986	20.7962	20.9550

Table 5.3: Calibration factor results (gradient of load/voltage plots) from four separate calibrations during second set of tests, shown to 4 d.p.

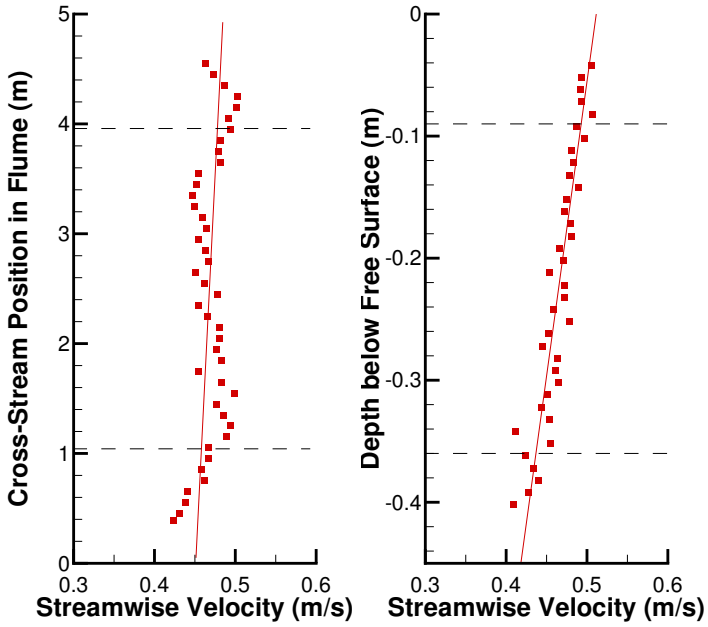

(a) Horizontal U_x profile (b) Vertical U_x profile

Figure 5.6: Freestream U_x a) horizontal and b) vertical profiles at mid-depth and mid-span, respectively, through the working area. Linear fit is included in a) to show the slight asymmetry of flow, and in b) to show the approximately linear relationship of U_x with depth. Horizontal dashed lines indicate the lateral and vertical extent of the arrays tested.

over the course of testing. Calibration 2, with the longest measurement time, was therefore taken to have the most reliable calibration factors for use in all calculations.

5.3 Flow Conditions

The mean flow speed through the working area in the x direction was found to be 0.469 m/s at mid-depth. This flow speed is created through the action of two recirculating pumps acting in parallel. A slight asymmetry was found in the undisturbed U_x flow speeds at the measurement plane, as shown in Figure 5.6a. The vertical shear profile of the undisturbed flow within the working area at the centreline of the flume (Figure 5.6b), was found to be approximately linear through the 20-80% depth in which the discs were placed. This is in agreement with the log law profile determined

previously for this flume by Olczak *et al.* [92], and allowed mid-depth measurements to be taken as mean flow speeds. Any large-scale turbulent structures created by the pumps were dissipated by an upstream grid weir, located 6.8 m upstream of the array. Average values of Turbulence Kinetic Energy (TKE) in the undisturbed freestream, with no array present, were found to be in the region of 0.003 m^2/s^2, and the Turbulence Intensity (TI) was found to be 9%.

5.4 Measurements

The vertical and cross-stream position of the ADV probe was controlled remotely through programmable traverser controls, allowing multiple measurements to be taken in one cross-stream plane without stopping the flow or manually moving the traverser. Changing the traverser's streamwise position, to capture different cross-stream planes of the flow, was achieved through manual repositioning of the gantry in stationary water. The number of points sampled in each traverse was around 70, all taken at mid-depth. For wider array spacings, some additional points were included to capture the spatial variance of the device and array bypass flows. The Nortek Vectrino$^+$ ADV probe was able to sample flowspeeds at a distance of approximately 50 mm from the probe centre, in a water volume of 6 mm diameter and 15 mm length [89].

The data presented in this chapter was taken across two sets of tests, as further discussed in Section 5.7. During initial set-up of the first tests, the ADV probe was found to be misaligned in the x-z plane, having become rotated within its housing collars. Re-alignment was not possible at the time, as it was considered likely to damage the probe and no replacement probes were available. Therefore, numerical correction of this rotation was applied to all test measurements taken, based on the average flow rotation observed in freestream measurements taken across the working area at mid-depth. The average angle by which the freestream measurements were

seen to deviate from horizontal flow was found to be 4.6 degrees. An opposite rotation of 4.6 degrees in the x-z plane was therefore subsequently applied to all experimental data taken. Prior to the second set of tests, the misalignment of the ADV probe had been mostly corrected by manual readjustment; however, the same observation and correction of flow rotation was still carried out to ensure consistency, although in this case the angle of rotation was only in the order of 1 degree and did not significantly affect the data.

Thrust and flow measurements were sampled simultaneously at 200 Hz, with every flow measurement point being sampled for 60 seconds. These parameters were based on work carried out in the same flume previously [22] [113]. Nortek, the ADV manufacturer, recommend a minimum of 30 seconds of sampling in unstable flow [89]. The ADV probe data quality (such as signal-to-noise ratio, particulate reflection count, etc) was also monitored continuously throughout testing, using Nortek's PolySync software. Since thrust measurements were recorded simultaneously with flow measurements, several hours of thrust data were accumulated during the wake traverse process for each array. Thrust figures represent an average over at least an hour for each configuration. It should be noted that the flow speed measurements from the ADV were not recorded directly from the PolySync software, due to the difficulties inherent in aligning the readings with strain gauge measurements being recorded within LabVIEW. Instead, the ADV signals were recorded by LabVIEW concurrently with strain gauge readings.

5.5 Data Processing

For every 60 second measurement window per flow point sampled, LabVIEW produced a file with 12000 (60×200 Hz) entries of 12 values: 8 for the strain gauge readings, and 4 for the flow speeds. The Vectrino$^+$ ADV gives a single reading in the

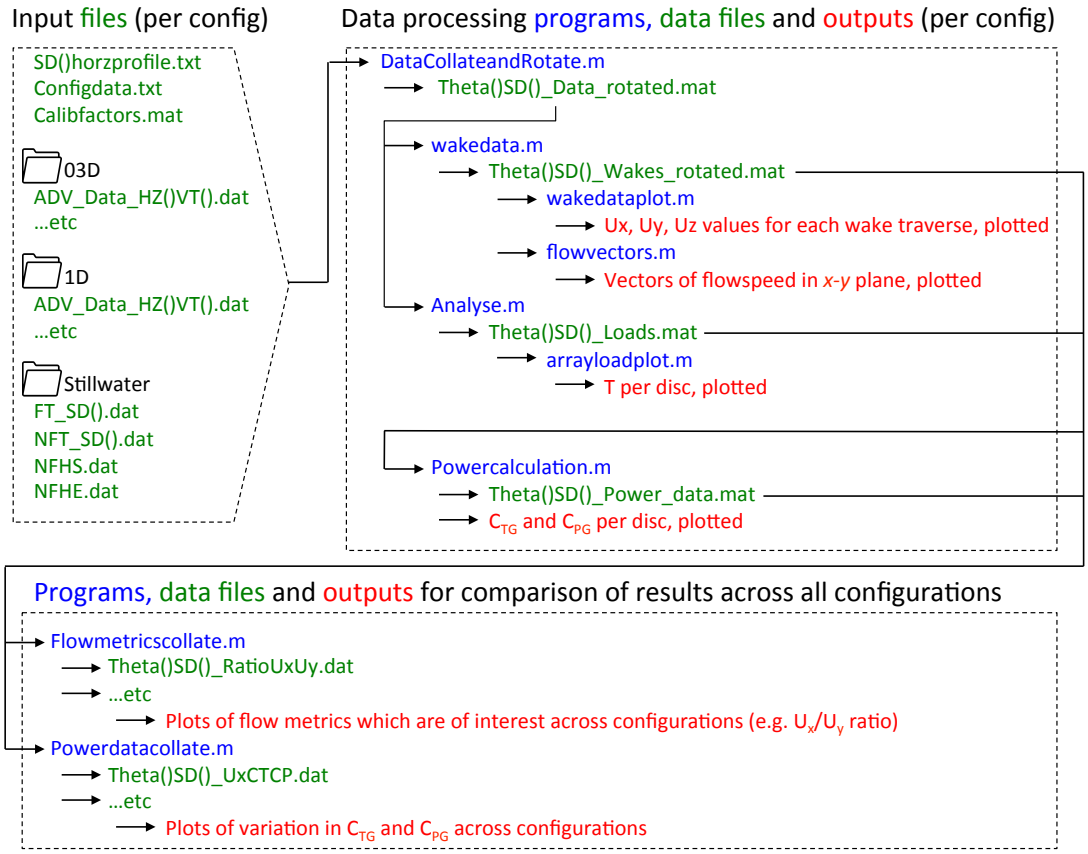

Figure 5.7: Diagram of data processing flow, from collections of LabVIEW data files for each traverse behind each configuration through to power, thrust and flow comparison graphs across all configurations.

x and z directions, but provides two measurements of the y component of flow speed. These two measurements are averaged to obtain a more robust measurement of the y velocity.

For each array configuration tested, it was necessary to collate all these 60 second measurement windows into one measurement record to allow time-averaged measurements of thrust to be calculated. Once this had been performed, it was then possible to carry out further calculations to rotate the flow as described in subsection 5.4 and align it to the global coordinate system. Further processing of strain gauge data into disc load, flow speed measurements into wake flow properties, and combining flow speed measurements with thrust measurements to provide an 'inferred power' mea-

surement were then carried out. (The concept of an 'inferred' power will be further discussed in section 6.2.2.) The full suite of data collected for each configuration, the procedures carried out on each set of data, and the Matlab programs written to achieve this, are illustrated in Figure 5.7. These programs were made to be easily applicable to all future datasets collected, allowing results to be easily calculated immediately after testing of each array, so that problems could be identified at an early stage, prior to subsequent tests.

5.6 Data Quality

5.6.1 Real-Time Flow Monitoring

Measurements of flow speed readings from the ADV and strain gauge output for all eight discs were taken simultaneously and recorded in LabVIEW. Data quality metrics for the ADV output were also monitored throughout testing using the Nortek PolySync software. This allowed standard data quality measures such as the Signal-to-Noise ratio (SNR) and auto-correlation to be observed constantly during testing so that any problems could be immediately rectified. The ADV probe also reports, through PolySync, the particulate count measured within the water. This is an important metric because the ADV technology relies on reflection of acoustic pulses from suspended particulates in the flow, and there is a minimum particulate threshold which the ADV requires.

During the first set of tests, it was observed that the data quality had reduced, with many noise spikes visible in the live ADV data, and a particulate count below 30 at times. Nortek's recommendation [89] is that the particulate count should not drop below 60 for reliable measurements. It was found that the quantity of particulates in the water had dropped due to a coagulant being added to the water during routine flume maintenance. This was rectified by using a broom to disperse settled particulate

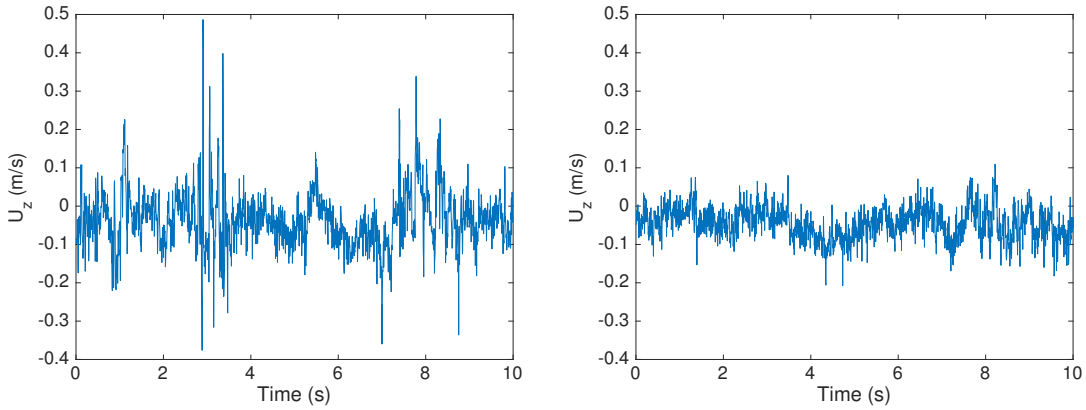

(a) Particulate count ≈ 30

(b) Particulate count ≈ 80

Figure 5.8: 10s of U_z measurements taken at the outermost bypass position, a) before and b) after the problem of a low particulate count was identified and rectified.

matter into circulation, returning the particulate count to around 80, and reducing noise in the signal. A visual example of this is shown in Figures 5.8a and 5.8b, comparing 10 seconds of raw U_z data at a point in the bypass flow, before and after the low particulate count was discovered and rectified. It can be seen that, while there is large-scale turbulent fluctuation visible in both sets of measurements, the first set (with a particulate count around 30) has considerably more high-magnitude noise than the second set (taken with particulate count readings of 80-90). Note that although U_z is displayed here, all velocities showed similar spikes: U_z is shown because it consists of a single ADV measurement, unlike U_y, and it has a low average velocity in this bypass position, unlike U_x, making the effect of measurement noise more clearly visible.

This problem was discovered on the day that the particulate count dropped, since the noise spikes were visible on live PolySync data displayed while tests were running. Once discovered and rectified, care was taken throughout all testing to keep the particulate count above 60.

5.6.2 Variability Due To Flow-Driven Behaviour

Apart from the specific problem of the ADV particulate counts, the data quality of the time-averaged, nominally steady-state measurements, taken during testing was generally seen to be affected by the turbulent nature of the flow, and by flow-induced vibrations on the discs and towers. Load measurements of the towers in flow, without discs, are shown in Figure 5.9. This clearly displays flow-induced vibrations, as might be expected from vortex shedding from the tower cylinders. Taking the Strouhal number of a long cylinder as 0.2, since the Reynolds number is around 6000, the vortex shedding frequency for a 15 mm diameter tube in flow at 0.45 m/s is calculated from:

$$St = \frac{fL}{u_\infty} \tag{5.1}$$

where St is the Strouhal number, f is the vortex shedding frequency, L is the characteristic dimension of the object in flow (in this case the tower diameter) and u_∞ is the freestream flow speed. Taking the freestream speed as 0.45 m/s, the calculated vortex shedding frequency is 6 Hz, and therefore the frequency of drag oscillation (twice that of vortex shedding) would be expected to be 12 Hz. Figure 5.9,shows the towers have a fluctuating load with a frequency of around 13 Hz, as 13 full cycles are visible within Figure 5.9a. There is also a power peak at approximately 13 Hz in the Power Spectral Density of the signal (Figure 5.9b), further discussed in Section 5.6.3. This vibration appears to be due entirely to vortex shedding from the towers.

With discs mounted to the towers, vortex shedding effects become more complex, and will exist at multiple frequencies, with characteristic lengths of the tube diameter, disc diameter and disc internal hole diameter all present. It is not possible to effectively remove all vortex shedding effects and freestream turbulence effects on the measurements taken. However, their contribution to the total signal should average

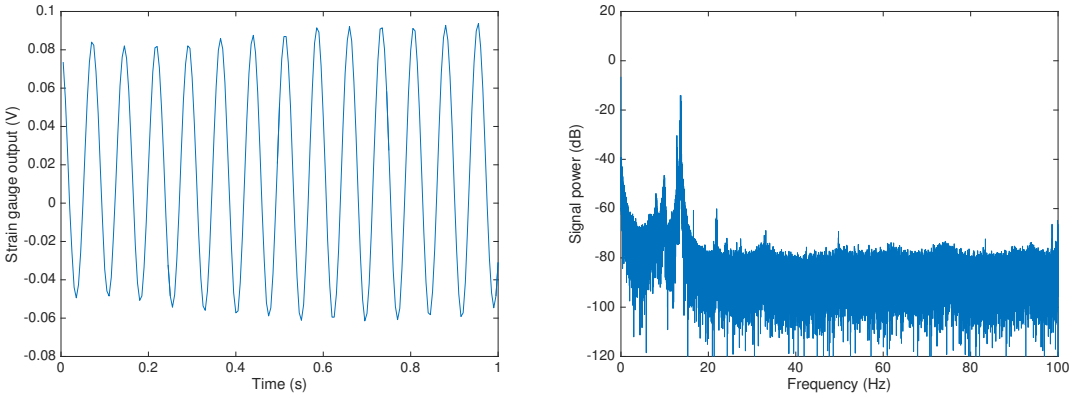

(a) Time-varying signal (b) Power Spectral Density

Figure 5.9: Raw strain gauge data from a single support tower during a baseline test with no discs attached, for towers spaced $0.4d$ apart. Data is shown as a) the time-varying series over the first second of measurement and b) a Power Spectral Density plot for the full 10-minute measurement.

zero over a long time, since they are respectively oscillatory and stochastic effects. Given the vortex shedding frequency of 13 Hz observed for the tower, the 60 s measurement window adopted is long enough to allow time-averaged measurements to be used without error.

5.6.3 Electrical Noise and Spectral Analysis

Fourier transform analysis of typical measurements of streamwise velocity, using Matlab's FFT function, can be used to calculate the Power Spectral Density (PSD) of each signal, giving a measure of the power contained within the signal at each frequency. Neglecting 0 Hz (i.e. the mean value), typical PSD plots for both U_x (Figure 5.10a) and disc load (Figure 5.10b), show the distribution of signal power across the frequency spectrum. It should be noted that these two plots are taken from the same 60 s sampling window, when the ADV probe was in position behind Disc 3, and thus show the flow behind the disc load presented, measured simultaneously.

It can be seen that the PSD of the U_x signal shows distribution of power across the frequency spectrum with a smooth attenuation away from low frequencies, as might

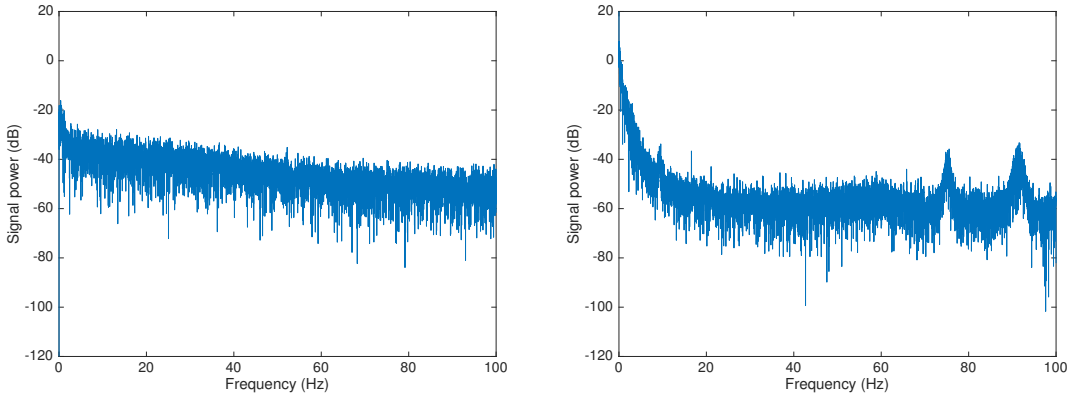

(a) PSD of U_x, $0.3d$ downstream of Disc 3 (b) PSD of the load force recorded on Disc 3

Figure 5.10: Power spectral density plots of U_x and disc load, taken for Disc 3 in the $\Theta = 0.3$, $s/d = 0.2$ array, neglecting mean values.

be expected from turbulent flow. The PSD of the disc load signal, while similar, also shows an unexpected increase in signal power around 75 Hz and again around 90 Hz. A power increase around these frequencies was seen consistently across all discs, across multiple tests, and is therefore considered highly likely to be the result of electrical interference from other equipment in the vicinity. The cables connecting strain gauges to the measuring equipment, although electrically shielded, were all several metres long, and had to be routed past the power cables to the ADV traverser, among other possible sources of interference. A similar analysis of the PSD of both the U_x and tower strain gauge measurements with no flow present, i.e. in still water, as shown in Figures 5.11a and 5.11b, shows no such high-frequency peaks. (Note that the raw strain gauge data is interrogated here since this still water reading forms the 'zero' load condition for normal load calculations, and as such the actual load on the disc cannot be calculated in this case without use of calibration offset data which is not used elsewhere.) It was therefore concluded that these peaks are likely due to other equipment involved in the experimental testing, such as the water pumps or the traverser motors, and that it could not therefore be easily excluded once the experiments had commenced.

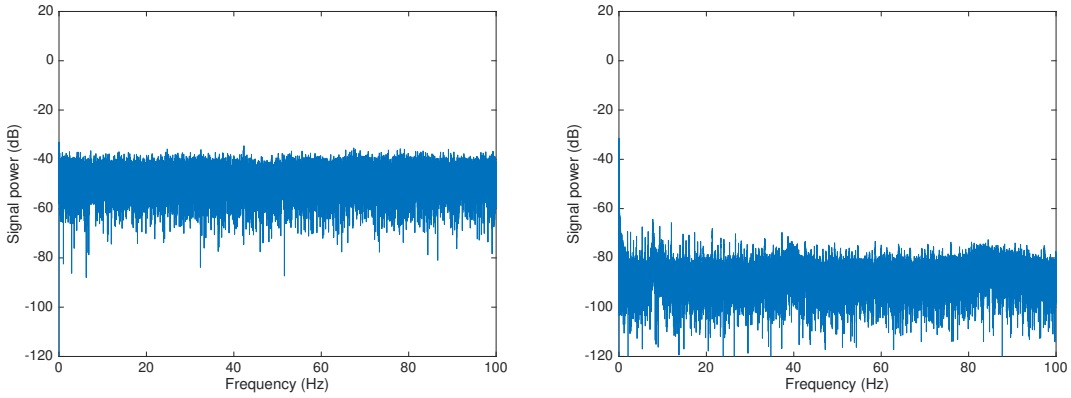

(a) PSD of U_x with no flow

(b) PSD of the raw strain gauge data recorded for Tower 3 with no flow

Figure 5.11: Power spectral density plots of U_x and disc load, taken as part of a still water measurement for a $s/d = 0.2$ array, neglecting mean values.

However, the peak power seen at these frequencies with operational flow is consistently around -40 dB, always at least 20 dB less than the signal power due to flow excitation seen at low frequencies (i.e. $\lesssim 10Hz$), and significantly below the power of the mean signal, generally recorded at around 30 dB. It is concluded that this noise is sufficiently low to be considered insignificant when calculating mean disc loads. Additionally, the time-varying component of the disc load measurement is not considered within the results presented, since it is dominated by the low frequency turbulence and vortex-shedding properties of porous discs, which are not of interest for this study. Only time-averaged disc loads are of interest. Time-varying signal analysis is restricted to flow measurements only to explore turbulence; the flow measurement signal shows no such high-frequency peaks. The small high-frequency peaks in the disc measurements were deemed not relevant for the scope of the experimental testing.

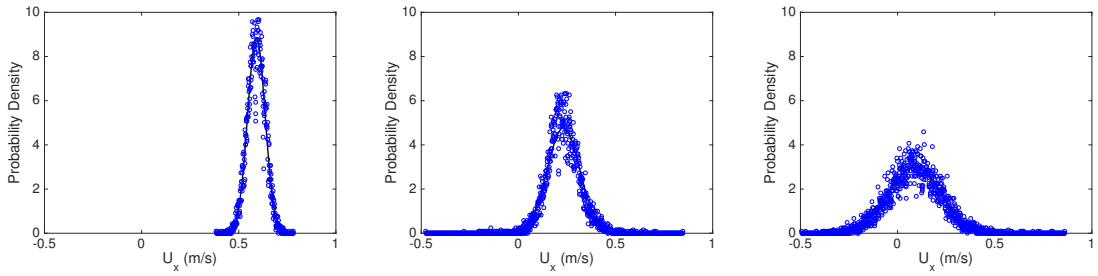

(a) Outer bypass (b) Array wake edge (c) Behind Disc 1 tower

Figure 5.12: Probability density of flow measurements taken at three points $0.3d$ behind a $\Theta = 0.35$, $s/d = 0.3$ array. Scattered probability density is shown for bin size of 1 mm/s flow speed. Solid line shows standard normal distribution PDF for the same mean and standard deviation as each sample.

5.6.4 Validity of Time-Averaged Measurements

The signal variance due to the lower frequency mechanical flow effects described above, however, may still be significant. It is therefore of interest to know whether the flow and load measurements are in line with a normal (or Gaussian) distribution, as might be expected from turbulent flow. A normal distribution has no skew; the mean value can be taken without concern for an asymmetric distribution around that mean.

Figures 5.12a to 5.12c show typical probability density results for flow measurements within this experiment. The values shown are taken from three different flow measurement points in the $0.3d$ downstream traverse behind an array of $\Theta = 0.35$ discs at $s/d = 0.3$ spacing. The three measurement points were chosen as: (a) a point in the outer bypass; (b) a point just inside the array wake where flow is strongly retarded and strong mixing is present; and (c) a point immediately behind the tower support of the first disc in the array, where negative U_x values may be seen. These three points are considered to represent the full spectrum of turbulent, chaotic flow regimes immediately behind the array. These are compared to standard normal distributions for the same values of mean and standard deviation, plotted using Matlab's native 'pdf' function.

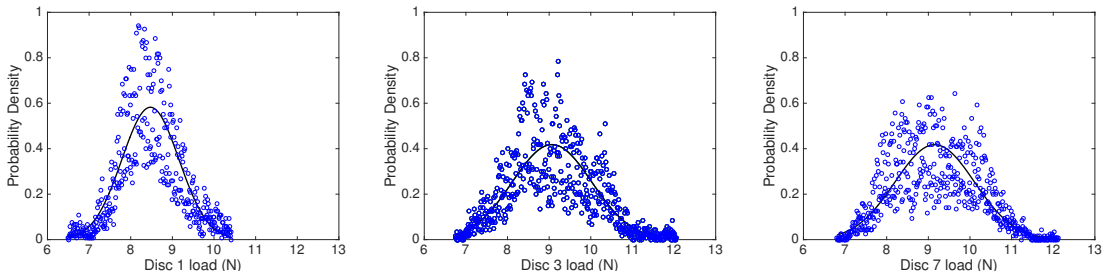

(a) Disc 1 (b) Disc 3 (c) Disc 7

Figure 5.13: Probability density of load measurements on three discs in a $\Theta = 0.35$, $s/d = 0.3$ array. Scattered probability density is shown for bin size of 0.01 N. Solid line shows standard normal distribution PDF for the same mean and standard deviation as each sample.

All three measurement points display a very close match to a normal distribution, despite their differing flow conditions. The mean values of these 60 s measurements are therefore representative of the flow. The fit is also sufficiently good that data can be used to calculate quantities such as Reynolds stresses which rely on the time-variant flow components.

For the same array, typical examples of load probability density are shown in Figures 5.13a to 5.13c for multiple discs. Although considerably more scatter is observable for load than for U_x, they still broadly conform to a normal distribution, and are equally weighted around the mean, so that average measurements are reliable for analysis. The cumulative nature of the thrust data, collected over multiple 60 s long measurement periods, ensures additional robustness of the averaged data.

This analysis indicates that the flow measurements are of sufficiently high quality to allow average flow speeds and time-varying turbulent quantities to be analysed. Similarly, all load measurements required for further analysis can be extracted as time-averaged values, with no further quality processes required.

5.7 Data Sets

The data presented in Chapter 6 comprises two sets of data from two periods of experimental work in the same facility and with the same equipment, approximately six months apart (Oct-Nov 2014 and Apr-Jun 2015). The first set of tests was carried out to investigate the parameter space and explore where areas of interest, such as peak power extraction, might lie. The second set of tests then focused on exploring these areas more fully. There is significant overlap between the configurations tested in both sets, however the second set of experiments forms the more complete exploration of the parameter space of interest. Tables 5.4a and 5.4b show the configurations tested in both sets of experiments. It can be seen that the second set includes more measurements of high blockage and high thrust arrays, with closer spacing and higher disc resistance; it was found from the first set of tests that this was the area where a point of peak power extraction might lie.

Upon taking the measurements of the overlapping configurations, a significant discrepancy in the thrust measurements recorded between the first and second sets of tests was discovered. Global thrust measurements were consistently lower in the second set of tests by approximately 7-8% across all configurations. The reason for this could not be determined during the second set of tests and subsequent analysis. During this second set of tests, once the discrepancy had been found, strain gauge calibration was repeated four times and every part of the thrust measurement system was fully checked to ensure no bias was entering the measurements through the amplifiers or wiring connections. Physical set-up variables were also investigated to check how they affected the thrust measurements: shimming of the support structure was undertaken to achieve a small amount of non-verticality in the towers and discs; the entire array was offset by 30 mm in the cross-stream direction; one particular configuration (Θ=0.3, s/d=0.2) was fully retested three times in each of these conditions to ensure repeatability. There was no significant flow speed discrepancy in the

Array Dimensions			**Θ (Open Area Ratio)**						
s/d	B_A	w_A	0.25	0.3	0.35	0.4	0.45	0.5	0.6
0.05	0.45	2.27 m							
0.1	0.48	2.38 m		✓x o	✓x	✓x			
0.2	0.52	2.59 m		✓x	✓x	✓x	✓x	✓x	✓x
0.3	0.56	2.81 m		✓x	✓x o	✓x			
0.4	0.60	3.02 m		✓x	✓x	✓x o			

(a) First Tests, Oct-Nov 2014

Array Dimensions			**Θ (Open Area Ratio)**						
s/d	B_A	w_A	0.25	0.3	0.35	0.4	0.45	0.5	0.6
0.05	0.45	2.27 m	✓x	✓x	✓x	✓x			
0.1	0.48	2.38 m	✓x	✓o	✓	✓			
0.2	0.52	2.59 m	✓x	✓	✓	✓			
0.3	0.56	2.81 m	✓x	✓	✓	✓			
0.4	0.60	3.02 m	✓x	✓	✓	✓			

(b) Second Tests, Apr-Jun 2015

Table 5.4: Array Configurations. Wake traverses taken for each configuration are indicated as follows: ✓- $0.3d$; x - $1d$; o - other traverses further downstream.

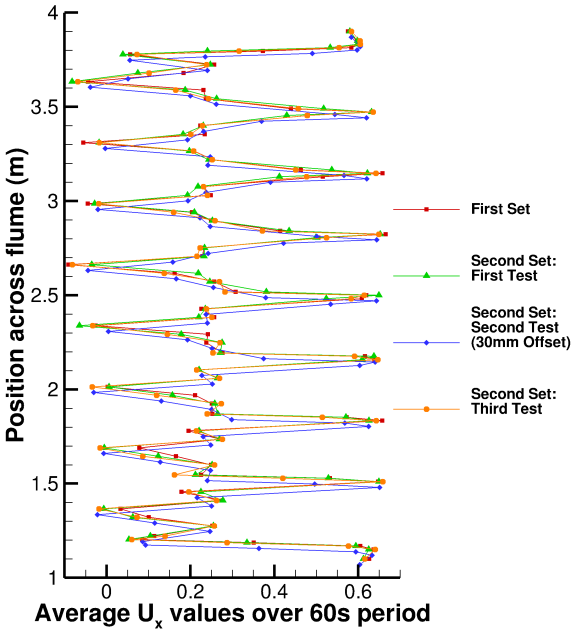

Figure 5.14: Comparison of $0.3d$ downstream wake traverse measurements taken in the first set of tests to three retests taken in the second set, including one taken with the entire array 30 mm offset from the flume centreline.

measurements taken between these retests and the earlier set of tests, as shown in Figure 5.14. This figure shows the similarity of the downstream profiles between the first set of tests and the second set, including retests, for this specific configuration, meaning that a change in flow behaviour within the facility was ruled out as a possible cause of the difference in thrust measurements.

It was concluded that nothing physical had changed in the testing environment between the two sets of tests. However, the total array C_{TG} was found to vary no more than 1% between the three retests taken during the second set of testing, between 1.6316 and 1.6413, whilst the same array in the first set of tests had recorded a C_{TG} of 1.757. The possibility of dependence on Reynolds number was considered, as the two sets of tests took place at different times of year with different ambient temperatures. This same configuration was retested at 70% flow speed to represent the most extreme possible change in Reynolds number (equivalent to a 10°C reduction in water temperature). This also gave a value of C_{TG} only 1% higher than the lowest

recorded in the other retest, at 1.6468. The variability of up to 1% is much more in line with expectation of measurement error for this experiment. Given the recalibration, system checking, sensitivity studies and retesting carried out in the second set of experiments, it was determined that strain gauge measurements taken in the second set of tests were robust, and therefore that those taken in the first set of tests could not be trusted. The load measurements from the first set of tests have been discarded and are not reported within this thesis. All thrust and power data presented are taken only from the second set of tests.

However, given the similarity between wake flow measurements as discussed above, it is not believed that there is any reason to discard flow measurement data from the first set of tests, particularly where this can shed additional light on features of the fluid dynamics involved. In some cases, additional flow measurements were taken in the first set of tests which were not repeated in the second set of tests due to time constraints (such as some $1d$ downstream traverses). Where these cases are of interest, therefore, flow data are presented from the first set of tests. Where this is the case, it is made clear that these measurements are from the first set of tests.

5.8 Inferred Power and Disc Flow Averaging

Point measurements of flow speed were taken downstream of every array to investigate the power removed from the flow by the array. This can be calculated from the standard relationship $P_{\text{disc}} = T_{\text{disc}} U_{\text{disc}}$, where P_{disc} and T_{disc} are respectively the power removed at the array plane and the thrust experienced by a single disc. U_{disc} is the time-averaged component of flow speed through the disc in the x-direction, averaged over the area of the disc. Within this experiment, however, it was not possible to measure U_{disc} directly. An ADV probe measures flow speed through calculation of the doppler shift in acoustic pulses that it sends out after they reflect from moving

particulates within the flow. Any stationary objects nearby, such as flume boundary walls or a porous disc, will also reflect these acoustic pulses, introducing noise into the signal and error into the measurement. While it is obviously impossible to obtain U_{disc} directly, this also places a restriction on how closely downstream U can be measured without incurring large amounts of error. The control software for the specific Nortek Vectrino^{+} ADV probe used in this experiment reports signal correlation within its quality data. A series of initial tests were therefore carried out with the ADV probe positioned at various flow depths directly behind the centre of a disc, $0.2d$, $0.25d$ and $0.3d$ downstream, and the signal correlation was monitored. The correlation of the ADV signals was found to vary particularly strongly across these downstream positions. At $0.2d$ downstream, the average correlation was found to be approximately 50%. At $0.25d$ downstream, this increased to an average 70%, and at $0.3d$ had risen to an average 80%, with all measurement points showing correlation above 70%. A baseline of 70% correlation was also observed in freestream measurements with no nearby reflective surfaces. Therefore, $0.3d$ downstream was determined to be the closest point to the array at which flow measurements should be taken to avoid introducing significant error through reflections from the array.

The concept of 'inferred power' was introduced to allow investigation of power removed by the array. This is defined as $P_{\text{disc,inferred}} = T_{\text{disc}} U_{\text{disc},0.3d}$, where $U_{\text{disc},0.3d}$ is the average streamwise velocity of the flow behind each disc at $0.3d$ downstream. The inferred power will always be lower than the true power removed from the flow by each disc, since the flow will continue to decelerate downstream of the disc as pressure recovery takes place (i.e. $U_{\text{disc},0.3d} < U_{\text{disc}}$ in all cases). The proportional decrease of U_{disc} to $U_{\text{disc},0.3d}$ is not fixed across all cases, since the length of the wake and the mixing processes are a function of array thrust, array geometry and blockage ratios. Theoretically, it would be possible to estimate the relationship between $U_{\text{disc},0.3d}$ and U_{disc} for each configuration using assumptions from Betz and from partial fence theory.

However, this has two drawbacks. Firstly, the analytical models do not allow for physical distances, so the total length of the wakes behind each disc and array would need to be measured in order to calculate the proportional length of $0.3d$ to the entire wake. This was considered impractical within this experimental set-up. Secondly, since the purpose of this experimental work was to compare to analytical theory, it is unhelpful to implicitly include the basic assumptions of analytical theory within the core measurements being taken. Therefore, $U_{\mathrm{disc},0.3d}$ and inferred power are compared consistently across all array configurations.

A number of point measurements of flow speed in the x, y and z directions were taken at mid-depth using the Nortek Vectrino^{+} ADV probe. Due to the quantity of discs in each array, and the 60 seconds required for robust flow speed measurement at each point, flow speeds were measured at 5 points only behind each disc: at the disc centre, and at $r/3$ and $2r/3$ on each side (i.e. -90 mm, -45 mm, 0 mm, 45 mm and 90 mm horizontal positions relative to the centre of each disc). A method to obtain an average $U_{\mathrm{disc},0.3d}$ from the U_x component of these measurements for each disc was therefore required.

Initially, a simple arithmetic mean of the five measurements was considered. However, this had a number of drawbacks. Firstly, the central measurement of U_x directly behind the centroid of the disc was found to be strongly influenced by the presence of the support tower, which obscures the disc at this point. U_x was therefore found to be significantly retarded at this point, and became negative for the discs with highest resistance to the flow, as can be seen for e.g. discs 1 and 4 in Figure 5.15. This negative flowspeed was not considered to be representative of the flow throughout the central portion of the disc, but almost entirely an artifact of the presence of the tower. This value was therefore removed from the calculation, however an arithmetic mean of the other four measurements, implying a square plug profile in the disc wake, is still an over-simplification. A weighting method was then considered, whereby each

point measurement of velocity was weighted by an appropriate annulus area:

$$U_{\text{disc},0.3d} = \left(\frac{U_{2r/3} + U_{-2r/3}}{2} \pi (r^2 - (\frac{r}{2})^2) + \frac{U_{r/3} + U_{-r/3}}{2} \pi ((\frac{r}{2})^2 - (\frac{r}{6})^2) + U_c \pi (\frac{r}{6})^2 \right) / A_{\text{disc}} \tag{5.2}$$

where A_{disc} is the disc area, r its radius and the subscripts on U denote measurements taken behind the centre of the disc or at the $\pm r/3$ and $\pm 2r/3$ positions. Alternatively, if omitting the central measurement, this becomes:

$$U_{\text{disc},0.3d} = \left(\frac{U_{2r/3} + U_{-2r/3}}{2} \pi (r^2 - (\frac{r}{2})^2) + \frac{U_{r/3} + U_{-r/3}}{2} \pi (\frac{r}{2})^2 \right) / A_{\text{disc}} \tag{5.3}$$

It was considered whether this method could be further improved through the use of interpolation and extrapolation to give an estimated flow speed at every radius across the disc. Due to the low number of point measurements, linear methods were used to interpolate between all five points measured and extrapolate to the edges of the disc beyond the outer points, as shown by the solid blue lines in both Figures 5.15 and 5.16. However, this method was found to be somewhat unreliable. A flaw inherent to this method is that the estimated flow speed with highest error will always be that at the outer edge of the disc, as it represents the furthest point from any measurement taken and is calculated from extrapolation rather than interpolation. Due to the geometry of the discs, however, this is the flow speed which is weighted most heavily by annulus area when integrating to calculate the average flow speed across the disc, compounding the error. Particularly in cases of high disc resistance (and therefore higher turbulence), the outer measurements taken on each disc (at $-2r/3$ and $2r/3$) were not always found to be higher than those taken at $-r/3$ and $r/3$, causing a linear extrapolation to predict a continued reduction in flow speed towards the outer edge of the wake, as can be seen for all discs in Figure 5.16. This is not physically

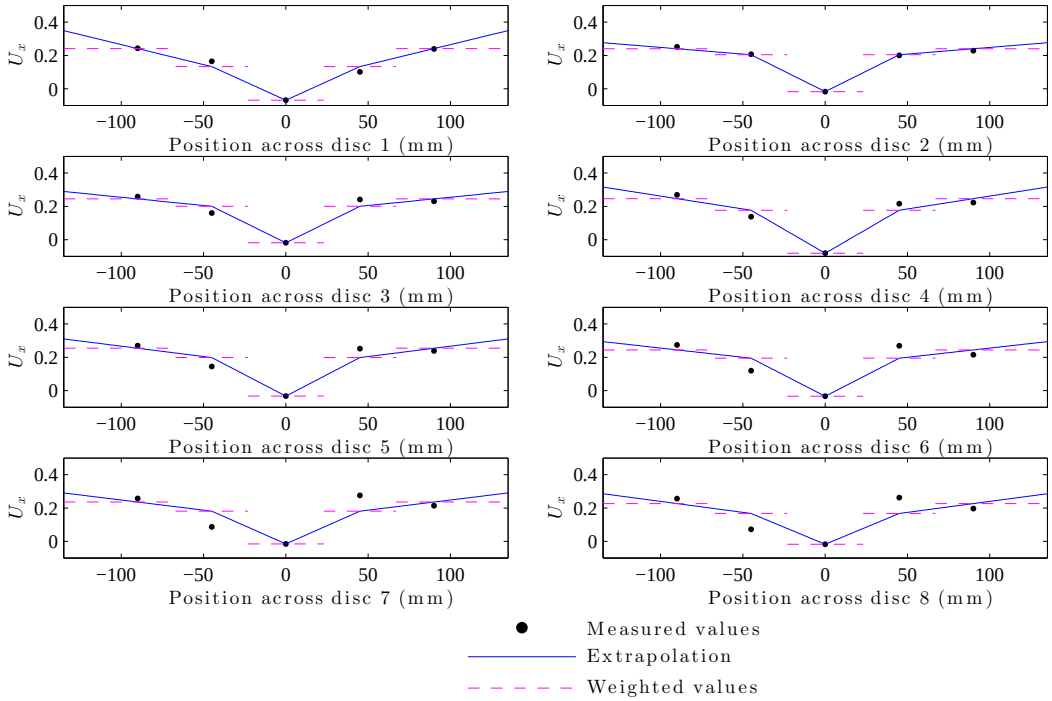

Figure 5.15: Raw velocity measurements, extrapolation and weighted assumptions at $0.3d$ downstream behind an array of $\Theta = 0.3$ discs with $s/d = 0.2$ spacing.

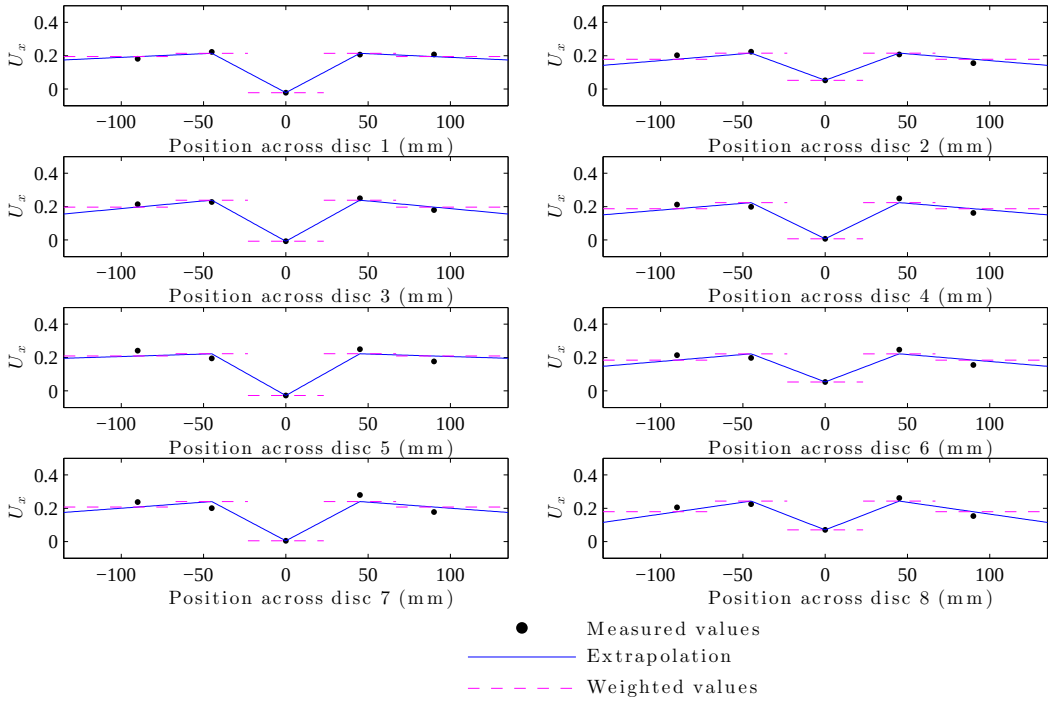

Figure 5.16: Raw velocity measurements, extrapolation and weighted assumptions at $0.3d$ downstream behind an array of $\Theta = 0.25$ discs with $s/d = 0.1$ spacing.

realistic and clearly creates a large error in the estimated flow speed at the outer edges of the disc. Additionally towards the outer edges of the disc fence, array wake expansion even within the 8.1 cm to $0.3d$ downstream also meant that the points at which measurements were taken, while centred on disc position, might not be as central within the disc wake as desired. This could introduce further error into the assumptions of the interpolation/extrapolation method.

After careful consideration of each of these measurements, it was decided to proceed with calculating inferred power based on an average speed calculated from area weighting of the $\pm r/3$ and $\pm 2r/3$ measurements, with no interpolation or extrapolation, as shown by the dashed lines in Figures 5.15 and 5.16. The central measurement, directly behind the tower support, was omitted as being unrepresentatively retarded compared to the wake flow surrounding it. Double-checking the results produced with or without this measurement in the area weighting method showed that, since it only acts across the small central area of the disc, the only impact was to slightly reduce the overall power calculated for all configurations. Its omission did not at all affect the trends of power extraction across configurations.

Chapter 6

Partial Array Experimental Results

6.1 Partial Fence Theory

The scoping exercise, described in Chapter 4, provided the basis for a full suite of experiments on a partial fence array of eight porous discs. This work was designed to investigate the predictions of the model for a partial fence array, developed by Nishino and Willden [87], as detailed in Section 3.2.2. This is an analytical model built on the assumptions of Linear Momentum Actuator Disc Theory (LMADT), showing that optimisation of different blockage ratios in combination with device characteristics such as induction factor could increase the available power from the case of a homogeneous fence of tidal turbines stretching across the entire width of a channel. For such fence arrays, a peak power point is found in terms of array geometry (and hence blockage characteristics), which could be exploited by devices with the correct thrust behaviour to extract the maximum power. This analytical model was compared to computational results by Nishino & Willden [88] with reasonable agreement. However, no previous experimental work has explored a sufficient number

of devices and adequate measurements of thrust across all devices to experimentally confirm this theory. The primary intention of the experimental work described here was to investigate whether the theory's prediction of increased thrust and power was realisable at experimental scale.

A number of assumptions are made for theoretical analysis to allow the governing equations to be solved. First, it is assumed that device-scale mixing and array-scale mixing occur at different length scales, and that device-scale mixing is complete before the onset of array-scale mixing. Second, the partial fence is assumed to be of quasi-infinite width, meaning that every device and device wake is considered to be identical to each other. These assumptions allow both the device scale problem and the array scale problem to be solved numerically, coupled only by the equality of applied thrust across both scales. An intention of the experimental work is therefore to examine the validity and limitations of these assumptions.

It should be noted that the analytical theory has been amended to consider wake expansion correction factors, to allow for the case of a finite short fence array instead of a quasi-infinite one. A comparison to computational results shows reasonable agreement [88]. The results of the experimental work described here, however, could not be compared to the amended model, since it was not possible to calculate the non-dimensional wake expansion coefficients from the measurements taken. The comparison is instead made against the uncorrected model of [87]. However, one finding from the later paper [88] was used to inform the experimental design; partial fence arrays of different lengths were considered, with numbers of devices in the array varying from 2 up to 40. It was found, as expected, that longer arrays behaved more like the quasi-infinite theory. An array of 8 devices was computationally investigated in some detail, as forming a compromise between ideal power output and a realistic size of fence array which might be constructed. An eight disc array was similarly chosen for the experiments as an array size at which partial fence array effects ought to exist,

but which is testable at a reasonable disc size within the Manchester facility.

This chapter describes the results obtained from the experimental testing, including thrust, power and flow behaviour for multiple 8-disc configurations. Note that, as discussed in Section 5.7, thrust and power results are reported exclusively from the second set of tests carried out, due to concerns over the quality of thrust data from the first set of tests. However, some data on wake behaviour from the first set of tests is presented in addition to data from the second set: this is highlighted wherever these results are included.

6.1.1 Disc Resistance

Prior to comparing experimental results to theory, it was necessary to establish whether the porous discs, designed in accordance with Equation (4.3) to give a desired pressure coefficient κ, were in fact resisting the flow to the desired degree. While, as with the power calculation described in Section 5.8, it was not possible to measure the discs' κ values directly, due to the inability to measure U_x in the disc plane, a representative '$0.3d$ downstream' $\kappa_{0.3d}$ value can be calculated from the thrust and flow measurements taken for every array tested. Given flow deceleration behind the discs, and the κ relationship defined in Equation (4.2), this value is expected to be greater than the real κ value of the discs (i.e. $\kappa_{0.3d} > \kappa$). The computed values for $\kappa_{0.3d}$ in each configuration are shown in Table 6.1, and are approximately 30% lower than the values computed via the $\kappa - \Theta$ relationship of Equation (4.3), κ_Θ. Hence, $\kappa_\Theta > \kappa_{0.3d} > \kappa$ and thus Equation (4.3) cannot be taken as a good approximation for these discs. Ideally, this $\kappa - \Theta$ relationship would have been revisited with the experimental data gathered, to allow better disc design. However, given the inability to measure true κ, and the probability that it varies with blockage or wake mixing conditions, the data gathered was insufficient to allow such a study. As this was not the focus of this experimental work, however, it was decided to continue with

		s/d				
Θ	κ_Θ	**0.05**	**0.1**	**0.2**	**0.3**	**0.4**
0.25	**15**	10.78	10.03	9.95	9.53	9.18
0.3	**10.11**	6.97	6.81	7.01	7.11	7.26
0.35	**7.16**	5.30	5.35	5.50	5.60	5.93
0.4	**5.25**	3.58	3.65	3.77	3.97	4.05

Table 6.1: $\kappa_{0.3d}$ evaluated from total thrust and $U_{0.3d}$ for each array, compared with κ_Θ predicted by Equation (4.3).

the discs as created and evaluate results using the measured $\kappa_{0.3d}$ only, rather than the expected κ_Θ. In the following sections, results are therefore reported against the design open-area ratio, Θ, but also where relevant the measured pressure coefficient, $\kappa_{0.3d}$.

6.2 Results: Thrust and Power

6.2.1 Thrust Variation Across Configurations

A plot of the variation of the experimental global thrust coefficient, C_{TG}, is shown in Figure 6.1a. The red diamonds on this plot mark the experimental measurements taken in the second set of tests, with numerical values shown in Table 6.2. The contours are interpolations (using basic triangulation methods native to Tecplot® plotting software) between these twenty points to show trends. The theoretical variation in C_{TG} as predicted by analytical theory across the same parameter space is shown in Figure 6.1b.

It can be seen that there is a significant difference in the magnitude of the global thrust coefficient measured in experiments versus that expected by theory. This is likely to be due to differences between the behaviour of a finite eight disc fence array and the quasi-infinite fence assumed by theory. In addition to the difference in magnitude of recorded C_{TG}, a further difference is seen to be that in the theory,

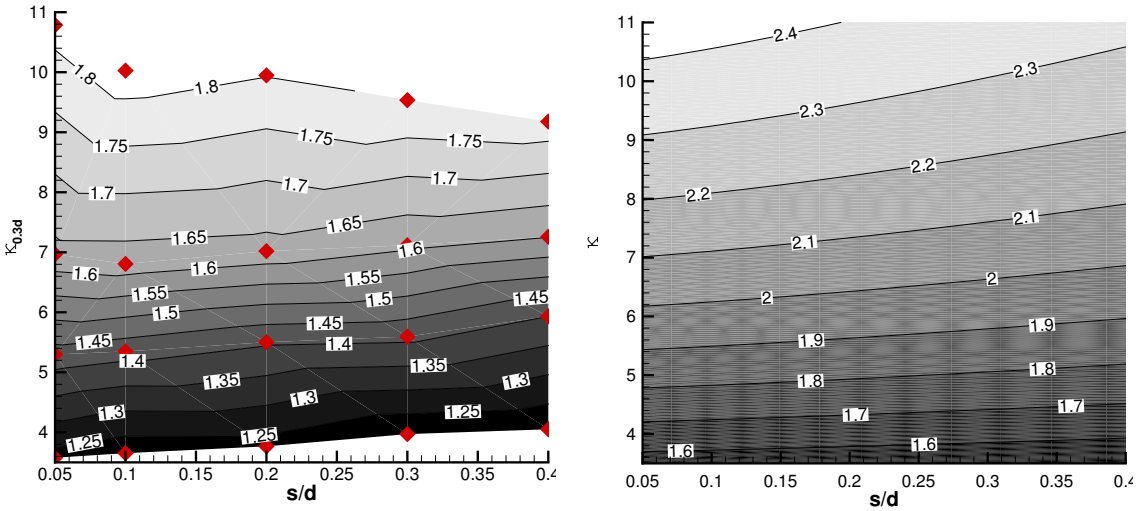

(a) Experiment

(b) Theory

Figure 6.1: Contours of global thrust coefficient as measured experimentally and as predicted by theory. Red diamonds mark the actual experimental measurements taken as detailed in Table 6.2: contours on plot a) are interpolated from these.

C_{TG} continues increasing as local blockage is increased; i.e. moving towards the left of the plot as disc spacing is decreased. However, this effect is considerably weaker in the experimental data presented: while thrust clearly increases with decreasing disc porosity, the correlation with decreasing spacing is not as strong. There is even a slight drop-off visible at the closest spacing and highest thrust; for the $\Theta = 0.25$ arrays at $s/d = 0.1$ and $s/d = 0.05$, C_{TG} reduces from 1.8336 to 1.8238 respectively. These measurements are still close, potentially within the margin of overall error. As such, although there are clear trends of increasing thrust with decreased spacing, the data do not absolutely prove an ability to carry continually increasing thrust as inter-disc spacing is reduced, as predicted by the theory.

This discrepancy between theory and experiments in terms of both magnitude and general trends may be due to the end effects inherent to a finite fence array. The theory assumes a quasi-infinite array length, allowing the assumption that all devices and device wakes within the array behave identically. A finite fence will not support a homogeneous high thrust across all eight discs, since the outer discs will experience

Θ	$\kappa_{0.3d}$	s/d 0.05	0.1	0.2	0.3	0.4
0.25	≈ 10	1.8238	1.8336	1.8017	1.8028	1.7845
0.3	≈ 7	1.6390	1.6260	1.6316	1.6106	1.6015
0.35	≈ 5.5	1.4323	1.4190	1.4064	1.4121	1.4031
0.4	≈ 4	1.2353	1.2187	1.2334	1.2100	1.2092

Table 6.2: Global thrust coefficient for each configuration from experimental measurements. The highest value is highlighted in blue.

additional effects due to flow diverting around the ends of the array rather than being forced through the discs. The thrust on the end discs will therefore be lower. This effect is shown by the distribution of C_{TG} across all discs in Figure 6.2 for the $\Theta = 0.3$ discs. The thrust coefficient in this plot is normalised by the area of each single disc, as with a local thrust coefficient, but uses the global array upstream flowspeed. It is therefore denoted as $C_{TG\text{disc}}$, so the total array C_{TG} is simply the average of all $C_{TG\text{disc}}$ values shown for that array. This plot shows a number of relevant effects, although it is biased by asymmetry of the flume flow as discussed in Section 5.3. Note that $C_{TG\text{disc}}$ is plotted against disc number, not the physical position of discs within the flume. This enables comparison of results across different array spacings. Disc 1 is the disc furthest from the y origin as shown in Figure 5.4, disc 8 closest to it.

It can be seen that asymmetric thrust occurs across every array, which is considered likely to be due to the asymmetry of the flume's undisturbed flow (as discussed in Section 5.3) combined with some feedback effects due to the presence of the array. Neglecting this bias, however, it can be seen that a quasi-parabolic distribution of thrust coefficient across the array exists in all cases, with central discs mostly sustaining higher thrust than those towards the outer edges. A slight increase in thrust across all discs can be seen as spacings are reduced, contributing to the trends for the whole array shown in Figure 6.1a and Table 6.2; however, a particularly large drop-off in thrust is seen on the two outer discs, 1 and 8, in the most closely spaced

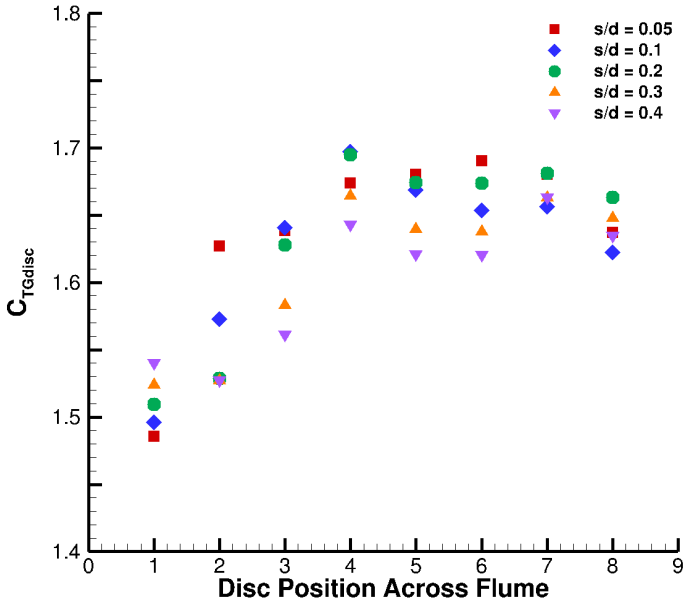

Figure 6.2: Individual values of $C_{TG\text{disc}}$ for arrays of $\Theta = 0.3$ discs at all spacings. Discs are numbered from left to right as viewed from upstream.

$s/d = 0.05$ and $s/d = 0.1$ cases. It can be seen that, if all discs were able to sustain the same thrust as those in the centre, the $s/d = 0.05$ array could achieve a C_{TG} value of approxmately 1.68, instead of the average 1.64 observed, an increase of 2.4%. Thus, the individual disc measurements confirm that end effects exist for this relatively short partial fence, and that they limit the thrust behaviour of the array.

6.2.2 Inferred Power Variation Across Configurations

Similar to the thrust coefficient, the measured values of inferred global power coefficient can be compared to the theoretical power coefficients, as shown in Figure 6.3. Again, the experimental contours are interpolations based on a triangulation of the twenty measurements taken, each marked with red diamonds on the plot (and shown in Table 6.3 for reference). This data is plotted against $\kappa_{0.3d}$ rather than κ_Θ derived from the empirical Equation (4.3).

A difference is once again seen between experiment and theory. The reduction in

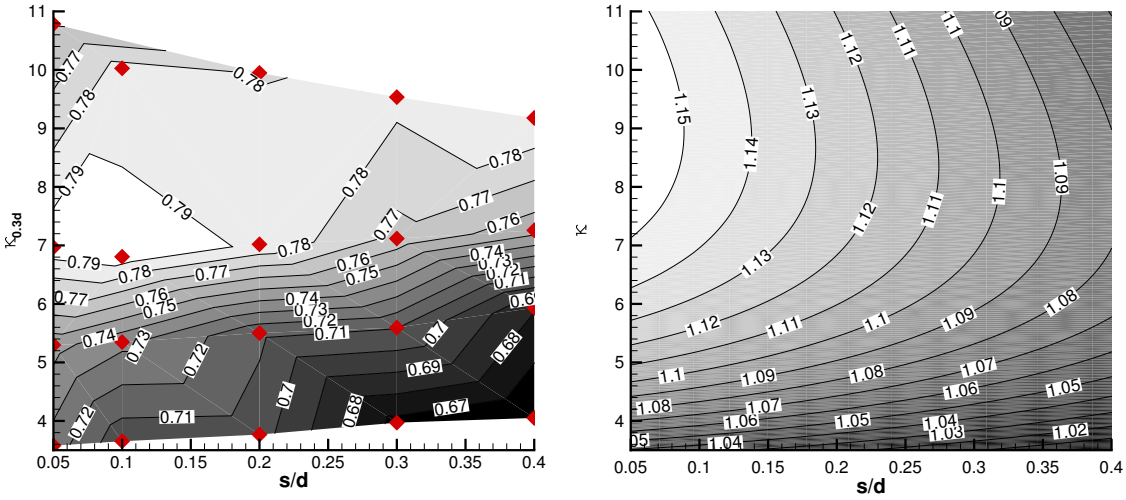

(a) Experiment (Inferred)

(b) Theory

Figure 6.3: Contours of global power coefficient as measured experimentally (using inferred power calculation) and as predicted by theory. Red diamonds mark the actual experimental measurements taken as detailed in Table 6.3: contours on plot a) are extrapolated from these.

magnitude of the power coefficient is partly due to the drop in C_{TG} already observed, and partly due to inferred power always being lower than true power (as previously discussed given that $U_{\text{disc},0.3d} < U_{\text{disc}}$). Importantly, there is also a slight shift in the potential peak power coefficient location. Partial fence theory predicts that as a homogenous fence of identical devices, equally spaced within the fence array, is brought closer together (reducing s/d), there will eventually be a peak power coefficient available at an appropriate combination of s/d and Θ. Beyond this point, however, the flow through the array will choke, with flow diverting around the outside of the array, so the available power will drop. For this array, with a global blockage of 0.2, the theory does not predict peak power occurring until a spacing lower than $s/d = 0.05$ is reached. This was not tested experimentally due to the extremely low disc spacings required ($0.05d = 13.5$mm). The theory also predicts a drop-off in power as disc resistance is increased above approximately $\kappa = 9$.

In the experimental data it can be seen that the peak inferred power coefficient, although perhaps still outside the parameter space tested, has shifted towards the

Θ	$\kappa_{0.3d}$	s/d 0.05	0.1	0.2	0.3	0.4
0.25	≈ 10	0.7613	0.7865	0.7793	0.7854	0.7920
0.3	≈ 7	0.7991	0.7954	0.7887	0.7668	0.7545
0.35	≈ 5.5	0.7461	0.7328	0.7122	0.7105	0.6831
0.4	≈ 4	0.7277	0.7053	0.7064	0.6689	0.6614

Table 6.3: Global inferred power coefficient for each configuration from experimental measurements. The highest value is highlighted in blue.

bottom of the plot, and away from the left axis. This implies that the performance of this array is more negatively affected by both high disc resistance and closer spacing than the theory would predict. The real arrays tested were able to remove highest power from the flow in the $\Theta = 0.3$ ($\kappa \approx 7$) disc arrays, with a drop-off occurring more steeply towards the $\kappa \approx 10$ array than the prediction. As shown in Figure 6.3a, peak values were found for $\Theta = 0.3$ discs at their closest spacings, with C_{PG} values of 0.7954 and 0.7991 at $s/d = 0.1$ and $s/d = 0.05$ respectively.

Some of the discrepancy at close spacings may be explained by geometric considerations: the analytical model contains no specified geometry for the actuator discs or channels, and in particular cannot replicate the anisotropy in bypass flow channel width around a circular disc within a rectangular local channel cross-section. At the closest spacings, the horizontal width of the bypass flow has become very narrow at mid-depth, even though the overall local blockage ratio is still reasonably modest. This will negatively impact the ability of the bypass flows to accelerate the core disc flow, thus incurring a negative impact on U_{disc} and on the extracted power.

A plot of inferred C_{PG} across all discs for $\Theta = 0.3$ and all spacings is presented in Figure 6.4, and shows the impact of end effects. Again, $C_{PG\text{disc}}$ is normalised on single disc area but with global upstream flowspeed, so that total array C_{PG} is the average of all $C_{PG\text{disc}}$ values. A small amount of flow asymmetry is still visible, and the general parabolic distribution of power across the array is much more pronounced

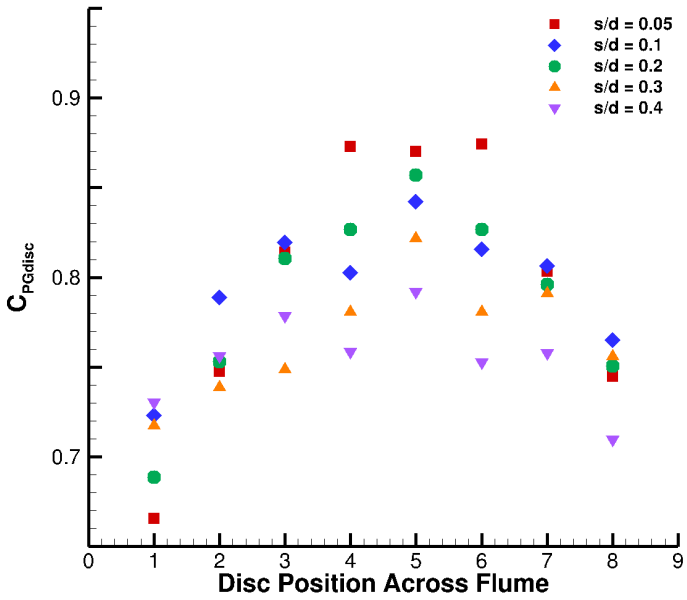

Figure 6.4: Individual values of $C_{PG\text{disc}}$ for arrays of $\Theta = 0.3$ discs at all spacings. Disc numbering is as shown in Figure 5.4

than for thrust. This shows the inability of the discs towards the array edges to extract as much power from the flow as those in the centre. This results in a much lower total C_{PG} for the array than might be possible if all discs could achieve the same power extraction as the central discs (e.g. an approximate 9% increase in the case of the $\Theta = 0.3$, $s/d = 0.05$ array).

6.2.3 Variation of Thrust and Power Across Array

End effects are of particular interest in the case of a real partial fence array, as the predicted increases in available power from the analytical theory may not be achieved in reality. The fact that real arrays are of finite length means that flow diversion around the array can reduce the total power and thrust values. The distribution of individual $C_{TG\text{disc}}$ and $C_{PG\text{disc}}$ values across all discs in the array can be examined to understand how this manifests across the length of a partial array such as this.

Figure 6.5 shows examples of the distribution of $C_{TG\text{disc}}$ and $C_{PG\text{disc}}$ across the

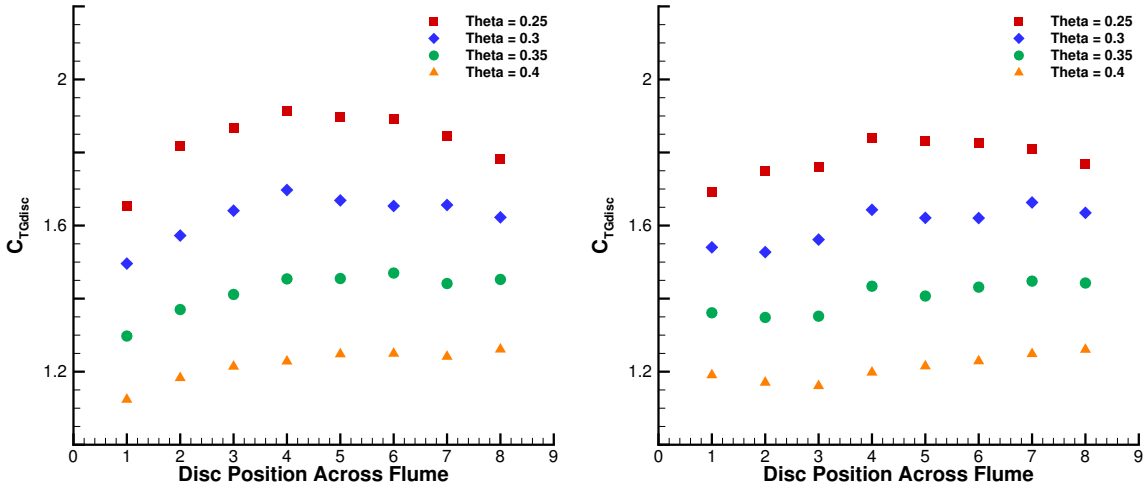

(a) $C_{TG\text{disc}}$, $s/d = 0.1$

(b) $C_{TG\text{disc}}$, $s/d = 0.4$

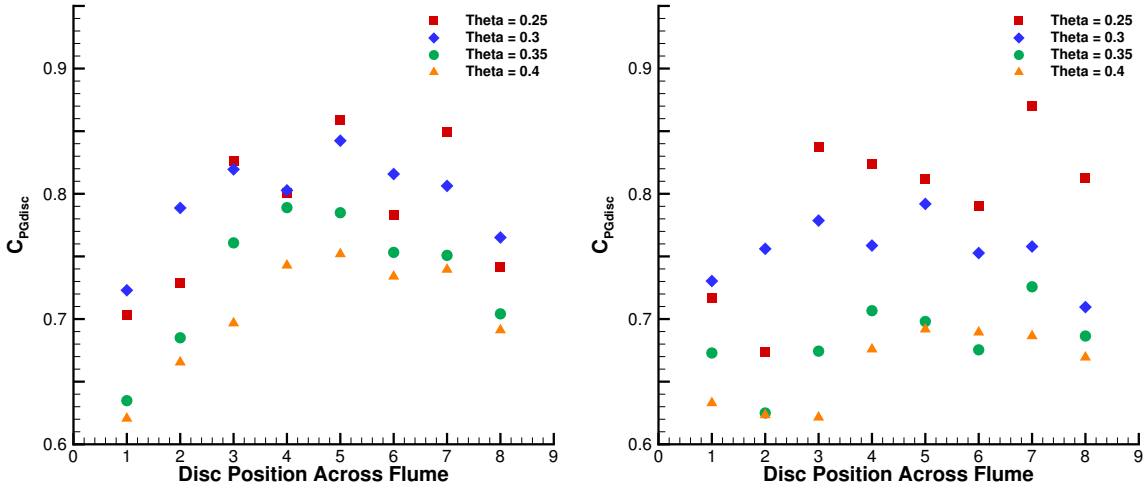

(c) $C_{PG\text{disc}}$, $s/d = 0.1$

(d) $C_{PG\text{disc}}$, $s/d = 0.4$

Figure 6.5: Values of $C_{TG\text{disc}}$ and inferred $C_{PG\text{disc}}$ calculated for all discs, shown for $s/d = 0.1$ and $s/d = 0.4$ array spacings for all disc porosities.

arrays, calculated as before, for a close spacing and a wide spacing, $s/d = 0.1$ and 0.4, for all porosities of discs tested. It can be seen that the broadly parabolic distribution of both thrust and power is much more of a feature for the closely spaced arrays. There is less coherent structure to the distribution of power and thrust for the more widely spaced arrays. It can also be seen that, within each array spacing, the higher thrust discs also develop more parabolic distributions than the lower thrust ones. This implies that end effects are more important for high thrust, closely spaced arrays: the same ones which benefit most from the partial fence effect to achieve the highest available power.

This effect can be quantified by considering the ratios of thrust and inferred power between the inner discs (discs 4 and 5) and the outer discs (discs 1 and 8) in each configuration. Tables 6.6a and 6.6b show these ratios for all configurations. It can be seen equally clearly here that the central discs experience higher thrust and extract higher power relative to the outer discs in almost all cases, and that this effect is more marked for the more closely spaced, higher disc resistance arrays. The difference in thrust coefficient can be seen to be up to 11% between the outer edge of the array and the centre, and for the power coefficient this rises to nearly 24%.

It is of interest to cross-reference these tables with the total global thrust coefficient of each array as shown in Table 6.2. It might be expected that the highest degree of end effects would correspond to the highest total array thrust, as more flow will divert around the array if it exerts greater force. However, it can be seen that this is not quite the case: the highest total thrust coefficients correspond to all five spacings of the $\Theta = 0.25$ discs, whilst the highest ratio of central power coefficient to outer is found with the closest spacing of the $\Theta = 0.3$ discs. Overall it can be seen that the arrays with the greatest achievable power, benefiting most from the partial fence effect, do generally display the greatest ratios in both thrust and power between innermost and outermost discs. End effects are therefore an intrinsic result of taking

			s/d		
Θ	**0.05**	**0.1**	**0.2**	**0.3**	**0.4**
0.25	1.1037	1.1087	1.0836	1.0716	1.0614
0.3	1.0739	1.0794	1.0618	1.0418	1.0280
0.35	1.0632	1.0578	1.0270	1.0130	1.0132
0.4	1.0444	1.0384	1.0094	1.0050	0.9844

(a) $C_{TG\text{disc}}$ ratio

			s/d		
Θ	**0.05**	**0.1**	**0.2**	**0.3**	**0.4**
0.25	1.1476	1.1487	1.1388	1.0909	1.0689
0.3	1.2359	1.1055	1.1696	1.0876	1.0769
0.35	1.1279	1.1754	1.1004	1.0849	1.0334
0.4	1.1633	1.1395	1.0803	1.0871	1.0502

(b) $C_{PG\text{disc}}$ ratio

Figure 6.6: Ratios of $C_{TG\text{disc}}$ and $C_{PG\text{disc}}$ between innermost and outermost discs, for all configurations. The highest value is highlighted in blue in each table.

advantage of partial fence effects to gain increased power extraction with any finite fence array.

6.3 Results: Flowfield Behaviour

In order to understand the trends of thrust and power behaviour, it is helpful to interrogate the data collected by the ADV probe across the downstream traverses for every array: not just the streamwise component U_x used in the inferred power and $\kappa_{0.3d}$ calculations, but also the cross-stream component U_y and vertical component U_z, plus the additional information on turbulence that can be calculated from their time-varying qualities.

As previously discussed in Section 5.7, two separate sets of tests were carried out, and although the thrust measurements from the first set of tests were discarded as erroneous, the flow measurements were sufficiently similar across both sets of tests

that they are considered equally valid. Both sets are interrogated within this section where relevant.

6.3.1 Wake Velocities and Expansion

When considering the data collected across both sets of tests, flow data was recorded for all configurations tested at both $0.3d$ and $1d$ downstream of the array, allowing mean and instantaneous flow quantities in the x, y and z directions to be investigated. A total of five measurement points were taken behind each disc, three in each internal bypass flow for the wider array spacings (two in the $s/d = 0.1$ configurations, and one in the $s/d = 0.05$ configurations), and at least 5 in each external bypass flow. An example of the mean flow field in the x-y plane, i.e. plan view, is shown in Figure 6.7 for four different spacings of the same porosity of disc, $\Theta = 0.35$. It should be noted that this figure is created from data drawn from the first set of tests undertaken, as the $1d$ downstream traverses were not repeated for these configurations in the second set of tests.

It can be seen that the flow behaviour is broadly as expected from the partial fence theory: as s/d is reduced and internal bypasses become narrower, the internal bypass flow is initially accelerated between the discs. Figure 6.7b, for example, clearly shows internal bypass flows at $0.3d$ downstream to be at higher speeds than the outer bypass flows. However, as inter-disc spacing is further reduced, these internal bypass flow speeds are also more rapidly retarded by mixing with the disc wakes, as seen at $0.3d$ downstream in Figure 6.7a. This can also be seen across the $1d$ downstream traverse for all four configurations shown here, with the internal bypass flow speed by this point progressively further reduced as disc spacing is reduced.

An additional aspect of the fluid behaviour which can be observed in these plots is the level of velocity gradient in the outer bypasses. At $0.3d$ downstream, an x-velocity shear can be seen developing in the $s/d = 0.1$ and $s/d = 0.2$ cases, while very little

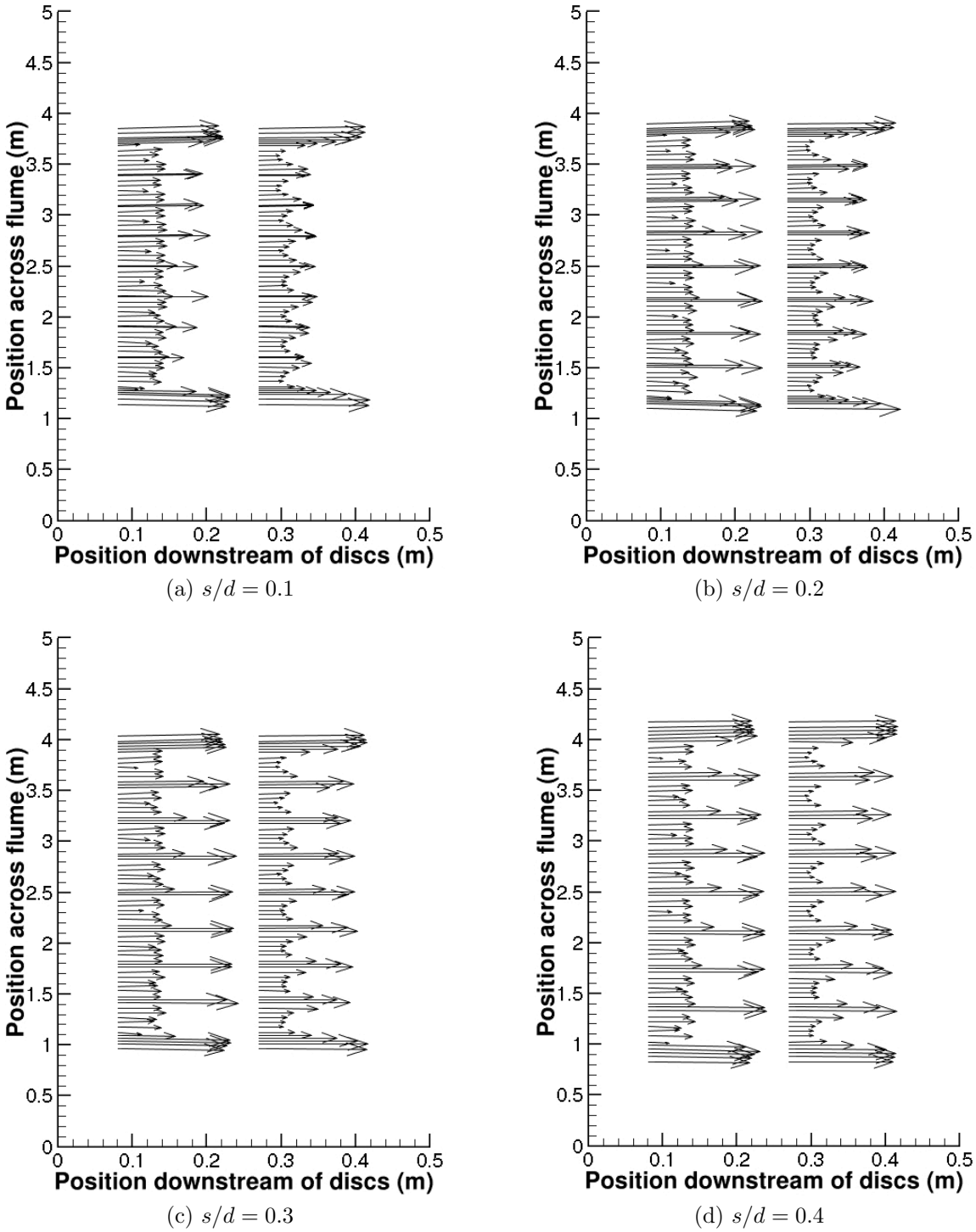

(a) $s/d = 0.1$

(b) $s/d = 0.2$

(c) $s/d = 0.3$

(d) $s/d = 0.4$

Figure 6.7: Flow speeds in the x-y plane at $0.3d$ and $1d$ downstream of arrays of $\Theta = 0.35$ discs, at different spacings. Measurements taken from the first set of tests. Flow speed vectors are scaled by 0.25, and are shown in m/s plotted against the x-axis (in m). Disc numbering is as shown in Figure 5.4

shear is visible in the wide spacing of $s/d = 0.4$. At $1d$ downstream, sheared bypass flow can be seen at all spacings, but with considerably stronger shear gradients on more closely spaced arrays.

6.3.1.1 Bypass Flow Lateral Behaviour

The effect of array wake expansion on individual device wakes is not clearly visible within these overall flow vector plots, however it can be observed more clearly by plotting U_y alone, or the U_y/U_x ratio. These results are plotted here to show different facets of the flowfield.

As the U_y values at individual measurement points are affected in disc wakes by the expansion or contraction of the disc wake as well as that of the overall array wake, the clearest indication of trends in the array wake can be seen by considering U_y values in the internal and external bypass positions only, as shown in Figure 6.8a. For these same points, the ratio of U_y/U_x can also be plotted, as in Figure 6.8b. All measurements shown are from the second set of tests, showing values from the $0.3d$ downstream traverse of each array, and measurement points behind discs (i.e. not in bypass flows) have been omitted for clarity. It should be noted that these plots will naturally be asymmetric as the sign of U_y will change at the centre of the array if the wake is expanding (or contracting) symmetrically. These plots allow expansion trends across all configurations to be generally compared.

It can be seen that across all array configurations there is expansion across the array wake, causing internal bypasses to divert away from the centreline of the array as the outer boundary of the array wake expands. However, it is of interest to note that there is a generally linear gradient of U_y, and of U_y/U_x, across all internal bypasses, while the near points in the outer bypasses show greater flow diversion with higher magnitudes of both. This once again shows end effects in action. The generally linear gradient across all inner bypass flows also shows that all internal disc wakes (apart

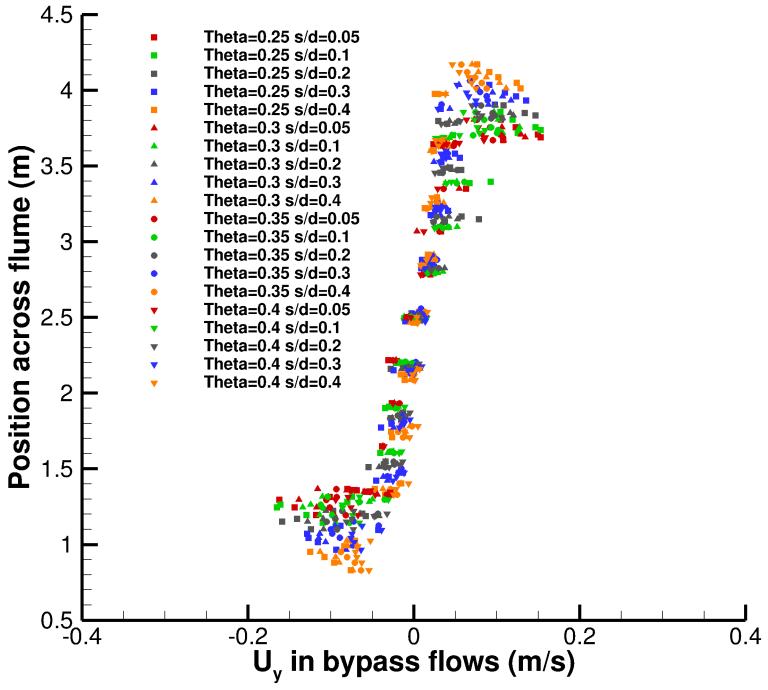

(a) U_y

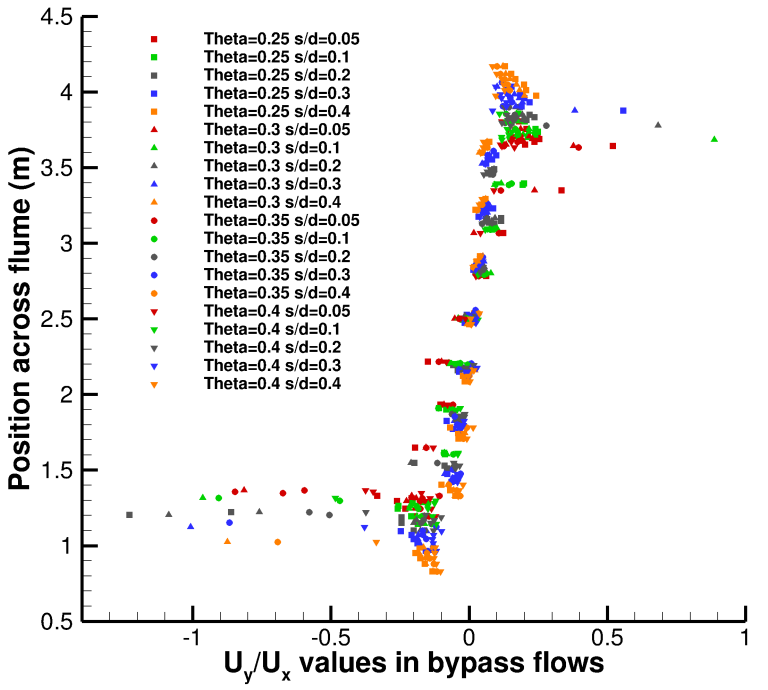

(b) U_y/U_x

Figure 6.8: Scatter plots showing the cross-stream velocity and the ratio of cross-stream to streamwise velocity in internal and external bypass flows, $0.3d$ downstream of all arrays.

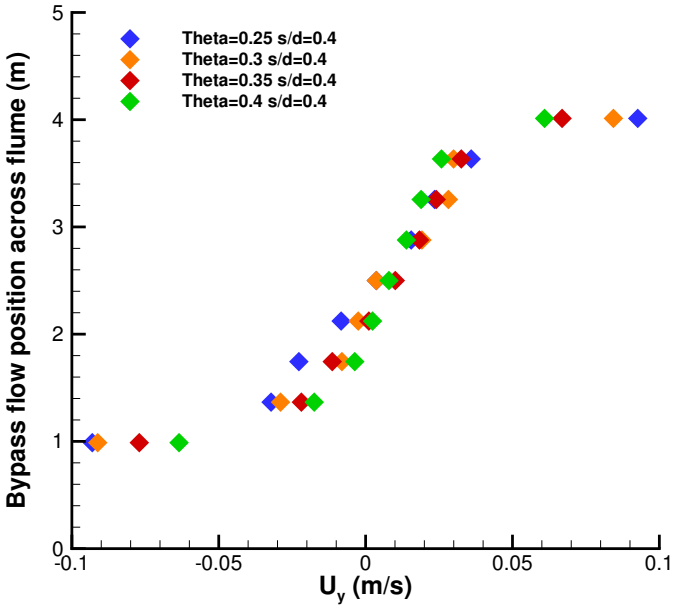

Figure 6.9: U_y velocities in the disc and array bypasses measured $0.3d$ downstream of all disc porosities at $s/d = 0.4$ spacing. (Note y positive upwards on y-axis, so flow on right hand side of flume, $y < 2.5$ m, is expected to have negative U_y.)

from those for discs 1 and 8) are expanding at approximately the same rate, as ΔU_y between the internal bypass wakes on each side of these disc wakes is the same. This is in line with the theoretical assumption that all individual device wakes can be treated as identical across a quasi-infinite array. However, where the quasi-infinite assumption breaks down at the ends of the array, the wakes of discs 1 and 8 can be seen to be expanding faster, with a greater ΔU_y between the inner bypass on one side of them and the outer bypass on the other.

Greater clarity can be achieved by restricting the number of configurations compared, and by averaging the U_y velocities in each internal and external bypass. Figure 6.9 shows such a comparison for the array spacing $s/d = 0.4$. It can clearly be seen that, the lower the array resistance is, the lower the gradient of U_y across the array's width. These arrays are all geometrically identical apart from the disc porosities, with the same number of discs in the same positions. Increasing the disc

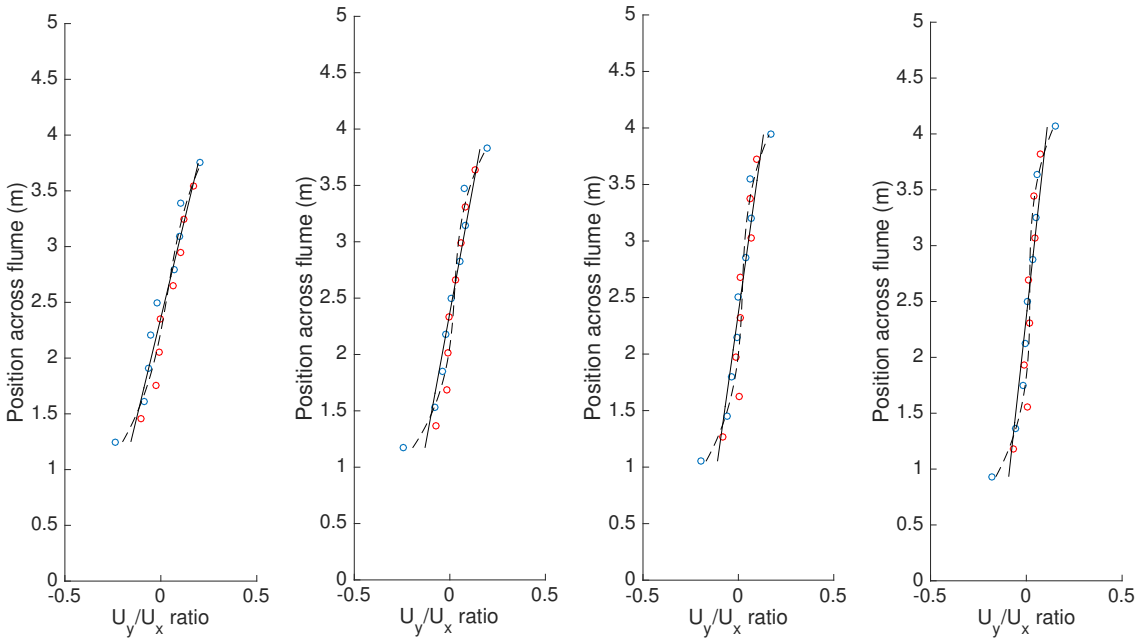

(a) $s/d = 0.1$ (b) $s/d = 0.2$ (c) $s/d = 0.3$ (d) $s/d = 0.4$

Figure 6.10: U_y/U_x at $0.3d$ downstream of $\Theta = 0.3$ discs at various spacings, with linear (solid) and cubic (dashed) regression fits. Disc average values are plotted in red, bypass averages in blue

resistance and thus the array thrust results in clear changes to the downstream wake expansion. It is also clear that U_y values are higher in the external bypasses than in the internal ones, meaning that the outer disc wakes are expanding more rapidly than the inner ones.

This partially contradicts the assumptions of the revised analytical model proposed by [88]. This model included device-scale wake expansion within the actuator disc model, to allow for the effects of such expansion within a short fence array. However, it was assumed that every device wake expanded at the same rate, with all sharing the same expansion factor at each downstream position. The experimental results show that, while this is broadly true across the central device wakes, it does not hold true in the case of the two end devices, whose wakes expand significantly more.

As an aside, Figure 6.8b shows outlying points in the external bypass flows on both sides of almost all arrays. With reference to the U_y plot in Figure 6.8a it is clear these are not instances of extreme flow diversion and high U_y, but rather sample volumes where for 60 s the average U_x value was relatively much lower than the average readings taken in these bypasses, such that $|U_y|$ could be equal to or even greater than $|U_x|$. There are far more of these outlying points, and they are more extreme, in the right-hand bypass (relative to flow direction) at the bottom edge of these plots. This gives further evidence of some asymmetry in the flow, as previously discussed in Section 5.3. This may be directly linked to the thrust asymmetry across discs, as shown in e.g. Figure 6.2, as these points could indicate flow approaching disc 8 at an angle, failing to pass directly through the holes parallel to the x-axis (as the discs are not perfect actuator discs and have a non-zero thickness), and being diverted tangential to the disc. This would increase disc thrust but not disc power (as shown in Figure 6.4). It is considered, therefore, that these outlying points - and in particular the imbalance of them between the two external bypasses - are an artefact of the basic flow conditions in the flume, and are not relevant to the general study of partial fence behaviour.

6.3.1.2 Disc Wake Lateral Behaviour

To study the entire array wake's expansion properties, including the flow behind individual discs, an averaging system for all points behind each disc is used to get a single overall U_y value for each disc wake. As discussed in Section 5.8, a weighted average scheme was considered the most robust option to average U_x values. This same method was also used for U_y values with the central point ignored and other measurements weighted by their appropriate disc area to reflect how much flow is moving in a certain direction. Having also taken an average of U_y in each internal and external bypass (with no weightings applied to these), the resulting bulk of U_y/U_x

				s/d		
Θ	$\kappa_{0.3d}$	**0.05**	**0.1**	**0.2**	**0.3**	**0.4**
0.25	≈ 10	0.2350	0.1463	0.1164	0.0769	0.0692
0.3	≈ 7	0.1885	0.1405	0.1085	0.0834	0.0642
0.35	≈ 5.5	0.1601	0.1344	0.0991	0.0819	0.0637
0.4	≈ 4	0.1239	0.1046	0.0815	0.0695	0.0581

Table 6.4: Gradient (per m across flume) of a linear regression fit to U_y/U_x values across the entire array, for all configurations. The highest value is highlighted in blue.

at $0.3d$ downstream can be analysed for every configuration. Examples of this are shown in Figure 6.10 for four configurations of the $\Theta = 0.3$ discs, together with linear and cubic fits (generated through Matlab's *polyfit* function). Broadly similar trends are seen to those discussed previously, confirming that the array wake is expanding self-similarly across its internal area, with the only significant variance from linearity at the ends of the array, where additional expansion is again seen to be present.

The wake expansion can be analysed as a function of overall thrust exerted by the array on the flow if it is plotted against κ and s/d, as was previously done for power and thrust coefficients. Figure 6.11 shows the coefficients of a linear U_y/U_x versus y fit, as provided in Table 6.4. It can be seen that the gradient of this expansion coefficient increases with both increasing κ and decreasing array width, as the thrust imposed on the flow by the array increases. This means that arrays designed to maximise power output through careful selection of local blockage and increased thrust will have increased wake expansion immediately downstream.

6.3.1.3 Downstream Behaviour

Following the study of wake expansion immediately behind the array, wake contraction can also be seen to occur very quickly downstream. This is almost certainly a function of the relatively high global blockage of the array within the flume - certainly higher than most proposed tidal turbine schemes at present. Figure 6.12 shows the

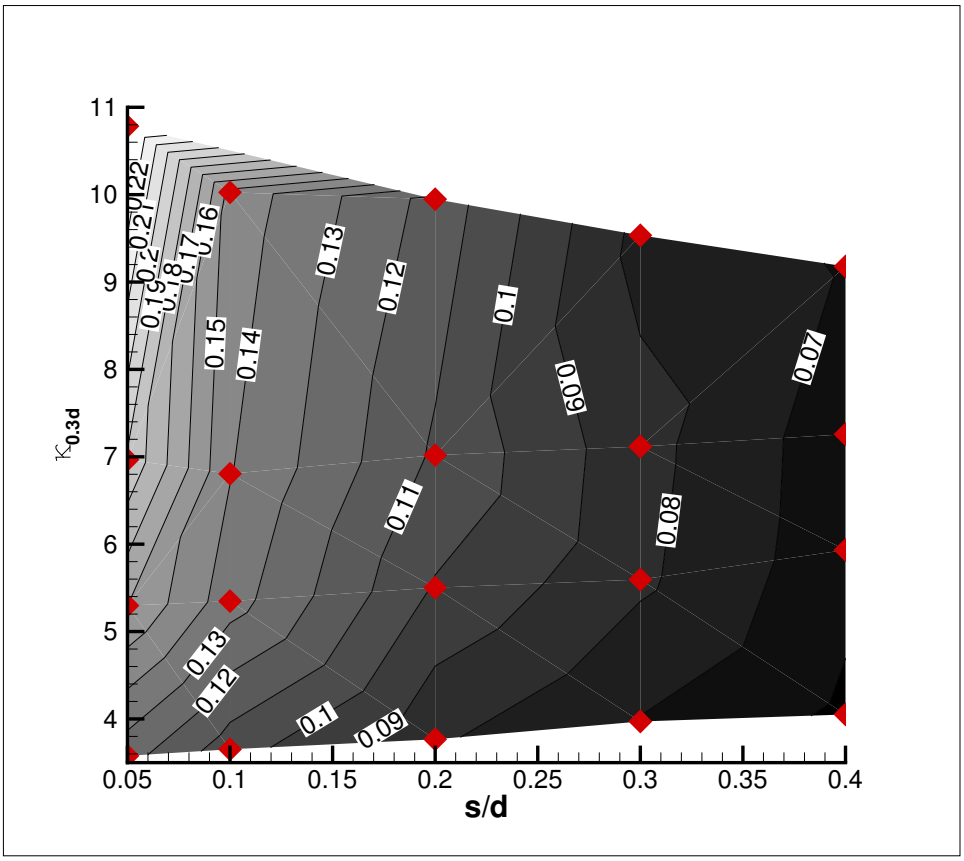

Figure 6.11: Coefficient of linear fit to U_y/U_x gradient across flume at $0.3d$ downstream of all arrays. Contours fitted to 20 individual experimental points, marked by red diamonds and detailed in Table 6.4.

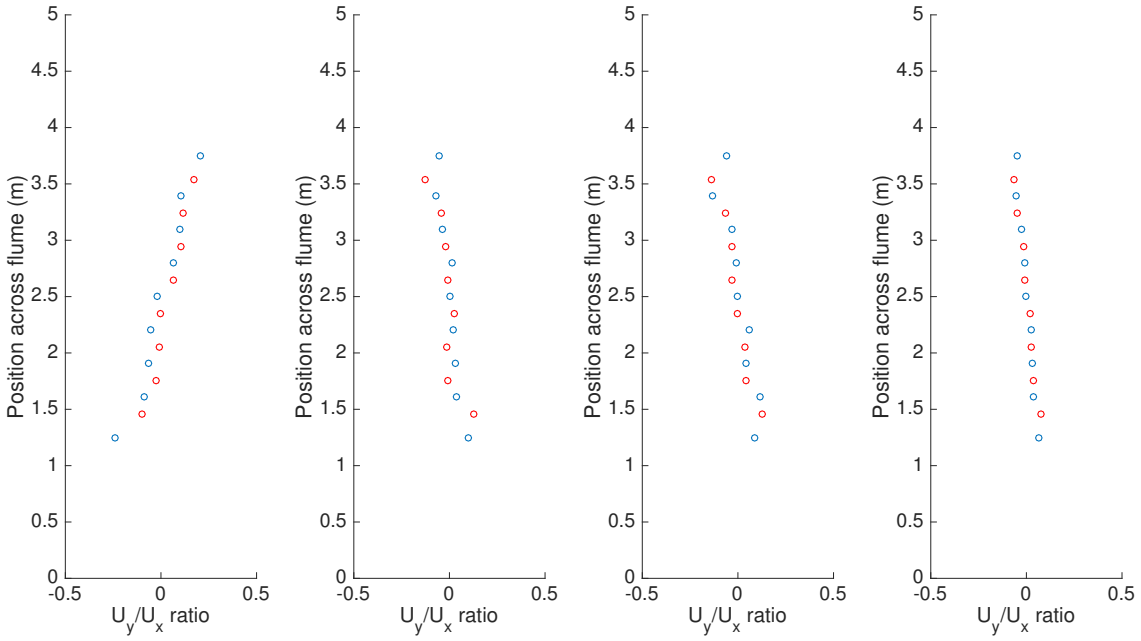

(a) $0.3d$ (b) $2d$ (c) $4d$ (d) $6d$

Figure 6.12: U_y/U_x at four downstream positions behind $\Theta = 0.3$ discs. Disc average values are plotted in red, bypass averages in blue.

progression of U_y/U_x downstream across four traverses, and it can be seen that even by two disc diameters downstream (i.e. less than a quarter of the array width) the entire wake has begun to contract, and continues doing so thereafter. Wake contraction is a direct consequence of the requirement, discussed in Section 3.2.1 for tidal turbines in incompressible flow, for velocity equalisation to occur downstream to ensure mass flux continuity. This contrasts the assumed continuous expansion of wind turbine wakes to achieve pressure equalisation.

Given the short distance over which this array wake is seen to expand prior to contraction, and comparing this to other studies of downstream wakes such as [115], who studied the wake of a single scale rotor in the same facility, it would seem that the high global blockage in this case has accelerated the process. Unfortunately the amount of data collected during this experimental work is insufficient to confirm this in more detail, since global blockage was not a parameter that changed across the

configurations investigated. Although this single set of downstream traverses was taken for this configuration, no additional downstream traverses were taken behind arrays with different local blockage in the same set of tests (the second set). However, an array wake showing contraction within two disc diameters downstream may well mean that tidal turbine arrays with high global blockage may benefit from fast wake contraction, which may enable any downstream rows of devices to be placed out of the wake of upstream rows.

6.3.2 Turbulence and Mixing

It is possible to analyse the flow measurements taken to explore the fluctuating components of fluid behaviour within the near wake. This involves investigation of Turbulence Kinetic Energy (TKE) and Reynolds Stresses. TKE is defined as:

$$\text{TKE} = \frac{1}{2}(\overline{u_x'^2} + \overline{u_y'^2} + \overline{u_z'^2}) \tag{6.1}$$

where an overbar denotes a time average and u_x', u_y' and u_z' denote the instantaneous fluctuating components of the u_x, u_y and u_z velocities. TKE is a measure of the kinetic energy contained within turbulent flow structures, which are created by sheared flow between the disc wakes and bypass flows, and as such it can be seen as a measure of the strength of all the mixing process occurring in each section of the flow. The TKE plots therefore display several features of the flow which might be expected from partial fence theory or from the thrust and power measurements presented in Sections 6.2.1 and 6.2.2.

An example of TKE distribution at $0.3d$ and $1d$ downstream is shown in Figure 6.13 for three different porosities at an identical spacing of $s/d = 0.2$. This figure relates to the first set of tests, where wake measurements were taken $1d$ downstream for this configuration.

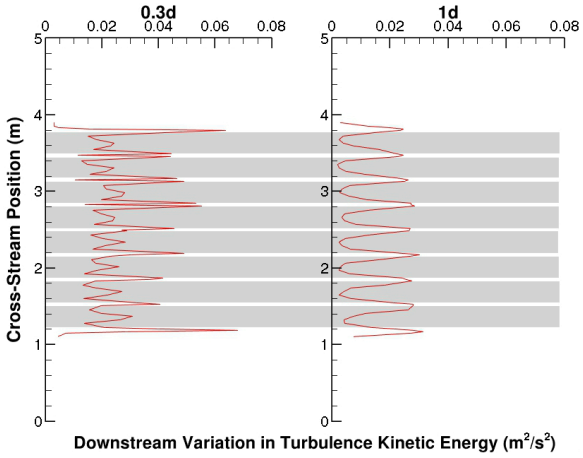

(a) $\Theta = 0.3$

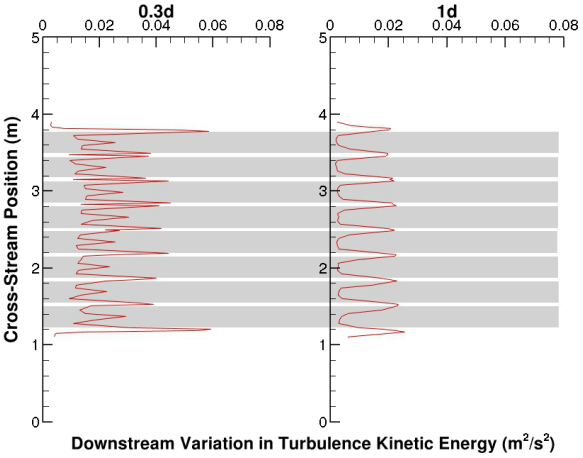

(b) $\Theta = 0.35$

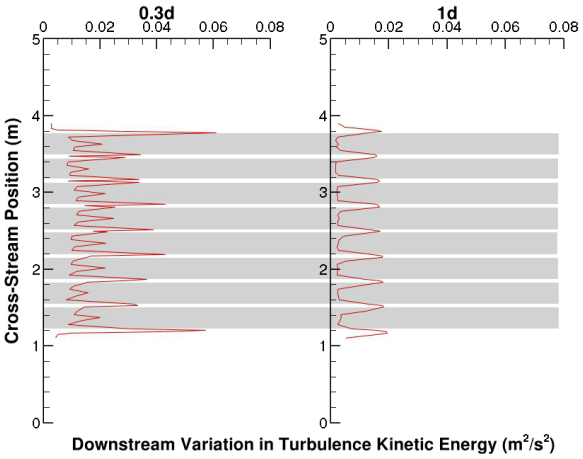

(c) $\Theta = 0.4$

Figure 6.13: Values of TKE at $0.3d$ and $1d$ downstream of arrays with $s/d = 0.2$ spacing, for three disc porosities. Measurements taken from the first set of tests. Grey bars show the projected downstream positions of the discs.

It can be seen that values of TKE in the array wake generally decrease with increasing disc porosity, as total array resistance to the flow decreases and thus lower shear and mixing are present downstream of the array. As with the flowfield and U_y plots, array wake expansion downstream of the array can also be seen for all configurations, as the peak of TKE in the external bypass flow moves outwards from the $0.3d$ measurement to the $1d$ measurements. This peak moves further than the internal bypass peaks, similar to the U_y plots, showing that external bypasses are expanding more than internal ones.

Distribution of TKE at $0.3d$ downstream for each array also shows differences between the flow around the central discs and the end discs in each array: in this case, values of TKE in inner bypass flows are seen to be significantly higher towards the middle of the array than they are towards the outer edges. This corresponds to lower thrust imposed on the flow by the outer discs in the previous investigation of thrust distribution across arrays. In addition, the values of TKE in the outer bypass flows are significantly higher than those in the inner bypass flows in all $0.3d$ plots. This distinction disappears by $1d$ downstream. Outer bypass mixing therefore initiates strongly behind the array concurrently with internal bypass mixing processes. This contradicts the assumption in analytical theory that a scale separation exists between device-scale mixing and array-scale mixing such that all device-scale mixing is complete before array-scale mixing commences.

It is also possible to examine the Reynolds stresses, being the average shear stresses on the fluid volume over the period of measurement. The Reynolds stress component between any two directions i and j is defined as $\tau_{ij} = -\rho\overline{u_i' u_j'}$. For systems with incompressible fluid, such as tidal turbines in water, this can be redefined per unit density as $\tau_{ij} = -\overline{u_i' u_j'}$ for simplicity. In the coordinate system adopted for the experiments, the most important fluid shear stress, when considering device wake interactions and partial fence theory, is the shear stress in the xy plane due to velocity

gradients between bypass flows and core flows across the array. These stresses will determine the rate of the quasi-two-dimensional mixing across the array wake. The Reynolds stress component for this mixing is thus:

$$\tau_{xy} = -\overline{u'_x u'_y} \tag{6.2}$$

The sign of this Reynolds stress will vary depending on the directionality of the shear: for example, it will be opposite on the two sides of a body in the flow, as the flow behind the body develops opposing vorticity caused by symmetric shear layers on either side. The -ve form of the equation reflects the convention of writing stresses +ve which cause movement in the +ve direction: see Massey [75] for a discussion and derivation.

For one high power configuration, that of $\Theta = 0.3$ discs with $s/d = 0.1$ spacing, additional downstream traverses were taken during the second set of tests, to give measurements at $0.3d$, $2d$, $4d$ and $6d$ downstream. Given the $8(s + d)$ width of the array, it was anticipated that even the $6d$ traverse would not be far enough downstream to observe complete mixing out of the array wake. However, the area upstream of array mixing being complete is still of interest when considering the assumptions of partial fence theory. Given that device and array mixing have both been seen to initiate immediately behind the array, it is particularly relevant to the question of assumed scale separation whether internal device wake mixing completes earlier than array wake mixing, or whether they proceed concurrently throughout the total length of the wake.

Measurements of the average U_x, τ_{xy} and TKE values are shown in Figures 6.14 - 6.16. General trends of wake development in a partial fence array can be observed in them. The $0.3d$ traverse shows a lot of chaotic mixing behaviour occurring immediately behind the discs: TKE values are high both within inner bypasses, where flow speed is high, and immediately behind the central tower, where U_x is close to

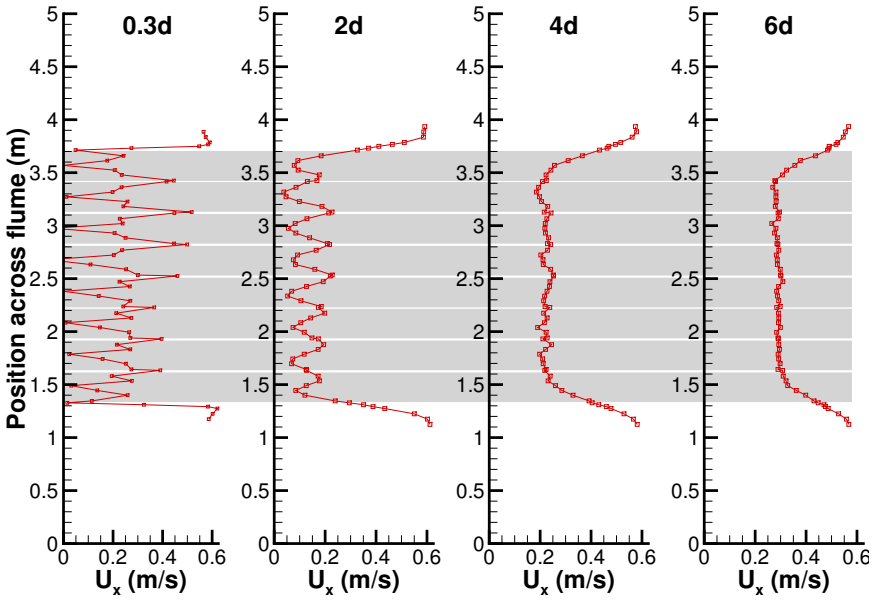

Figure 6.14: U_x values measured at four distances downstream behind a $\Theta = 0.3$, $s/d = 0.1$ array. Grey bars indicate upstream positions of discs.

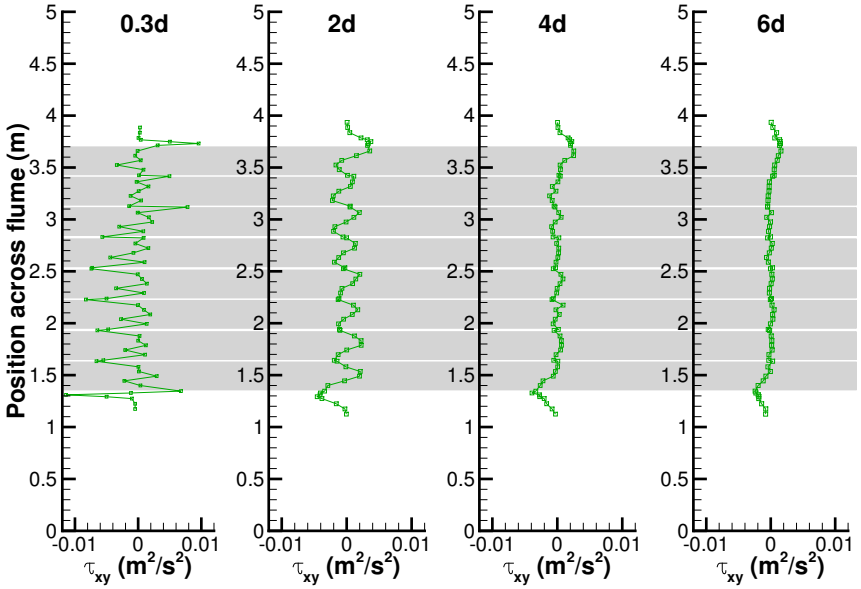

Figure 6.15: τ_{xy} values measured at four distances downstream behind a $\Theta = 0.3$, $s/d = 0.1$ array. Grey bars indicate upstream positions of discs.

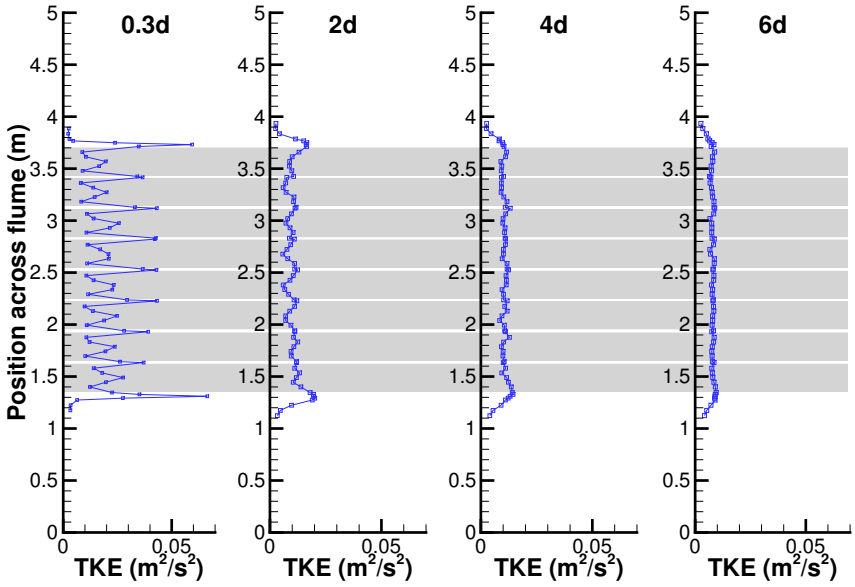

Figure 6.16: TKE values measured at four distances downstream behind a $\Theta = 0.3$, $s/d = 0.1$ array. Grey bars indicate upstream positions of discs.

zero. As shown with the $s/d = 0.2$ arrays in Figure 6.13, the highest TKE and $|\tau_{xy}|$ values occur immediately outside the outer discs of the array, in the outer bypasses. This shows that mixing processes are strongest in the outer bypasses, even at $0.3d$ downstream of the discs. This again strongly contradicts the theoretical assumption that device-scale mixing initiates first. At the $2d$ traverse, wake structures are coherent, with a clear internal wake deficit behind each disc and elevated τ_{xy} and TKE values in the internal bypass flows. It should be noted, however, that τ_{xy} and TKE values are still elevated in the external bypass flows above the values observed in the internal bypasses. This can be seen to continue further through the wake, where internal device wakes can be seen to mix out and only the external, array-scale mixing remains. By $4d$ and $6d$ downstream, there is a consistent U_x deficit across the entire array wake, and a consistent increase in TKE across the array wake, while $|\tau_{xy}|$ is close to zero across the main width of the array wake and only elevated at the edges where U_x shear in the x-y plane is still present. These measurements support the

other basic assumption of scale separation in partial fence theory; that mostly two-dimensional external mixing at the ends of the array persists further downstream than the three-dimensional internal mixing processes in, and between, the device wakes.

Further evidence of this can be seen by examining further downstream wake traverses measured across different arrays in the first set of tests. For three arrays, spanning the range of thrust imposed by arrays in this set of tests, an additional wake traverse was carried out at $5d$ downstream. This enables the evolution of the wake to be studied for each array, but also allows comparison between different arrays of the downstream wake evolution. U_x profiles for each of the three arrays ($\Theta = 0.3$ and $s/d = 0.1$, $\Theta = 0.35$ and $s/d = 0.3$, $\Theta = 0.4$ and $s/d = 0.4$) are shown in Figure 6.17a. General trends of mixing over the downstream wake are as seen before, with definite differences between internal and external bypass mixing scales. It is of interest to compare the $5d$ profile across the three arrays. The overall streamwise velocity deficit in the wake at this distance downstream behaves as might be expected, being less for the low thrust $\Theta = 0.4$, $s/d = 0.4$ array than for the higher thrust arrays. However, individual disc wake velocity profiles are still visible for this low thrust configuration, while for the high thrust $\Theta = 0.3$, $s/d = 0.1$ array these have completely disappeared by $5d$ downstream, leaving only a uniform velocity deficit across the entire array wake. This same trend can be seen in the τ_{xy} plot in Figure 6.17b, which shows the Reynolds stress values in the $x - y$ plane for the $5d$ traverse only, comparing all three arrays. It can be seen that, while the values of τ_{xy} in the external bypass flow are broadly similar across all three arrays here, the highest values in the internal bypass flows all belong to the $\Theta = 0.4$, $s/d = 0.4$ array. The average value of TKE across the array wakes at $5d$ downstream, as shown in Figure 6.17b, is very similar between all three arrays despite the differences in active internal mixing processes occurring.

These findings are relevant for practical applications of partial fence theory, par-

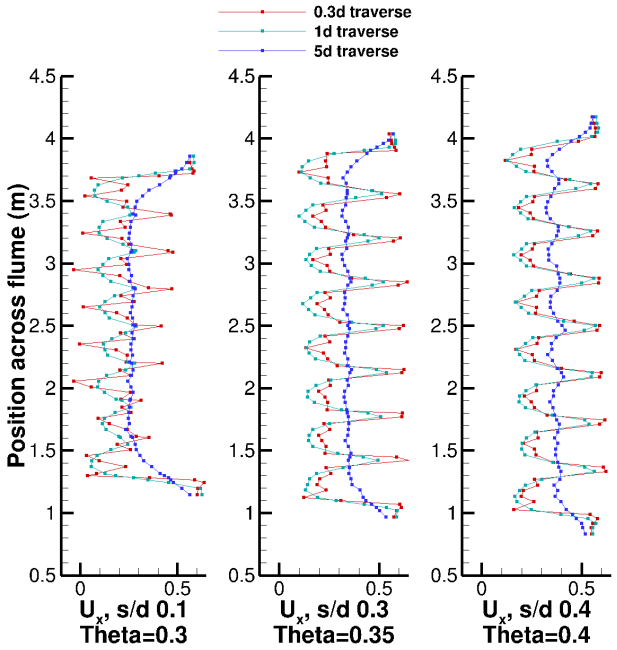

(a) U_x measurements for three arrays

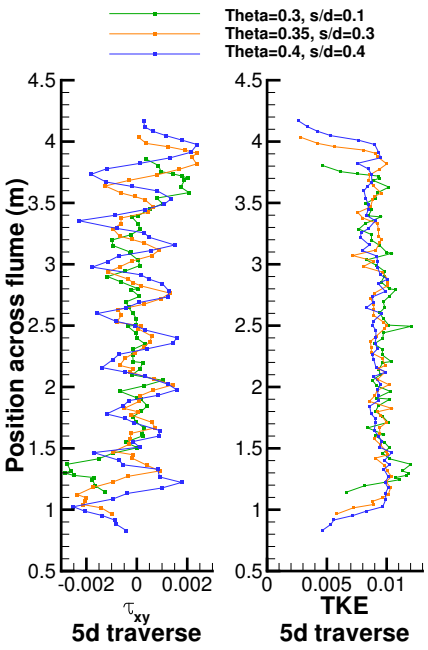

(b) 5D traverse measurements of τ_{xy} and TKE for three arrays

Figure 6.17: Values of U_x, τ_{xy} and TKE for three configurations, from first set of tests. U_x is shown for $0.3d$, $1d$ and $5d$ traverses downstream. τ_{xy} and TKE are shown for $5d$ traverse only.

ticularly in the case where multiple fence arrays are being considered, with some downstream of others. It might be expected that it would be better to place additional turbines downstream of arrays which have lower thrust and wider internal bypass flows, as these would be expected to have less overall effect on the channel flow. While such an array does have a lower downstream velocity deficit in the wake, and thus higher potential for further arrays downstream to generate power, turbulent structures within the wake are clearly also persisting further downstream for the wider, lower thrust array. It would be undesirable to place turbines in locations where high values of Reynolds stress still persist, as this will induce vorticity and increase fatigue loading on turbine blades. It has been seen that the inferred available power for the $\Theta = 0.3$, $s/d = 0.1$ array is 20% higher than that for the $\Theta = 0.4$, $s/d = 0.4$ array, for the same total frontal area of device. As such, the fact that the lower thrust array's internal wake mixing processes nevertheless continue further downstream may be very relevant to array design, particularly when combined with the earlier observation that high blockage appears to lead to accelerated wake contraction. Care must therefore be taken when placing turbines in a multiple-row partial fence arrangement, as it may be more efficient (in terms of available power versus build and maintenance costs) to use a smaller number of high thrust, low s/d arrays placed widely apart down a channel's length. A larger number of lower thrust, high s/d fences placed more closely downstream of each other, as often considered in the literature at present, may lead to higher maintenance costs through fatigue because of these wake mixing characteristics.

6.4 Sub-Array Investigation

The final element of the experimental work explored the 'sub-array' fence concept developed in Chapter 3. Both m and n (number of sub-arrays and number of devices in

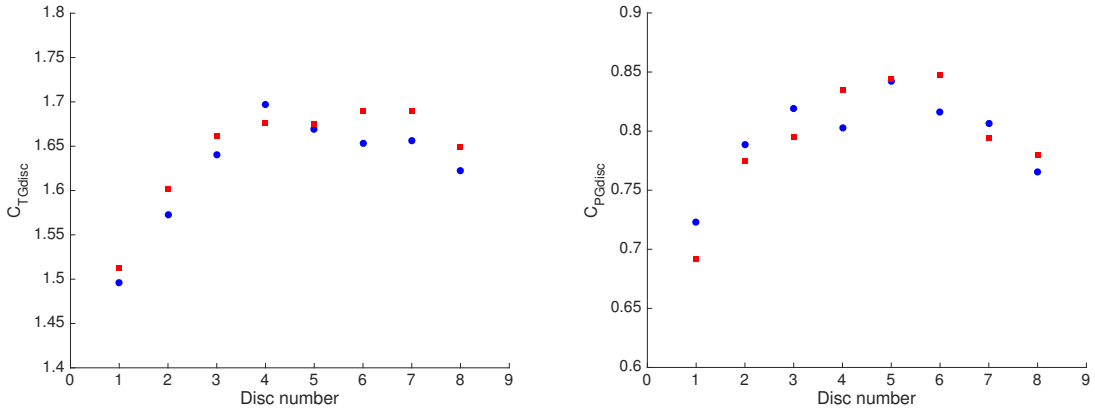

(a) $C_{TG\text{disc}}$ (b) $C_{PG\text{disc}}$

Figure 6.18: Values of $C_{TG\text{disc}}$ and $C_{PG\text{disc}}$ for $\Theta = 0.3$ discs with $s/d = 0.1$, in standard fence configuration (blue circles) and in 'sub-array' configuration with $0.2d$ central spacing (red squares).

each array) need to be reasonably large to justify some of the theoretical assumptions. It was considered likely to be difficult to explore this robustly within the experiment. Given that an n of 8 had been chosen for the single partial fence study, an equivalent use of $m = 8$ as well would require a 64-disc array, a minimum of 17.3 m wide using the existing discs. This was not feasible using the same equipment and facilities. However, it was possible to look at the case of two small sub-arrays of 4 discs each. As partial fence array effects were seen with only 5 discs in Chapter 4, it was believed that sub-arrays of 4 discs could also behave similarly.

One configuration tested previously for the single partial array experiments was retested with an increased gap between the central two discs, thus creating a larger internal bypass in the centre and splitting the array into two sub-arrays. The configuration chosen for this test was that of $\Theta = 0.3$, $s/d = 0.1$, a high thrust and power array, as sub-array theory showed additional gains to be made from the peak of partial fence theory. The spacing between the two sub-arrays was $0.2d$, twice the width of all other internal bypasses.

The global thrust coefficient, C_{TG}, of this array was found to be 1.6445, 1% higher

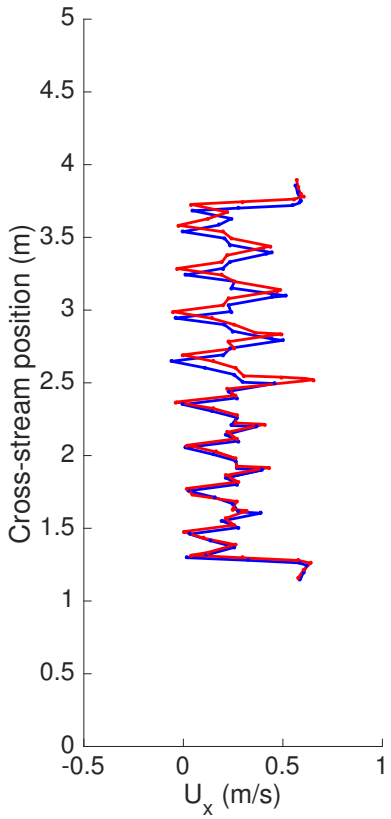

Figure 6.19: Values of U_x recorded downstream of a $\Theta = 0.3$ array with $s/d = 0.1$, in standard fence configuration (blue line and markers) and in 'sub-array' configuration with $0.2d$ central spacing (red line and markers).

than that of the continuous fence array's C_{TG} of 1.6260. Thrust was higher on seven out of eight discs in the sub-array case, as shown in Figure 6.18a. In the case of power, however, the sub-array case performed marginally worse, with $C_{PG} = 0.7951$ versus the continuous partial fence's $C_{PG} = 0.7954$. The per-disc plot shown in Figure 6.18b shows that there is no clear correlation of increased or decreased power across the discs. It is of interest that the power performance of the central discs does not drop off despite the bypass flow between them becoming wider.

Investigating the flow speed data shows very little discrepancy between the two cases, except at the central internal bypass. Figure 6.19 shows a comparison between U_x at $0.3d$ downstream for the two cases. The $0.2d$ wide central bypass shows an increased flow speed versus that recorded in the continuous case: this is presumably

due to an increased volume of flow resulting in a lower rate of deceleration through mixing with the slower disc flows downstream of the array.

The conclusion of this short investigation was that further experiments on sub-arrays, using this equipment, would likely be similarly inconclusive regarding potential power increases available. A different experimental set-up would be needed to enable greater numbers of longer sub-arrays to be investigated, before further information could be gained.

6.5 Conclusions

The objective of these experiments was to compare the predictions of analytical partial fence theory to the actual behaviour of a real fence array made up of 8 porous discs, tested within a wide flume to allow expected partial fence behaviour to develop. The findings from the experiments are threefold: firstly, that the total thrust and available power for the disc array were significantly less than predicted by partial fence theory; secondly, that the basic predicted trends of thrust and power as predicted by partial fence theory do exist, and that increased power is available with a carefully chosen combination of device thrust and array spacing; and thirdly, that the main differences between theory and reality are that a complete scale separation between device and array wake mixing does not occur in reality, and that end effects are significant in the performance of a real partial fence with a finite length.

The reasons for the differences between the theoretically predicted values of thrust and power and those observed experimentally cannot be completely proven, however it is considered likely due to several contributing factors. The necessity of measuring flow speed $0.3d$ downstream of the array instead of directly at the discs will reduce the values of 'inferred power' calculated relative to the actual power removed by the array. The choice of disc porosities made for this experimental work was based on

a first-order relationship between disc open area ratio and 'resistance factor'. This relationship is known to be somewhat unreliable across varying porous disc designs, and resulted in lower resistance discs being deployed than had been intended. General energy losses due to viscous effects, which are not accounted for within the quasi-inviscid analytical model, will also contribute to an inability to achieve the theoretical maximum. In addition to all of these, it has been seen that end effects play a role in reducing the ability of the total array to support high thrust and high power compared to the quasi-infinite fence assumptions of the theory, where each device is assumed to behave identically and suffer no impacts from end effects.

Given that this experiment was carried out with porous discs as turbine emulators rather than with real rotors, however, the total measured values of C_{TG} and C_{PG} are less relevant than for experiments modelling proposed real turbines: the main intention of these experiments was to show whether the overall trends of partial fence theory were correct, and whether greater power is available for closely-spaced, high thrust arrays when the spacing and thrust values are carefully chosen to exploit this. This was clearly shown to be true. Increases of up to 50% in thrust coefficient and 20% in inferred power coefficient were observed for a partial fence array of eight discs from the lowest resistance arrays to the highest. The arrays tested encompassed a parameter space of five values of inter-disc spacing and four values of disc porosity. The array with the highest power coefficient was not, however, the array with the highest thrust coefficient: the increase of 20% in power coefficient corresponded to an increase of 35% in thrust coefficient. Where it is possible, therefore, to design tidal turbines to withstand higher thrust and safely position them in very close spacings, there is significant potential to increase available power, even when considering the same device frontal area and total number of devices.

The analytical theory has been shown, however, to over-simplify the fluid flow around a short fence array such as this, and two corrections in particular ought to be

considered to make it more directly applicable to real array design in future. The first is to revisit the assumption of separation of scales between device mixing and array mixing. This is a key assumption within the theory to allow the scales to be decoupled. However, it has been shown to be only partially true in the experiments: while array-scale wake mixing is always seen to persist further downstream than device-scale wake mixing, it is not seen to initiate later than that of device scale. In fact, the array wake mixing processes in the outer bypass flows are seen to initiate more strongly immediately behind the array than for the device wake mixing. This assumption should therefore be revisited, though correcting it may complicate the simple model to the point where it can no longer be solved. The second correction would be to include the impact of end effects and device wake expansion in a short fence within the analytical model. This has already been partially attempted analytically [88], but unfortunately the wake expansion factors developed are not related to the geometry or design of an array and thus cannot be measured with certainty for any real array to substitute into the model. In addition, there is no allowance for end effects within this model. As such, a model of array behaviour needs to be developed which includes end effects and can incorporate experimental data to produce amended thrust and power predictions.

Chapter 7

Analytical Partial Array Model with Variable Device Behaviour

The experimental work discussed in Chapter 6 showed significant variation in the distribution of both thrust and inferred power coefficients across all partial fence arrays tested. The highest thrust arrays in particular showed a strongly curved distribution of power coefficient, C_{PG}, with significantly less power extraction at the ends of the arrays. Similar behaviour has been seen in computational modelling such as that carried out by Hunter [55]. However, there is presently no analytical model which will allow these end effects to be included in simple array modelling. Such a model would allow better prediction of array performance for a row array in a tidal channel, and would enable developers to include these effects at design stage.

This chapter discusses end effects as witnessed in the experimental work. A number of potential methods to model these end effects within an analytical framework are investigated. A simple model which allows thrust, power and flow variations across an array and attempts to partially account for end effects is presented.

7.1 Investigation of End Effects for Short Fence Arrays

Thrust and inferred power were seen to vary across an eight-disc array during the experiments. These effects are of significant interest to designers and developers as they affect the build requirements and expected performance of devices in arrays, however they are not entirely self-explanatory. To understand the reasons for these end effects, and to include them in any form of modelling, the basis of this behaviour must be understood.

It is therefore of interest to study other quantities that varied across the array during experimental testing. This includes a) the flow speeds measured immediately behind the disc, since inferred power was calculated from disc thrust multiplied by these flow speeds and b) the measured disc pressure coefficient, $\kappa_{0.3d}$. Although this pressure coefficient might be thought to be an intrinsic property of a disc in any configuration, the experimental data collected and discussed in Section 6.1.1 suggest otherwise. The average $\kappa_{0.3d}$ across each array was shown to vary in a complex fashion with array spacing: the highest resistance discs displayed a consistently decreasing $\kappa_{0.3d}$ with increasing s/d, while the lowest resistance discs exhibited the opposite behaviour. While $\kappa_{0.3d}$ is calculated from $U_{\text{disc},0.3d}$, which does not necessarily vary linearly with U_{disc} (as discussed in Section 5.8), this is insufficient to explain the $\kappa_{0.3d}$ variation.

Breaking the results down further to investigate the $\kappa_{0.3d}$ values per disc gives insight into the array behaviour. An example is shown in Figure 7.1a for the closest and widest spacings of $\Theta = 0.4$ discs. This disc resistance was chosen for investigation due to having a relatively smooth κ variation across the array at both low and high s/d, making model comparison easier. It can be seen that the average disc pressure coefficient is higher for the more widely spaced array in this case. However, it can

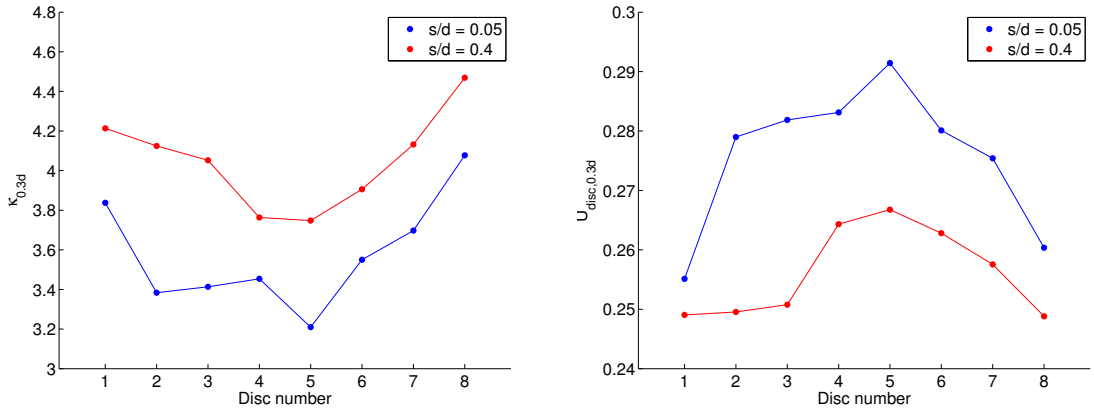

(a) $\kappa_{0.3d}$ (b) $U_{0.3d}$

Figure 7.1: Values of flow speed and disc pressure coefficient, respectively measured and calculated at $0.3d$ downstream of individual discs, for the $\Theta = 0.4$ discs at closest and widest spacings. Disc numbering is as defined in Figure 5.4.

also be seen that there is reasonably significant variation in the individual disc measurements of $\kappa_{0.3d}$ across the array, circa 10% from average, with the highest values occurring towards the edges and the lowest towards the centre. The reason behind this variation is not clear, but it is thought that it may be due to the variation of disc wake mixing behaviour with blockage and with other downstream mixing (such as the outer array mixing processes).

The variation of the area-weighted $U_{0.3d}$ values across these same arrays are also shown in Figure 7.1b, and can be seen to vary approximately inversely to $\kappa_{0.3d}$ as might be expected. When considered within the behaviour of the wider array, however, this distribution of flow speed is non-intuitive: one might expect the core flow through the discs to be more retarded in the centre of the array, and to have higher velocity towards the edges, as would be the case with the wake of a single device. However, the opposite behaviour appears to be occurring: core flow through the outer discs is slower than that through the central ones. As with the $\kappa_{0.3d}$ variation, this is likely to be a function of the effective resistance of each disc and of the wake mixing events occurring downstream of them. Without more detailed wake measurements along the length of the wake, however, it is not possible to identify which mixing effects are

causing this, nor exactly how. However, the ability to vary κ and U_{disc} across the array, whether individually or together, would clearly be useful within an analytical model aiming to reproduce these effects.

When designing such a model, it is necessary to evaluate the possible ways in which such a correction could be applied. In particular, it is of interest whether both κ and U_{disc} values (used in analytical modelling instead of the experimentally measured $\kappa_{0.3d}$ and $U_{0.3d}$ values) can be independently varied. It is not clear from the experimental results whether there is only one process at work causing both increase in κ and decrease in U_{disc} at the ends of each array. Therefore, a model would ideally allow the ability to vary both quantities quasi-independently (given that varying κ alone will also alter U_{disc} values).

Note that, since the $U_{0.3d}$ measurements were based on only 5 measurement points per disc, taken only at mid-depth, and since the experimental work focused only on 8 turbines in a specific cross-sectional area with a single value of global blockage, there is limited parametric information with which to develop the model. This is particularly important where empirical correction may be required. Further experiments or computational work would usefully add to this knowledge base.

7.2 Revised Analytical Model with End Effects

Returning to Linear Momentum Actuator Disc Theory (LMADT) as used in Chapter 3, a new model can be developed which allows a variation of κ across an array of actuator discs to be used as an input. This results in an output variation of flowspeed, thrust coefficient and power coefficient across the array.

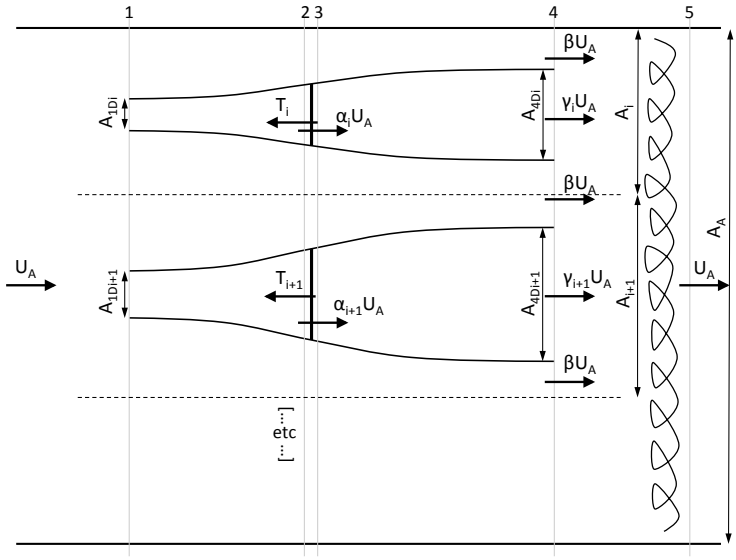

Figure 7.2: Model diagram for the multiple streamtube model, showing the single bypass flow speed at position 4. The ith and (i+1)th channels are shown in detail within an n-channel array.

7.2.1 Local Array Model

As shown in Figure 7.2, the model for the array itself consists of a finite specified number n of actuator discs, all experiencing a constant approach flow speed U_A. The ith disc imposes a thrust T_i upon the core flow which passes through it. Each disc and disc wake has local induction factors, α_i and γ_i respectively, specific to the ith channel. However, the bypass flow is considered to be homogeneous across the array, and thus at station 4 (static pressure equalisation across the array) the bypass flow speed is βU_A around all device streamtubes. This assumption is equivalent to that made in standard BEM theory for a single rotor, where only one bypass flow is included around the edges of the rotor and all blade element streamtubes are assumed to share the same bypass flowspeed at the static pressure equalisation point. The bypass flow data from experiment is inconclusive as to whether this assumption is justified, since no measurements were taken at the static pressure equalisation point within the device wakes. However, internal bypass flow speeds were broadly similar at $0.3d$ and further downstream, as shown for example in Figure 6.14.

Since LMADT models are one-dimensional, and contain no information about the cross-stream position of core or bypass flows, this model is equivalent to that shown in Figure 7.3a (where the similarity to a BEM model can be more clearly seen). Since the total thrust of all actuator discs can be summed to equal the thrust of the array, we can also choose to represent this by a single aggregated streamtube model as shown in Figure 7.3b. The subscript S is used for quantities specific to this version of the model. This single streamtube formulation can be used to find a relationship between the thrust coefficient and the bypass induction factor β, which can then be used to solve the multiple streamtube problem. By reducing the model to a single streamtube in order to do this, an assumption is made regarding the equivalence of momentum flux between the single streamtube and multiple streamtube forms. This assumption is that the average of the squared disc wake velocities at position 4, $\frac{1}{n}\sum_{i=1}^{n} U_{4Di}^2$, can be considered equal to the square of the average disc wake velocity, $\overline{U_{4D}}^2 = (\frac{1}{n}\sum_{i=1}^{n} U_{4Di})^2$. This assumption is justifiable provided the variation in U_{4D} is not too great across the array, and it is equivalent to the assumption made in the blockage-corrected BEM method developed by Vogel [130] that U_{4D} is calculated as the average wake velocity across the rotor plane.

The governing equations for a single streamtube LMADT model are, as previously discussed in Chapter 3, those of conservation of mass:

$$U_A A_{1DS} = \alpha_S U_A A_{2DS} = \gamma_S U_A A_{4DS} \tag{7.1}$$

$$U_A A_A = \beta U_A (A_A - A_{4DS}) + \gamma_S U_A A_{4DS} \tag{7.2}$$

conservation of momentum:

$$T_S = (p_2 - p_3) A_{2DS} \tag{7.3}$$

$$T_S = (p_1 - p_4) A_A + \rho A_A U_A^2 - \rho (A_A - A_{4DS}) \beta^2 U_A^2 - \rho A_{4DS} \gamma_S^2 U_A^2 \tag{7.4}$$

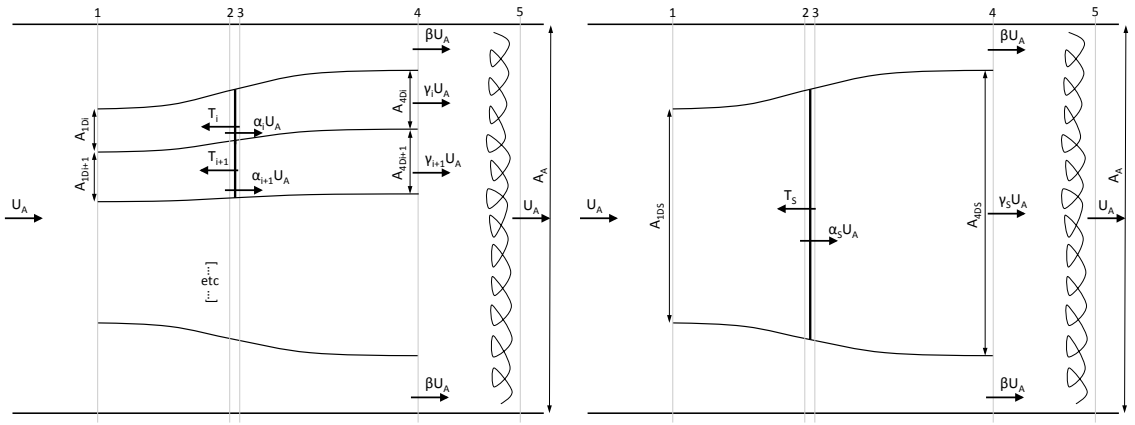

(a) Combined streamtubes (b) Single streamtube

Figure 7.3: Model diagrams for: a) an equivalent multiple streamtube model showing the similarities to a standard concentric annulae BEM analysis; b) a representative single streamtube which can be used to evaluate the array effects on the bypass flow.

and conservation of energy, or Bernoulli's equation:

$$p_1 + \frac{1}{2}\rho U_A^2 = p_2 + \frac{1}{2}\rho\alpha_S^2 U_A^2 \tag{7.5}$$

$$p_3 + \frac{1}{2}\rho\alpha_S^2 U_A^2 = p_4 + \frac{1}{2}\rho\gamma_S^2 U_A^2 \tag{7.6}$$

$$p_1 + \frac{1}{2}\rho U_A^2 = p_4 + \frac{1}{2}\rho\beta^2 U_A^2 \tag{7.7}$$

Combination of equations (7.1) and (7.2) yields a geometric relationship between the three induction factors in terms of the local blockage ratio, B_L (the ratio of total disc area to array channel area):

$$\beta = \frac{1 - \alpha_S B_L}{1 - \frac{\alpha_S}{\gamma_S} B_L} \tag{7.8}$$

Combination of the Bernoulli equations with the momentum equations (7.3) and (7.4) yields:

$$T_S = \frac{1}{2}\rho U_A^2 A_{2DS}(\beta^2 - \gamma_S^2) \tag{7.9}$$

$$T_S = \frac{1}{2}\rho U_A^2 A_{4DS}(\beta - \gamma_S)(\beta + 2\gamma_S - 1) \tag{7.10}$$

and setting these two equations equal to each other, noting that $A_{2DS} = \frac{\gamma_S}{\alpha_S} A_{4DS}$ from equation (7.1), yields:

$$\alpha_S = \frac{\gamma_S(\beta + \gamma_S)}{\beta + 2\gamma_S - 1} \tag{7.11}$$

Noting that equations (7.8) and (7.11) are both in terms of α_S, γ_S and β, they can be combined to eliminate α_S and yield a quadratic expression for γ_S in terms of β and B_L:

$$\gamma_S = \frac{-(\beta - 1) \pm \sqrt{(1 - B_L)(\beta - 1)^2 + B_L^2\beta^2}}{B_L} \tag{7.12}$$

of which the correct root for a turbine is the positive one. A thrust coefficient for the single streamtube is now defined as:

$$C_{TS} = \frac{T_S}{\frac{1}{2}\rho A_{2DS} U_A^2} \tag{7.13}$$

where A_{2DS} is the area of the effective device in the single streamtube formulation, which is equal to the sum of the device areas across all the individual streamtubes, nA_{2Di}. (Within this model, all devices are assumed to have the same cross-sectional area.) The single streamtube thrust, T_S, is similarly the sum of the thrust across all streamtubes, $\sum_{i=1}^{n} T_i$.

The positive root of equation (7.12) can now be substituted back into equation (7.9) to eliminate γ_S and eventually yield a quartic expression for β in terms of the local blockage ratio and the single streamtube thrust coefficient C_{TS}:

$$-3\beta^4 + 4\beta^3 + 2((2 - B_L)C_{TS} + 1)\beta^2 - 4((2 - B_L)C_{TS} + 1)\beta + (1 - B_L C_{TS})^2 + 4C_{TS} = 0 \tag{7.14}$$

Only one of the roots of equation (7.14) is greater than 1 and non-complex for turbine-appropriate values of B_L and C_{TS}. Therefore it is possible, using this equa-

tion, to find β from a specified C_{TS}.

Since the thrust to be imposed in the single streamtube formulation is equal to the total thrust on all devices in the multiple streamtube formulation, the governing equations for the ith streamtube must now also be established. Taking this streamtube (including a local area of bypass flow) to have cross-sectional area A_i as indicated in Figure 7.2, the governing equations of conservation of mass, momentum and energy for this streamtube become:

$$U_A A_{1Di} = \alpha_i U_A A_{2Di} = \gamma_i U_A A_{4Di} \tag{7.15}$$

$$U_A A_i = \beta U_A (A_i - A_{4Di}) + \gamma_i U_A A_{4Di} \tag{7.16}$$

$$T_i = (p_{2i} - p_{3i}) A_{2Di} \tag{7.17}$$

$$T_i = (p_1 - p_4) A_i + \rho A_i U_A^2 - \rho (A_i - A_{4Di}) \beta^2 U_A^2 - \rho A_{4Di} \gamma_i^2 U_A^2 \tag{7.18}$$

$$p_1 + \frac{1}{2}\rho U_A^2 = p_{2i} + \frac{1}{2}\rho \alpha_i^2 U_A^2 \tag{7.19}$$

$$p_{3i} + \frac{1}{2}\rho \alpha_i^2 U_A^2 = p_4 + \frac{1}{2}\rho \gamma_i^2 U_A^2 \tag{7.20}$$

$$p_1 + \frac{1}{2}\rho U_A^2 = p_4 + \frac{1}{2}\rho \beta^2 U_A^2 \tag{7.21}$$

It should be noted that A_i for each channel is unknown, as it is a function of the thrust imposed in each channel and varies accordingly such that the bypass flow speed is equal across all streamtubes. Therefore, it is not possible to close these equations completely as was done for the single streamtube model, as the effective local blockage of each individual streamtube is unknown. However, it is possible to combine equations (7.15)-(7.21) as before to yield the following two device relationships for each streamtube:

$$C_{Ti} = (\beta^2 - \gamma_i^2) \tag{7.22}$$

$$\alpha_i = \frac{\gamma_i(\beta + \gamma_i)}{\beta + 2\gamma_i - 1} \tag{7.23}$$

7.2.1.1 Substitution of experimental values and iterative solution

To proceed further, additional information is required, since the distribution of C_{Ti} across the array is unknown. Data from the experimental campaign is used to allow the model to be closed.

The variation in C_{Ti} across the discretised channels is found from the relationship between thrust coefficient and the disc resistance coefficient in each channel, κ_i, defined as:

$$\kappa_i = \frac{\Delta p}{\frac{1}{2}\rho U_{2Di}^2} \tag{7.24}$$

which, since C_{Ti} is defined as:

$$C_{Ti} = \frac{T_i}{\frac{1}{2}\rho U_A^2 A_{2Di}} \tag{7.25}$$

results in:

$$C_{Ti} = \kappa_i \alpha_i^2 \tag{7.26}$$

and thus a prescribed distribution of κ_i will translate into a distribution of C_{Ti} once α_i is known.

Since $T_S = \sum_{i=1}^{n} T_i$, $C_{TS} = 1/n \sum_{i=1}^{n} C_{Ti}$. Therefore, an iterative solution method can be adopted, wherein the problem is first solved in the single streamtube formulation for an initialising value of β. From this, a value of α_S is generated which can be used as an initial value for all α_i. Using a prescribed distribution of κ_i, an initial distribution of C_{Ti} is calculated. From this, the initial C_{TS} is found and β is recalculated from equation (7.14). An iterative loop then commences wherein the following steps are performed:

1. γ_i is calculated from equation (7.22).

2. α_i is calculated from (7.23).

3. C_{Ti} is calculated from equation (7.26).

4. β is recalculated from equation (7.14).

5. γ_i is recalculated as per step 1.

A low relaxation factor is applied to the recalculation of γ_i on each loop to aid solution convergence. Convergence is sufficiently quick that this makes no noticeably significant difference to calculation time.

This produces a fully closed solution for the inner model of the device streamtubes, so long as a distribution of κ_i is provided. This is, once again, analogous to a BEM rotor model where lift and drag coefficients of each blade section must be provided.

7.2.2 Channel Envelope for Partial Array Formulation

The model as previously described can only predict the behaviour of an array of devices homogeneously spaced across a channel, sharing the same local blockage. In order to preserve the partial array behaviour observed when grouping devices more closely together within a wide channel, an outer LMADT model at array-scale is required, as shown in Figure 7.4. This follows the method of Nishino & Willden [87] as previously described in Section 3.2.2. Conservation of mass between the outer and inner scales is ensured by continuity of U_A between the channel scale and the multiple streamtube scale, and the total thrust is matched between the two scales. Given that a total value of thrust coefficient for the array is produced by the inner model, this fixes the thrust in the array-scale model and allows solution of the outer scale. This is done in exactly the same way as carried out in Chapter 3, calculating the array

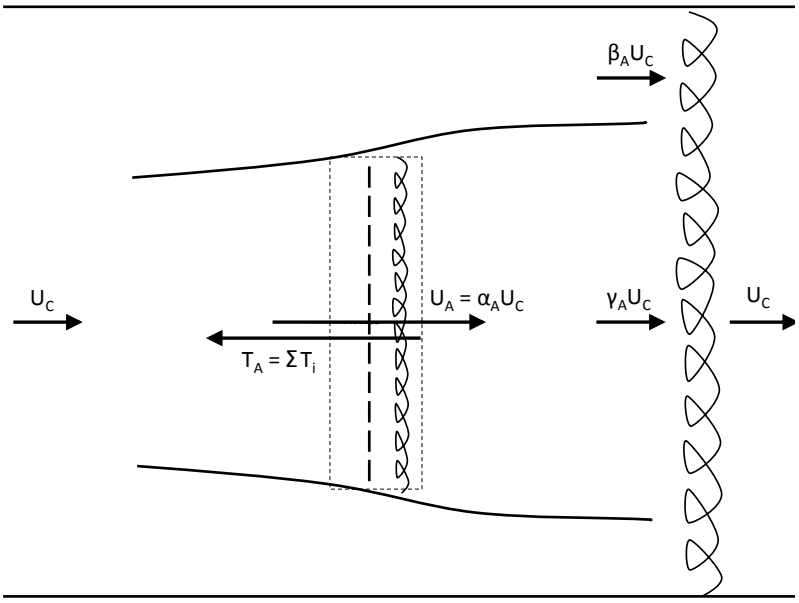

Figure 7.4: Illustration of the discretised array model within a channel envelope to form a partial array model. Area shown within the dashed rectangle is the discretised model previously described in Section 7.2.1.

wake induction factor, γ_A, as:

$$\gamma_A = 1 - \frac{(\alpha_A^2 B_L C_{TS})(1 - \frac{\alpha_A}{\gamma_A} B_A)^2}{(1 + \gamma_A - 2B_A \alpha_A)} \tag{7.27}$$

which can be solved iteratively if an initial guess for α_A is made. Once γ_A is found, α_A can be calculated from:

$$\alpha_A = \frac{1 + \gamma_A}{(1 + B_A) + \sqrt{(1 - B_A)^2 + B_A(1 - 1/\gamma_A)^2}} \tag{7.28}$$

and all other unknowns can then be found. This provides a closed model with a 'partial array' scale separation and a discretised array model allowing variation in local streamtube behaviour for each device, where all device resistance coefficients are specified.

7.3 Results of Revised Model

Since the motivation behind the development of this model was the observed variation in κ, C_{TG} and C_{PG} in the experimental work, it is of interest to compare the results of the model to experimental data, where possible. The values of κ and α could not be measured directly during experiments, due to the difficulties of bringing the ADV probe close to the disc plane. However, it is possible to substitute the experimentally measured $\kappa_{0.3d}$ values into the revised model as κ values and compare the output to experimental measurements (particularly since $U_{\text{disc},0.3d}$ and C_{PG} are also affected by this restriction, and will be accordingly lower than their true values).

In order to do this, it makes sense to first remove some variability and asymmetry in κ variation across the array by creating a symmetric $\kappa_{0.3d}$ profile as input to the model. This can be done by averaging $\kappa_{0.3d}$ by disc position relative to the centre of the array (i.e. averaging Disc 1 and Disc 8 to obtain an average 'outermost disc' value, etc). The result of this process applied to the data previously given in Figure 7.1a is shown in Figure 7.5, with the corresponding values of $\kappa_{0.3d}$ detailed in Table 7.1.

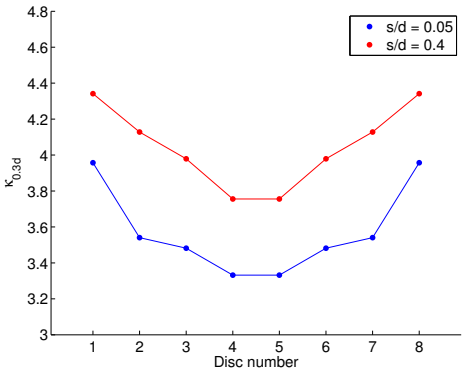

Figure 7.5: Symmetric distribution of $\kappa_{0.3d}$ for two $\Theta = 0.4$ arrays

	$\kappa_{0.3d}$			
s/d	Discs 1,8	Discs 2,7	Discs 3,6	Discs 4,5
0.05	3.9573	3.5403	3.4816	3.3317
0.4	4.3413	4.1283	3.9790	3.7557

Table 7.1: Averaged values of $\kappa_{0.3d}$

Using these values of κ within the discretised array model, and adjusting the value of local blockage according to both arrays' s/d values, distributions of U_{disc}, $C_{TG\text{disc}}$ and $C_{PG\text{disc}}$ are obtained. These results are shown in Figures 7.6 and 7.7.

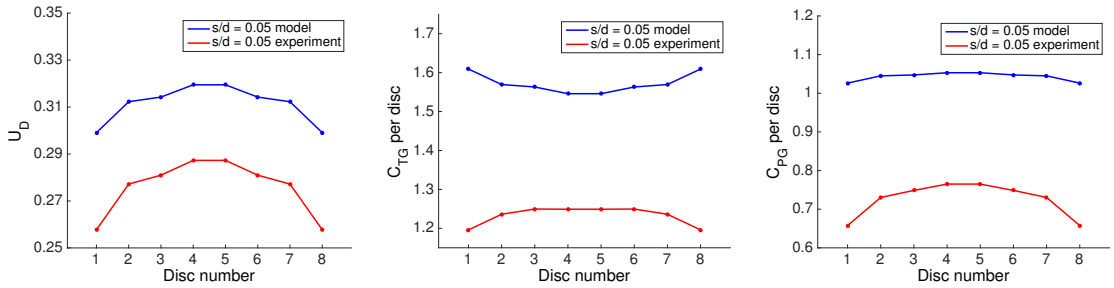

(a) U_{disc} (b) $C_{TG\text{disc}}$ (c) $C_{PG\text{disc}}$

Figure 7.6: Distributions of flow speed, thrust and power coefficients across all discs in a revised array model simulation of a $\Theta = 0.4, s/d = 0.05$ array, with κ distribution input taken from experimental measurements. The experimental record of each measurement for this array, averaged to remove asymmetry, is also shown for comparison.

Comparing these results with those measured in experiments allows some conclusions to be made about the new model. Comparing the U_{disc} values generated by the model to the measured values of $U_{0.3d}$ as shown in Figure 7.1b, it is clear that the overall shape of the U_{disc} distribution is being reproduced correctly: discs with higher κ values are experiencing lower flow speed, as would be expected. The predicted velocities are also of the correct order, however the magnitude of U_{disc} is seen to be higher in the model's predictions than the measured values. It should be noted that U_{disc} from the model and $U_{0.3d}$ from experiments are not directly comparable, since one is a value in the disc plane (albeit calculated using $\kappa_{0.3d}$) and one is a downstream measurement. It is therefore not helpful to compare them directly in terms of magnitude. However, an additional difference can also be seen in the experimental measurements for the higher thrust, closer spacing array ($s/d = 0.05$): there is a larger drop-off in flowspeed at the edges of the array than is predicted by the model.

The probable over-prediction of flowspeed leads to an over-prediction of power coefficient. C_{PG} per disc again exceeds the measured values of inferred power coefficient, this time by a greater margin. However, an 'end effect' causing reduction of the power coefficient towards the edges of the array is clearly visible, as was desired,

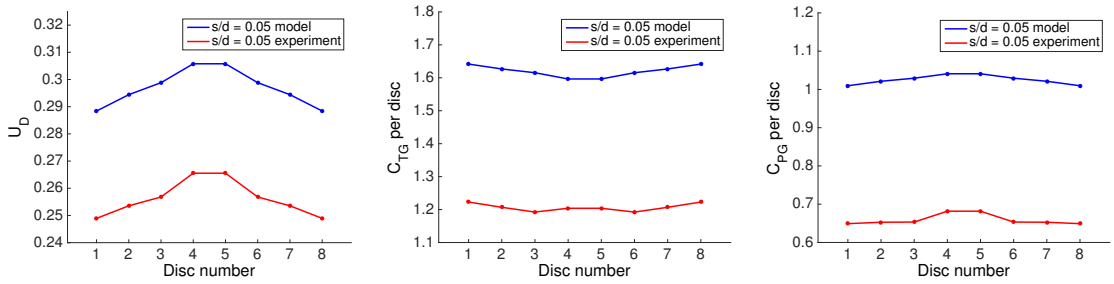

(a) U_{disc} (b) $C_{TG\text{disc}}$ (c) $C_{PG\text{disc}}$

Figure 7.7: Distributions of flow speed, thrust and power coefficients across all discs in a revised array model simulation of a $\Theta = 0.4$, $s/d = 0.4$ array, with κ distribution input taken from experimental measurements. The experimental record of each measurement for this array, averaged to remove asymmetry, is also shown for comparison.

although less pronounced than in the experimental data. It can be seen that if this edge drop-off was not occurring, and every disc behaved the same as those in the centre of the array (i.e. the assumption made in Nishino & Willden's partial fence model), the total power coefficient of the array would be higher. For the $s/d = 0.05$ array, this would correspond to an array C_{PG} of 1.05 instead of the average of 1.04: a 1% increase. Although this is significantly less variance than the 15% variation in C_{PG} seen in experimental testing, the distribution of C_{PG} is still seen to follow the same form as the variation of inferred C_{PG} measured during experiments: that is, the highest power is extracted in the centre of the array, with drop-off towards the edges.

The variation of thrust coefficient, C_{TG}, however, is not seen to vary in the same way as in experiments. Although less pronounced than the C_{PG} distribution, the experimental thrust coefficient was also seen to peak at the centre of the array, with this effect becoming clearer for more closely spaced, higher thrust arrays such as the $s/d = 0.05$ spacing shown in Figure 7.6b. (See Figure 6.5a for additional thrust curves showing similar behaviour.) The new analytical model, however, predicts a reduction in global thrust coefficient per disc towards the centre of the array, as shown in Figures 7.6b and 7.7b.

It is not entirely clear what is causing this change in the thrust distribution. However, it is likely due to additional effects occurring towards the ends of the array which are not reflected in the change of κ across the array. Given that a distribution of κ is the only input to this model which causes variation in other variables, these effects are therefore not included in the analytical model. Since the variation of κ across the array is likely to be caused by changes in wake mixing behind the discs, this does not capture any other 'end effects' due to e.g. flow diversion around the ends of the array, and cross-stream variation in approach velocity. An effect such as this could be modelled by a distribution of U_A across the array. More pronounced decrease in U_A and hence U_{disc} towards the ends of the array would lead to thrust falling off at the array ends and a more pronounced drop-off in power at the ends of the array, as was witnessed experimentally.

7.4 Further Work

As discussed, the model produces a variation in flowspeed through the array as might be expected. This flowspeed is, however, higher than that seen in experiments, albeit calculated further upstream, and does not drop off as significantly at the edges of the array as seen in experiments. This leads to an incorrect prediction of higher thrust at the edges of the array, and a prediction of power coefficient which, while dropping off at the edges of the array, shows far less of an end effect than that seen in experiments.

It is considered that an additional revision of the model to allow variation in approach flow speed across the array could improve its ability to replicate results from real arrays, as this would allow additional drop-off at the edges of the array to be included, which would provide some correction to these errors. The physical basis of this additional drop-off would come from the flow diverting around the ends of the array rather than passing through it, caused by the pressure difference across the

array. This is a physically separate effect from the alteration in κ across the array due to variation in mixing processes downstream.

7.4.1 End Effect Models for Rotor Blades

A similar end effect phenomenon exists for rotor blades, aeroplane wings and other such three-dimensional aerofoils. At the tip of a blade, the pressure difference between the loaded and unloaded sides causes flow on the loaded side to divert around the end of the blade, preventing it from contributing to lift forces (which create rotor power). The physical geometry of a row array of tidal turbines also leads to upstream high-pressure areas (as have been seen by others in computational modelling [55] [104]), so similar flow leakage around the ends of the array may contribute to lower performance by end devices.

The original tip-loss model for rotor blades was developed by Prandtl, in an appendix to the work of Betz in 1919 [96]. This was subsequently amended within a Blade Element Momentum model by Glauert in 1935 [47], allowing tip losses to be accounted for by embedding their effects within the inflow velocities applied. Further development and correction of tip loss models based on the Prandtl/Glauert model have been undertaken since, as discussed in Shen *et al.* 2005 [109]. These models result in decay of both torque and thrust towards the edges of the rotor blade. Theoretically, a similar model to account for a change in inflow velocities could be applied to the case of varying U_{disc} towards the edge of an array of turbines, if it could be equivalently developed. It could be expected to contribute to reduced thrust at the ends of the array as desired.

The basis of the blade tip loss models is the physical derivation by Prandtl [96] of a model accounting for the form of flow around the ends of a rotor blade. Although considering propellor blades at the time, instead of turbine blades, the derivation holds. It is based on the observation that flow behind a rotor can be divided into

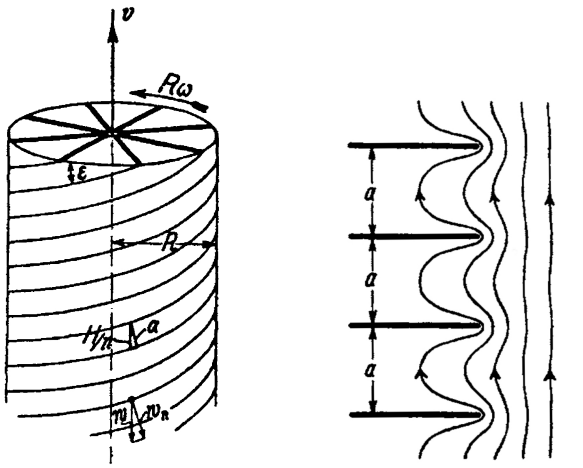

(a) Helicoids in rotor wake

(b) Equidistant planes

Figure 7.8: Physical basis of Prandtl's tip loss model, showing a) helicoidal separation in the rotor wake and b) an equivalent system of equidistant planes with flow streamlines. (Figures are as shown in Prandtl 1919 [96], as republished by Universitätsverlag Göttingen in 2010 [97]. Reproduction is licensed under a Creative Commons 3.0 BY-ND licence: https://creativecommons.org/licenses/by-nd/3.0/)

multiple helicoids traced out by the blades as the flow passes through them, as shown in Figure 7.8a. Prandtl observed that, when the helicoids were sufficiently closely packed, radial velocities at the edges of the blades were sufficiently low to be disregarded, i.e. there was minimal tip loss of flow around the blade ends. He therefore investigated the separation of these helicoids and its effect on circulation and bypass flow entrainment. Using the simple case of a series of equidistant planes to represent the helicoids, as shown in Figure 7.8b, Prandtl was able to derive a new expression for the circulation around a blade along its radial span. The expression has a dependence on the total number of blades in the rotor, and its rotational speed, as these both affect the helicoidal separation in the wake.

After a review of this physical derivation of Prandtl's tip loss model, it can be seen that any attempt to modify it or develop a similar model for the case of array end effects would not be straightforward. There is no physical equivalent in an array wake to the helicoids entrained in a rotor wake by the rotation of the blades, and

thus no downstream separation of planes to induce bypass flow entrainment. Whilst it might be considered an extreme case with infinite plane separation, this would not be solvable with the governing equations derived, and would also ignore Prandtl's observation that his correction would be less accurate for cases of fewer rotor blades.

It is considered possible that an equivalent correction factor could still be found for a row array, if greater understanding of the flow mechanics behind the edges of the array were gained: however, the wake measurements taken within the experiments are not detailed enough to formulate such an understanding. As such, the possibility of applying a 'tip-loss' style correction was not investigated further.

7.5 Conclusions

A new analytical model has been proposed which allows the inclusion of variable resistance across a row of devices arranged in a partial array form. This variable resistance was observed during the experimental work described in Chapter 6 and is thought likely to be due to variation in wake mixing downstream of the array. The new analytical model consists of a discretised array model embedded within an outer array streamtube model as previously developed in partial array theory.

The results obtained from this model when using an experimentally measured distribution of disc pressure coefficient across an 8-disc array only provide a partial match to the observed distributions of flowspeed, thrust and power. Flowspeed and power coefficient are seen to vary in the correct manner across the array, with higher values towards the centre of the array. However, they are significantly over-predicted. Thrust coefficient is seen to vary incorrectly, with higher values towards the edges of the array.

The possibility of including additional end effects which might be expected, such as flow diversion around the ends of the array analogous to tip loss effects on rotor blades,

was considered. However, it was found that there were insufficient data from the experiments carried out to develop a tip-loss style model, even though it is expected that similar effects are occurring due to pressure difference across the array.

The model presented is therefore only partially successful at including all end effects present in a short row array of tidal turbines spanning part of a tidal channel. However, it is a significant initial step which allows a measured variation of device resistance to create a variation in flow speed and extractable power across the array, and could easily form the basis of a more extensive model in future if further experimental investigation were undertaken to properly parametrise the other end effects present and implement cross-stream variation in approach flow.

Chapter 8

Conclusions

This thesis has presented several areas of work, focusing on the behaviour of tidal turbines in row arrays within channels. A new analytical model has been developed for the case of a long row array split into multiple smaller arrays. Experimental work has been carried out to interrogate assumptions and explore predictions from previous analytical modelling for the behaviour of a single row array partially spanning the width of a channel. The experimental findings were used to inform the development of a new analytical model for a single row array which can account for some of the end effects seen in short row arrays.

This chapter summarises the findings of each area of work, and makes recommendations for future work in each area. Section 8.3 summarises the original contributions made by this thesis.

8.1 Findings

8.1.1 Analytical Sub-Array Model

A new analytical model was developed for the case of a single long row array of turbines split into multiple smaller, co-linear row arrays. The model uses scale sepa-

ration between device, array and 'tidal farm' to evaluate performance at each scale. A key assumption is that wake mixing at each sub-scale completes prior to the commencement of mixing at the next scale. In addition, the sub-arrays are assumed to be quasi-infinite in length (i.e. long but still finite in relation to the width of the channel) so that end effects can be ignored.

The extractable power was found to increase by optimisation of the blockage ratios at each scale. It was found that, for any global blockage ratio considered, maximum power coefficient was always achieved when local blockage was higher than array blockage, which in turn was higher than farm blockage.

A number of blockage scenarios were considered, leading to the result that the power coefficient could be increased above the maximum achievable from a single row array. Splitting the row array into multiple smaller arrays, with higher local blockage, increased the power coefficient to a peak. However, further increases in local blockage caused over-blocked flow and the extractable power dropped away.

In the case of zero global blockage (i.e. an infinitely wide channel) a new maximum power coefficient of 0.865 is achieved at a local blockage ratio of 58%. This maximum power coefficient is 8% higher than the maximum predicted for a single row array and 46% higher than the completely unconstrained case of the Lanchester-Betz limit.

8.1.2 Experimental Investigation of Partial Array Model

A series of experiments were performed to explore the performance of porous discs in a recirculating flume, to provide data for comparison with the theoretical models. Initially a scoping exercise was completed, using five discs, to identify the likely parameter space for investigation. Based on these initial experiments new equipment was designed and built, specifically to allow multiple disc porosities and inter-disc spacings to be robustly tested. The main scope focused on providing experimental data for comparison with the analytical partial array theory developed by Nishino &

Willden [87]. The concept of 'inferred power' was introduced to allow comparison of power coefficient as well as thrust coefficient.

Variations in thrust and power coefficients on the eight-disc array showed similar trends to that predicted by the theory. Increasing thrust was recorded with both decreasing disc porosity and decreasing inter-disc spacing. A peak power coefficient was identified within the parameter space, identifying an optimal choice of disc porosity and inter-disc spacing. The thrust and power coefficients, however, were observed to be of significantly lower magnitude than those predicted by the theory.

Additionally, 'end effects' were observed on this short row array, with end discs experiencing lower thrust and power coefficients compared to those in the centre of the array. A variation in measured disc resistance was seen across the arrays, even though all discs in each array had the same open area ratio and thus nominally the same resistance. The Nishino & Willden model does not allow any variation of resistance, thrust or power across the array, so does not predict this effect.

The fluid behaviour in the array near-wake was compared to the assumptions made underpinning the theory for wake mixing and scale separation. The assumption of complete scale separation between device-scale mixing and array-scale mixing was only partially supported by the experimental measurements. Device-scale mixing was seen to complete prior to the completion of array-scale mixing, showing operation of these effects at different length scales. However, array-scale mixing was seen to initiate immediately behind the array, concurrently with device-scale mixing. This contradicts the theoretical assumption that array-scale mixing does not commence until device-scale mixing is complete.

8.1.3 Analytical Partial Array Model with Variable Device Behaviour

Following the experimental work, a new analytical model was developed capable of including a distribution of disc resistance across an array of discs. The model is based on Linear Momentum Actuator Disc Theory, and makes an assumption regarding the uniformity of bypass flow speed in all local disc channels.

Experimental measurements of the distributions of disc resistance were used as an input to the model, and the results were compared to experimental results. The flowspeed distribution across the array was found to vary similarly to that measured in the experiments, although the predicted magnitude is higher. However, the flowspeed and power coefficients predicted by the model cannot be directly compared to experimental results, which rely on measurements taken slightly downstream of the array. The power distribution was found to drop off at the ends of the array, as desired, although experimental drop-off was seen to be significantly greater, by approximately an order of magnitude. The overall magnitude of the power coefficient as predicted was significantly higher than that recorded in the experiment. The modelled thrust distribution, which is directly comparable to experimental measurements, also showed an increase in magnitude. However, the modelled thrust was seen to behave differently across the array compared to the experimental measurements. In particular, there was an increase in predicted thrust towards the ends of the array.

This work indicates that the variation in disc resistance across the array is not the only factor contributing to end effects. There is also likely to be a variation of inflow speed approaching the discs, caused by flow diverting around the ends of the array due to the pressure difference across it. However, given a lack of upstream flow measurements in the experimental work, coupled with insufficient downstream measurements to propose a new correction, this effect could not be captured within the new model.

8.2 Future Work

8.2.1 Analytical Sub-Array Model

Full computational or experimental investigation of a 'sub-array' model should be carried out to validate the model and its new assumption of scale separation between array scale and farm scale. The experimental work carried out on two four-disc arrays was inconclusive regarding the potential for increased power predicted by the theory.

8.2.2 Experimental Investigation of Partial Array Model

Carrying out a similar scope of work on a row array of rotors rather than porous discs would be a valuable exercise. This would gain additional information on wake interaction effects relevant to real tidal turbines in such an array. Varying rotor tip speed ratios, instead of varying disc porosity, would likely cause changes in wake mixing downstream of the array. The use of rotors would also allow another degree of freedom to be investigated, that of controlled cross-stream thrust variation.

8.2.3 Analytical Partial Array Model with Variable Device Behaviour

Additional experimental measurements upstream and downstream of a row array could allow development of a 'tip-loss' style correction for array flow. This would provide an additional source of end effects for the model and further reduce flowspeed, thrust and power at the ends of the array. Further amendment of the analytical model to include varying inflow velocities for each disc would allow this effect to be captured.

8.3 Contributions

Analytical Sub-Array Model

The sub-array model is the first analytical model to consider a row array split into multiple smaller, co-linear rows. This required a reformulation of the Linear Momentum Actuator Disc Theory equations to allow device scale, array scale and farm scale channel flow to be modelled. This utilises the property identified within partial array theory, but not exploited there, for multiple scales of LMADT channels to be nested within each other.

Experimental Investigation of Partial Array Model

Experimental work carried out on an eight-disc array of porous discs in a recirculating flume is presented. The thrust and flow data collected represent the first full experimental dataset that explores a partial row array with multiple spacings and multiple resistances. These data are compared to the predictions from partial array theory, allowing valuable insight into the validity of the underpinning theoretical assumptions. The data represent a significant new source of information regarding wake behaviour downstream of a row array of this form.

Analytical Partial Array Model with Variable Device Behaviour

The amended analytical partial fence model is the first to allow variation of device resistance across an array. This allows the model to predict variation in downstream flowspeed, thrust or power across an array, and is therefore the first such model to introduce end effects. The model compared favourably to trends observed in the experimental work, and also identified areas which will require further development of the model.

References

[1] T.A.A. Adcock, S. Draper, G.T. Houlsby, A.G.L. Borthwick, and S. Serhadlıoğlu. The available power from tidal stream turbines in the Pentland Firth. *Proceedings of the Royal Society A: Mathematical, Physical and Engineering Science*, 469(2157):20130072, 2013.

[2] I. Afgan, J. McNaughton, S. Rolfo, D.D. Apsley, T. Stallard, and P. Stansby. Turbulent flow and loading on a tidal stream turbine by LES and RANS. *International Journal of Heat and Fluid Flow*, 43:96–108, 2013.

[3] A.S. Bahaj, A.F. Molland, J.R. Chaplin, and W.M.J. Batten. Power and thrust measurements of marine current turbines under various hydrodynamic flow conditions in a cavitation tunnel and a towing tank. *Renewable energy*, 32(3):407–426, 2007.

[4] A.S. Bahaj, L.E. Myers, R.I. Rawlinson-Smith, and M. Thomson. The effect of boundary proximity upon the wake structure of horizontal axis marine current turbines. *Journal of Offshore Mechanics and Arctic Engineering*, 134(2):021104, 2012.

[5] A.S. Bahaj, L.E. Myers, M.D. Thomson, and N. Jorge. Characterising the wake of horizontal axis marine current turbines. In *Proceedings of the 7th European wave and tidal energy conference*, page 9, 2007.

[6] G. Bai, W. Li, H. Chang, and G. Li. The effect of tidal current directions on the optimal design and hydrodynamic performance of a three-turbine system. *Renewable Energy*, 94:48–54, 2016.

[7] L. Bai, R.R.G. Spence, and G. Dudziak. Investigation of the influence of array arrangement and spacing on tidal energy converter (TEC) performance using a 3-dimensional CFD model. In *Proceedings of the 8th European wave and tidal energy conference, Uppsala, Sweden*, pages 654–660, 2009.

[8] A. Betz. Das Maximum der theoretisch möglichen Ausnützung des Windes durch Windmotoren. *Zeitschrift für das gesamte Turbinenwesen*, 26:307–309, 1920.

[9] Black & Veatch. Phase II UK Tidal Stream Energy Resource Assessment. *Carbon Trust Marine Energy Challenge*, 2005.

[10] T. Blackmore, W.M.J. Batten, G.U. Müller, and A.S. Bahaj. Influence of turbulence on the drag of solid discs and turbine simulators in a water current. *Experiments in Fluids*, 55(1):1–10, 2014.

[11] J. Blanchfield, C. Garrett, P. Wild, and A. Rowe. The extractable power from a channel linking a bay to the open ocean. *Proceedings of the Institution of Mechanical Engineers, Part A: Journal of Power and Energy*, 222(3):289–297, 2008.

[12] R. Bucher and I. Bryden. Overcoming the marine energy pre-profit phase: What classifies the game-changing array-scale success? *International Journal of Marine Energy*, 13:180–192, 2016.

[13] T. Burton, N. Jenkins, D. Sharpe, and E. Bossanyi. *Wind energy handbook*. John Wiley & Sons, 2011.

[14] Carbon Trust. Future marine energy, 2006.

[15] Carbon Trust. UK Tidal Current Resource & Economics, 2011.

[16] C. Carlier, G. Pinon, B. Gaurier, G. Germain, and E. Rivoalen. Numerical and experimental study of elementary interactions in marine current turbines array. In *11th European Wave and Tidal Energy Conference (EWTEC)*, 2015.

[17] I.P. Castro. Wake characteristics of two-dimensional perforated plates normal to an air-stream. *Journal of Fluid Mechanics*, 46(03):599–609, 1971.

[18] L.P. Chamorro, C. Hill, S. Morton, C. Ellis, R.E.A. Arndt, and F. Sotiropoulos. On the interaction between a turbulent open channel flow and an axial-flow turbine. *Journal of Fluid Mechanics*, 716:658–670, 2013.

[19] Y. Chen, B. Lin, J. Lin, and S. Wang. Effects of stream turbine array configuration on tidal current energy extraction near an island. *Computers & Geosciences*, 77:20–28, 2015.

[20] M.J. Churchfield, Y. Li, and P.J. Moriarty. A large-eddy simulation study of wake propagation and power production in an array of tidal-current turbines. *Philosophical Transactions of the Royal Society of London A: Mathematical, Physical and Engineering Sciences*, 371(1985):20120421, 2013.

[21] European Commission. Communication from the commission to the European parliament, the council, the European economic and social committee and the committee of the regions: Energy Roadmap 2050, 2011.

[22] S.C. Cooke, R. H. J. Willden, B.W. Byrne, T. Stallard, and T. Feng. An experimental investigation of blockage in a short fence array of tidal turbines. *Proceedings of the 1st RENEW conference, Lisbon, Portugal*, 2014.

[23] D.M. Culley, S.W. Funke, S.C. Kramer, and M.D. Piggott. Tidal stream resource assessment through optimisation of array design with quantification of uncertainty. In *11th European Wave and Tidal Energy Conference (EWTEC)*, 2015.

[24] T. Daly, L.E. Myers, and A.S. Bahaj. Experimental analysis of the local flow effects around single row tidal turbine arrays. In *Third International Conference and Exhibition on Ocean Energy, Bilbao, Spain, 06 - 08 Oct 2010*, 2010.

[25] T. Daly, L.E. Myers, and A.S. Bahaj. Modelling of the flow field surrounding tidal turbine arrays for varying positions in a channel. *Philosophical Transactions of the Royal Society A: Mathematical, Physical and Engineering Sciences*, 371(1985):20120246, 2013.

[26] T.A. de Jesus Henriques, T.S. Hedges, I. Owen, and R.J. Poole. The effect of wave-current interaction on the near-wake of horizontal axis tidal stream turbines. In *11th European Wave and Tidal Energy Conference, EWTEC*, 2015.

[27] T.A. de Jesus Henriques, T.S. Hedges, I. Owen, and R.J. Poole. The influence of blade pitch angle on the performance of a model horizontal axis tidal stream turbine operating under wave–current interaction. *Energy*, 102:166–175, 2016.

[28] DECC. Renewable energy roadmap. *Crown Copyright, Department of Energy & Climate Change, London*, 2011.

[29] DECC. 2010 to 2015 government policy: low carbon technologies, 2015.

[30] DECC. Third progress report of the promotion and use of energy from renewable sources for the united kingdom, 2016.

[31] Energy Department for Business and Industrial Strategy. Digest of United Kingdom Energy Statistics, 2016.

[32] T. Divett, R. Vennell, and C. Stevens. Channel-scale optimisation and tuning of large tidal turbine arrays using LES with adaptive mesh. *Renewable Energy*, 86:1394–1405, 2016.

[33] S. Draper, A.G.L. Borthwick, and G.T. Houlsby. Energy potential of a tidal fence deployed near a coastal headland. *Philosophical Transactions of the Royal Society A: Mathematical, Physical and Engineering Sciences*, 371(1985):20120176, 2013.

[34] S. Draper, G.T. Houlsby, M.L.G. Oldfield, and A.G.L. Borthwick. Modelling tidal energy extraction in a depth-averaged coastal domain. *IET Renewable Power Generation*, 4(6):545–554, 2010.

[35] S. Draper and T. Nishino. Centred and staggered arrangements of tidal turbines. *Journal of Fluid Mechanics*, 739:72–93, 2014.

[36] S. Draper, T. Stallard, P.K. Stansby, S. Way, and T.A.A. Adcock. Laboratory scale experiments and preliminary modelling to investigate basin scale tidal stream energy extraction. In *Proceedings of the 10th European Wave and Tidal Energy Conference*, 2013.

[37] The Crown Estate. UK Wave and Tidal Key Resource Areas Project October 2012 - Summary Report, 2012.

[38] The Crown Estate. UK Wave and Tidal Key Resource Areas Project - Technical Methodology Report, 2013.

[39] European Commission and Others. Non-nuclear energy Joule II Wave Energy Project Results. *The exploitation of tidal marine currents. European Commission DG Sci [Rep. EUR 16683 EN]*, 1996.

[40] C.F. Fleming. *Tidal turbine performance in the offshore environment.* PhD thesis, The University of Oxford, 2014.

[41] C.F. Fleming, S.C. McIntosh, and R.H.J. Willden. Tidal turbine performance in sheared flow. In *Proceedings of 10th European Wave and Tidal Energy Conference (EWTEC), Aalborg, Denmark*, 2013.

[42] P. L. Fraenkel. Power from marine currents. *Proceedings of the Institution of Mechanical Engineers, Part A: Journal of Power and Energy*, 216(1):1–14, 2002.

[43] S.W. Funke, P.E. Farrell, and M.D. Piggott. Tidal turbine array optimisation using the adjoint approach. *Renewable Energy*, 63:658–673, 2014.

[44] S. Gant and T. Stallard. Modelling a tidal turbine in unsteady flow. In *The Eighteenth International Offshore and Polar Engineering Conference*. International Society of Offshore and Polar Engineers, 2008.

[45] C. Garrett and P. Cummins. The power potential of tidal currents in channels. *Proceedings of the Royal Society A: Mathematical, Physical and Engineering Science*, 461(2060):2563–2572, 2005.

[46] C. Garrett and P. Cummins. The efficiency of a turbine in a tidal channel. *Journal of Fluid Mechanics*, 588:243–251, 2007.

[47] Hermann Glauert. Airplane propellers. In *Aerodynamic theory*, pages 169–360. Springer, 1935.

[48] Andritz Hydro GmbH. Promising Results. *Hydro News*, 25:23, 2014.

[49] J.M.R. Graham. Turbulent flow past a porous plate. *Journal of Fluid Mechanics*, 73(03):565–591, 1976.

[50] National Grid. Future energy sources 2016, 2016.

[51] A. Harang, R. Vennell, and M. Smeaton. How large scale channel dynamics influence the optimum tidal power available? In *11th European Wave and Tidal Energy Conference (EWTEC)*, 2015.

[52] M.E. Harrison, W.M.J. Batten, L.E. Myers, and A.S. Bahaj. Comparison between CFD simulations and experiments for predicting the far wake of horizontal axis tidal turbines. *IET Renewable Power Generation*, 4(6):613–627, 2010.

[53] T. Hooper and M. Austen. Tidal barrages in the UK: Ecological and social impacts, potential mitigation, and tools to support barrage planning. *Renewable and Sustainable Energy Reviews*, 23:289–298, 2013.

[54] W. Hunter. *Actuator disk methods for tidal turbine arrays*. PhD thesis, The University of Oxford, 2015.

[55] W. Hunter, T. Nishino, and R.H.J. Willden. Investigation of tidal turbine array tuning using 3D Reynolds-Averaged Navier–Stokes Simulations. *International Journal of Marine Energy*, 10:39–51, 2015.

[56] IEA. Key Renewables Trends - Excerpt from : Renewables information (2016 Edition), 2016.

[57] British Standards Institution. PD IEC/TS 62600-201:2015 Marine energy Wave, tidal and other water current converters Part 201: Tidal energy resource assessment and characterization, 2015.

[58] C.T. Jacobs, M.D. Piggott, S.C. Kramer, and S.W. Funke. On the validity of tidal turbine array configurations obtained from steady-state adjoint optimisation. 2016.

[59] P. Jeffcoate, F. Salvatore, C. Boake, and B. Elsaesser. Effect of submergence on tidal turbine performance. In *11th European Wave and Tidal Energy Conference, EWTEC*, 2015.

[60] P. Jeffcoate, R. Starzmann, B. Elsaesser, S. Scholl, and S. Bischoff. Field measurements of a full scale tidal turbine. *International Journal of Marine Energy*, 12:3 – 20, 2015. Special Issue on Marine Renewables Infrastructure Network.

[61] P. Jeffcoate, T. Whittaker, C. Boake, and B. Elsaesser. Field tests of multiple 1/10 scale tidal turbines in steady flows. *Renewable Energy*, 87:240–252, 2016.

[62] C.H. Jo, J.Y. Yim, K.H. Lee, and K.O. Ko. Performance of multi-arrayed tidal current power rotors. In *3rd International Conference on Ocean Energy (ICOE). Bilbao, Spain*, 2010.

[63] L-B. Jordan, S. Simmons, S. McLelland, B. Murphy, D. Parsons, and L. Vybulkova. The impact of tidal stream turbines on 3D flow and bed shear stress measured with particle image velocimetry in a laboratory flume. In *11th European Wave and Tidal Energy Conference, EWTEC*, 2015.

[64] N.E. Joukowsky. Windmill of the NEJ type. *Transactions of the Central Institute for Aero-hydrodynamics of Moscow*, 1:57, 1920.

[65] R. Karsten, A. Swan, and J. Culina. Assessment of arrays of in-stream tidal turbines in the Bay of Fundy. *Phil. Trans. R. Soc. A*, 371(1985):20120189, 2013.

[66] Y. Kervella, G. Germain, B. Gaurier, J.-V. Facq, and T. Bacchetti. Mise en évidence de limportance de la turbulence ambiante sur les effets dinteraction entre hydroliennes. In *XIIIèmes Journées Nationales Génie Côtier–Génie Civil, 2-4 July 2014, Dunkerque*, 2014.

[67] S.C. Kramer, S.W. Funke, and M.D. Piggott. A continuous approach for the optimisation of tidal turbine farms. In *11th European Wave and Tidal Energy Conference (EWTEC)*, 2015.

[68] F. W. Lanchester. A contribution to the theory of propulsion and the screw propeller. *Journal of the American Society for Naval Engineers*, 27(2):509–510, 1915.

[69] ABP Marine Environmental Research Ltd. Atlas of UK Marine Renewable Energy Resources. Technical Report R.1106, Department of Trade and Industry, 2004.

[70] Anatec Ltd. Navigation Risk Assessment Update - Fall of Warness. Technical Report A2343-EMEC-NRA-1, European Marine Energy Centre (EMEC), 2010.

[71] A.J. MacLeod, S. Barnes, K.G. Rados, and I.G. Bryden. Wake effects in tidal current turbine farms. In *International conference on marine renewable energy*, pages 49–53, 2002.

[72] R. Malki, I. Masters, A.J. Williams, and T.N. Croft. The influence of tidal stream turbine spacing on performance. In *Proceedings of the 9th European Wave and Tidal Energy Conference (EWTEC). Southampton, UK*, pages 10–14, 2011.

[73] R. Malki, I. Masters, A.J. Williams, and T.N. Croft. Planning tidal stream turbine array layouts using a coupled blade element momentum–computational fluid dynamics model. *Renewable Energy*, 63:46–54, 2014.

[74] R. Malki, A.J. Williams, T.N. Croft, M. Togneri, and I. Masters. A coupled blade element momentum–computational fluid dynamics model for evaluating tidal stream turbine performance. *Applied Mathematical Modelling*, 37(5):3006–3020, 2013.

[75] B.S. Massey and J. Ward-Smith. *Mechanics of fluids (9th Edition)*, volume 1. CRC Press, 2011.

[76] I. Masters, J.C. Chapman, M.R. Willis, and J.A.C. Orme. A robust blade element momentum theory model for tidal stream turbines including tip and hub loss corrections. *Journal of Marine Engineering & Technology*, 10(1):25–35, 2011.

[77] J. McNaughton. *Turbulence modelling in the near-field of an axial flow tidal turbine using Code Saturne*. PhD thesis, The University of Manchester, 2013.

[78] J. McNaughton, S. Harper, R. Sinclair, and B. Sellar. Measuring and modelling the power curve of a commercial-scale tidal turbine. In *11th European Wave and Tidal Energy Conference, EWTEC*, 2015.

[79] J. McNaughton, S. Rolfo, D.D. Apsley, T. Stallard, and P.K. Stansby. CFD power and load prediction on a 1 MW tidal stream turbine with typical velocity profiles from the EMEC test site. In *Proceedings of the 10th European Wave and Tidal Energy Conference*, 2013.

[80] Ian A Milne, Alexander Day, Rajnish N Sharma, Richard GJ Flay, and Simon Bickerton. Tidal turbine blade load experiments for oscillatory motion. In *9th European Wave and Tidal Energy Conference, EWTEC 2011*, 2011.

[81] P. Mycek, B. Gaurier, G. Germain, G. Pinon, and E. Rivoalen. Experimental study of the turbulence intensity effects on marine current turbines behaviour. Part I: One single turbine. *Renewable Energy*, 66:729–746, 2014.

[82] P. Mycek, B. Gaurier, G. Germain, G. Pinon, and E. Rivoalen. Experimental study of the turbulence intensity effects on marine current turbines behaviour. Part II: Two interacting turbines. *Renewable Energy*, 68:876–892, 2014.

[83] L. Myers and A.S. Bahaj. Wake studies of a 1/30th scale horizontal axis marine current turbine. *Ocean Engineering*, 34(5):758–762, 2007.

[84] L.E. Myers and A.S. Bahaj. Experimental analysis of the flow field around horizontal axis tidal turbines by use of scale mesh disk rotor simulators. *Ocean Engineering*, 37(2):218–227, 2010.

[85] L.E. Myers and A.S. Bahaj. An experimental investigation simulating flow effects in first generation marine current energy converter arrays. *Renewable Energy*, 37(1):28–36, 2012.

[86] L.E. Myers, B. Keogh, and A.S. Bahaj. Layout optimisation of 1st-generation tidal energy arrays. In *Proc. of 9th European Wave and Tidal Energy Conference*, 2011.

[87] T. Nishino and R. H. J. Willden. The efficiency of an array of tidal turbines partially blocking a wide channel. *Journal of Fluid Mechanics*, 708:596–606, 2012.

[88] T. Nishino and R. H. J. Willden. Two-scale dynamics of flow past a partial cross-stream array of tidal turbines. *Journal of Fluid Mechanics*, 730:220–244, 2013.

[89] Nortek AS, http://www.nortek-as.com/en/support/manuals. *Comprehensive Manual*, December 2013.

[90] T. O'Doherty, D.A. Egarr, A. Mason-Jones, and D.M. O'Doherty. An assessment of axial loading on a five-turbine array. *Proceedings of the ICE-Energy*, 162(2):57–65, 2009.

[91] A. Olczak, T. Stallard, T. Feng, and P.K. Stansby. Comparison of a RANS blade element model for tidal turbine arrays with laboratory scale measurements of wake velocity and rotor thrust. *Journal of Fluids and Structures*, 64:87–106, 2016.

[92] A. Olczak, T. Stallard, and P. K. Stansby. The influence of waves on tidal stream turbine wake recovery. *Proceedings of the 10th European Wave and Tidal Energy Conference*, 2013.

[93] OpenHydro. OpenHydro deploys second Paimpol-Bréhat turbine. Press Release, May 2016. `http://www.openhydro.com/news/OpenHydroPR-2016-05-30.pdf`.

[94] F. O'Rourke, F. Boyle, and A. Reynolds. Tidal energy update 2009. *Applied Energy*, 87(2):398–409, 2010.

[95] European Parliament. DIRECTIVE 2009/28/EC OF THE EUROPEAN PARLIAMENT AND OF THE COUNCIL of 23 April 2009 on the promotion of the use of energy from renewable sources and amending and subsequently repealing Directives 2001/77/EC and 2003/30/EC, 2009.

[96] L Prandtl and A Betz. Schraubenpropeller mit geringstem Energieverlust. *Göttinger Nachrichten*, 2, 1919.

[97] L. Prandtl and A. Betz. *Vier Abhandlungen zur Hydrodynamik und Aerodynamik*, volume 3. Universitätsverlag Göttingen, 2010.

[98] reNEWS. First Power for Atlantis at MeyGen, 2016. `http://renews.biz/104916/first-power-for-atlantis-at-meygen/`.

[99] reNEWS. ScotRenewables launches 2MW kit. Press Release, May 2016. `http://renews.biz/102659/scotrenewables-launches-2mw-kit/`.

[100] A. Roberts, B. Thomas, P. Sewell, Z. Khan, S. Balmain, and J. Gillman. Current tidal power technologies and their suitability for applications in coastal and marine areas. *Journal of Ocean Engineering and Marine Energy*, 2(2):227–245, 2016.

[101] M. Sánchez, R. Carballo, V. Ramos, and G. Iglesias. Floating vs. bottom-fixed turbines for tidal stream energy: A comparative impact assessment. *Energy*, 72:691–701, 2014.

[102] M. Sánchez, R. Carballo, V. Ramos, and G. Iglesias. Tidal stream energy impact on the transient and residual flow in an estuary: a 3D analysis. *Applied Energy*, 116:167–177, 2014.

[103] B. Sanderse, S.P. Pijl, and B. Koren. Review of computational fluid dynamics for wind turbine wake aerodynamics. *Wind Energy*, 14(7):799–819, 2011.

[104] J. Schluntz. *Tidal Turbine Array Modelling*. PhD thesis, The University of Oxford, 2014.

[105] J. Schluntz and R.H.J. Willden. The effect of blockage on tidal turbine rotor design and performance. *Renewable Energy*, 81:432–441, 2015.

[106] C.L. Sequeira and R.J. Miller. Loss mechanisms in tidal stream turbines. In *Proceedings of the 10th European Wave and Tidal Energy Conference (EWTEC), Aalborg, Denmark*, 2013.

[107] S. Serhadlıoğlu, T.A.A. Adcock, G.T. Houlsby, S. Draper, and A.G.L. Borthwick. Tidal stream energy resource assessment of the Anglesey Skerries. *International Journal of Marine Energy*, 3:e98–e111, 2013.

[108] P.M. Sforza, P. Sheerin, and M. Smorto. Three-dimensional wakes of simulated wind turbines. *AIAA Journal*, 19(9):1101–1107, 1981.

[109] W.Z. Shen, R. Mikkelsen, J.N. Sørensen, and C. Bak. Tip loss corrections for wind turbine computations. *Wind Energy*, 8:457–475, 2005.

[110] M. Smeaton, R. Vennell, and A. Harang. How does channel constriction affect the potential for tidal stream power? In *11th European Wave and Tidal Energy Conference (EWTEC)*, 2015.

[111] M. Smeaton, R. Vennell, and A. Harang. The effect of channel constriction on the potential for tidal stream power. *Renewable Energy*, 99:45–56, 2016.

[112] J.N. Sørensen and W.Z. Shen. Numerical modeling of wind turbine wakes. *Journal of fluids engineering*, 124(2):393–399, 2002.

[113] T. Stallard, R. Collings, T. Feng, and J. Whelan. Interactions between tidal turbine wakes: experimental study of a group of three-bladed rotors. *Philosophical Transactions of the Royal Society A: Mathematical, Physical and Engineering Sciences*, 371(1985):20120159, 2013.

[114] T. Stallard, T. Feng, and P.K. Stansby. Experimental study of the mean wake of a tidal stream rotor in a shallow turbulent flow. *Journal of Fluids and Structures*, 54:235–246, 2015.

[115] T. Stallard, T. Feng, and P.K. Stansby. Experimental study of the mean wake of a tidal stream rotor in a shallow turbulent flow. *Journal of Fluids and Structures*, 54:235 – 246, 2015.

[116] P.K. Stansby and T. Stallard. Fast optimisation of tidal stream turbine positions for power generation in small arrays with low blockage based on superposition of self-similar far-wake velocity deficit profiles. *Renewable Energy*, 92:366–375, 2016.

[117] X. Sun. *Numerical and experimental investigation of tidal current energy extraction*. PhD thesis, The University of Edinburgh, 2008.

[118] X. Sun, J. Chick, and I. Bryden. Laboratory-scale simulation of energy extraction from tidal currents. *Renewable Energy*, 33(6):1267–1274, 6 2008.

[119] G. I. Taylor. Air resistance of a flat plate of very porous material. *ARC Reports and Memoranda*, 2236, 1944.

[120] S.C. Tedds. *Scale Model Testing of Tidal Stream Turbines: Wake Characterisation in Realistic Flow Conditions*. PhD thesis, The University of Liverpool, 2014.

[121] S.C. Tedds, R.J. Poole, and I. Owen. Wake characteristics of horizontal axis tidal stream turbines in uniform and non-uniform steady flows. In *4th International Conference on Ocean Energy (ICOE), Dublin, Ireland*, 2012.

[122] N. Troldborg, J.N. Sorensen, and R. Mikkelsen. Numerical simulations of wake characteristics of a wind turbine in uniform inflow. *Wind Energy*, 13(1):86–99, 2010.

[123] S.R. Turnock, A.B. Phillips, J. Banks, and R. Nicholls-Lee. Modelling tidal current turbine wakes using a coupled RANS-BEMT approach as a tool for analysing power capture of arrays of turbines. *Ocean Engineering*, 38(11):1300–1307, 2011.

[124] Andreas Uihlein and Davide Magagna. Wave and tidal current energy–A review of the current state of research beyond technology. *Renewable and Sustainable Energy Reviews*, 58:1070–1081, 2016.

[125] G.A.M. Van Kuik. The Lanchester–Betz–Joukowsky limit. *Wind Energy*, 10(3):289–291, 2007.

[126] R. Vennell. Tuning turbines in a tidal channel. *Journal of Fluid Mechanics*, 663:253–267, 2010.

[127] R. Vennell. Tuning tidal turbines in-concert to maximise farm efficiency. *Journal of Fluid Mechanics*, 671(1):587–604, 2011.

[128] R. Vennell. The energetics of large tidal turbine arrays. *Renewable Energy*, 48:210–219, 2012.

[129] R. Vennell, S.W. Funke, S. Draper, C. Stevens, and T. Divett. Designing large arrays of tidal turbines: A synthesis and review. *Renewable and Sustainable Energy Reviews*, 41:454–472, 2015.

[130] C.R. Vogel. *Theoretical Limits to Tidal Stream Energy Extraction*. PhD thesis, The University of Oxford, 2014.

[131] C.R. Vogel, G.T. Houlsby, and R.H.J. Willden. Effect of free surface deformation on the extractable power of a finite width turbine array. *Renewable Energy*, 88:317–324, 2016.

[132] C.R. Vogel, R.H.J. Willden, and G.T. Houlsby. A correction for depth-averaged simulations of tidal turbine arrays. In *Proceedings of the 10th European Wave and Tidal Energy Conference (EWTEC), Aalborg, Denmark*, volume 25, 2013.

[133] S. Waters and G. Aggidis. A world first: Swansea Bay Tidal lagoon in review. *Renewable and Sustainable Energy Reviews*, 56:916–921, 2016.

[134] J. I. Whelan, J. M. R. Graham, and J. Peiro. A free-surface and blockage correction for tidal turbines. *Journal of Fluid Mechanics*, 624(1):281–291, 2009.

[135] J.I. Whelan. *A fluid dynamic study of free-surface proximity and inertia effects on tidal turbines*. PhD thesis, Imperial College London, 2010.

[136] J.I. Whelan and T. Stallard. Arguments for modifying the geometry of a scale model rotor. In *Proceedings of 9th European Wave and Tidal Energy Conference*, 2011.

[137] H. Xiao, L. Duan, R. Sui, and T. Rosgen. Experimental investigations of turbulent wake behind porous disks. *Proceedings of the 1st Marine Energy Technology Symposium*, 2013.